High Coupling Materials for Thin Film Bulk Acoustic Wave Resonators

THÈSE N^{O} 4489 (2009)

PRÉSENTÉE LE 18 SEPTEMBRE 2009
À LA FACULTÉ SCIENCES ET TECHNIQUES DE L'INGÉNIEUR
LABORATOIRE DE CÉRAMIQUE
PROGRAMME DOCTORAL EN SCIENCE ET GÉNIE DES MATÉRIAUX

ÉCOLE POLYTECHNIQUE FÉDÉRALE DE LAUSANNE

POUR L'OBTENTION DU GRADE DE DOCTEUR ÈS SCIENCES

PAR

Janine CONDE

acceptée sur proposition du jury:

Prof. H. Hofmann, président du jury
Prof. P. Muralt, directeur de thèse
Prof. I. Katardjiev, rapporteur
Dr T. Metzger, rapporteur
Prof. P. Ryser, rapporteur

ÉCOLE POLYTECHNIQUE
FÉDÉRALE DE LAUSANNE

Suisse
2009

Abstract

Radio frequency (RF) filters based on bulk acoustic wave resonances in piezoelectric thin films have become indispensable components in mobile communications. The currently used material, AlN, exhibits many excellent properties for this purpose. However, its bandwidth is often a limiting factor. In addition, no tuning is possible with AlN. Ferroelectrics would offer both larger coupling to achieve larger bandwidths, and tunability. However, their acoustic properties are not well known, especially in the thin film case. The goal of this thesis is to investigate the potential and identify the limitations of ferroelectric thin films for thickness mode resonators in the 0.5 - 2 GHz range.

The $\mathrm{Pb(Zr}_x\mathrm{,Ti}_{1-x}\mathrm{)O}_3$ (PZT) solid solution system is the main candidate, since it is known for its large piezoelectric constants and its growth is already well studied. As a main test vehicle, free standing thin film bulk acoustic resonator (TFBAR) structures with Pt/PZT/Pt/SiO_2 membranes were successfully fabricated using silicon micro-machining techniques. The main drawback of ferroelectrics is the damping of acoustic waves by domain wall motion both in the RF electric field and in the pressure wave. For this reason films with varying orientations and compositions were investigated. From the device structures the electro-mechanical coupling constants k_t^2, the quality factors (Q-factors) and several materials parameters have been obtained. High coupling constants have been found for sol-gel $\mathrm{Pb(Zr}_{0.53}\mathrm{,Ti}_{0.47}\mathrm{)O}_3$ films with a {100} texture, k_t^2 is found to be 0.4 for a 1 μm thick film and 0.8 for a 3.8 μm thick film. However, the Q-factors of these films are low, 18 for the first film and 3 for the second film. The increase of k_t^2 and the decrease of the Q-factor with frequency indicates that the domains present in these films contribute to these characteristic parameters. It was generally observed that high coupling constant are associated to low Q-factors. This became evident when comparing films with 53/47 composition, where both tetragonal and rhombohedral phases are present, to tetragonal films as well as when comparing {100} textures with (111) textures. Both for the 53/47 composition and for the {100} texture, ferroelastic domain walls are thought to play a bigger role than for tetragonal compositions and (111) textures. The highest figure of merit (FOM) of about 15 was found when combining the composition leading to a high coupling constant (53/47) and the orientation leading to lower losses (111). However the losses even in this film are too high for RF-filter applications. On the other hand, films with low Q-factors but high coupling could prove very useful as transducers for ultrasonic imaging applications, where low Q-factors are desired.

The stiffness coefficients of the studied PZT films were shown to be higher than expected from ceramics data. Most likely the stiffness of ceramics always contains domain contributions leading to softening. In contrast, in textured films the variety of domain orientation is very much reduced.

In order to reduce losses due the presence of ferroelastic domains three different potential solutions were explored. The first idea was to manipulate the domain populations of the films deposited on silicon by using heat and vacuum treatments. Silicon substrates are known from previous works to be unfavourable for high c-domain fractions. It was discovered that an anneal in vacuum at 550°C lead to a significant reduction of c-domains in tetragonal 30/70 PZT ($\{100\}$). On the contrary, if the sample was subjected to a compressive stress during cooling, the c-domain fraction could be increased. Analysis of the film stress versus temperature curves revealed a trend consistent with theoretical predictions, i.e. a phase boundary between the $c/a/c/a$ and the $a_1/a_2/a_1/a_2$ domain patterns between room temperature and the Curie temperature θ_C. However, even though this method reveals interesting results, it can not be exploited as a method to achieve a sufficient c-domain population.

The second idea explored was the implementation of a high thermal expansion material as a substrate. PZT films deposited on MgO are known to be compressive due to the difference in thermal expansion of the two materials. The compressive stress leads to highly c-axis oriented PZT films. Devices using MgO substrates were fabricated, however difficulties in the micromachining of the MgO substrate inhibited a complete liberation of the membrane. Nevertheless, preliminary measurements indicate these devices could lead to both high coupling and high Q-factors, suggesting that further detailed study of this method is worthwhile.

As a third method for avoiding ferroelastic domains, the uniaxial ferroelectric potassium lithium niobate (KLN) was explored. The unique ferroelectric axis in this material means that only 180° domain walls are present, which can theoretically be removed by poling. This material has been deposited in thin film form using pulsed laser deposition (PLD). KLN thin films with a $\{001\}$ texture were deposited successfully on Pt/Si substrates. The films were piezoelectric with a $d_{33,f}$ value of around 10 pm/V and a dielectric constant of 250. This is the first time that piezoelectric properties were measured on KLN thin films. A columnar structure has been observed, however the small grain size and the rough surface currently make it difficult to apply this material to TFBAR's.

Keywords: ferroelectric, thin film bulk acoustic wave resonator,TFBAR, PZT, RF-MEMS

Zusammenfassung

Radiofrequenz-Bandpassfilter basierend auf akustischen Raumwellen-Dünnschichtresonatoren (TFBAR) sind zu unentbehrlichen Komponenten für mobile Telekommunikation geworden. Das gegenwärtig eingesetzte Material AlN besitzt zwar viele hervorragende Eigenschaften für diese Anwendung; es ist jedoch bezüglich seiner Bandbreite limitiert. Ausserdem ist Tuning bei AlN nicht möglich. Ferroelektrika würden sowohl hohe Kopplungskonstanten, die zu breiten Bandbreiten führen, bieten, als auch ein Tuning ermöglichen. Allerdings sind die akustischen Eigenschaften von ferroelektrischen Materialien, vor allem im Fall von dünnen Schichten, noch weitgehend unbekannt. Das Ziel dieser Dissertation ist, das Potential und die Grenzen von ferroelektrischen Dünnschichten in Resonatoren basierend auf Dickenschwingungen im Frequenzbereich von 0.5 - 2 GHz zu untersuchen.

Das $Pb(Zr_x,Ti_{1-x})O_3$ (PZT) Mischkristallsystem ist ein vielversprechender Kandidat, da es für seine hohen piezoelektrischen Konstanten bekannt ist und die Herstellung von PZT Schichten gut beherrscht wird. Freistehende $Pt/PZT/Pt/SiO_2$ Membrane wurden mittels Silizium Mikrofabrikationstechniken hergestellt und als Testruktur benutzt. Der grösste Nachteil von Ferroelektrika ist die Dämpfung der akustischen Wellen durch Bewegungen der Domänenwände im elektrischen Feld und in der Druckwelle. Aus diesem Grund wurden Schichten mit unterschiedlichen Orientierungen und Zusammensetzungen studiert. Impedanzmessungen der Resonatoren ermöglichen die Bestimmung der Kopplungsfaktoren (k_t^2), Qualitätsfaktoren (Q-Faktor) und mehrerer Materialskonstanten. Grosse Kopplungsfaktoren wurden für $Pb(Zr_{0.53},Ti_{0.47})O_3$ Sol-Gel Schichten mit einer {100} Textur erzielt, ein Kopplungfaktor von 0.4 ist für eine 1 μm dicke Schicht ermittelt worden und 0.8 für eine 3.8 μm dicke Schicht. Allerdings sind die Q-Faktoren dieser Schichten klein, 18 für die erste Schicht und 3 für die zweite. Der Anstieg von k_t^2 und die Abnahme des Q-Faktors mit steigender Frequenz deuten an, dass die Domänen, die in diesen Schichten vorhanden sind, zu diesen Werten beitragen. Hohe Kopplungskonstanten konnten in allen hergestellten Schichten mit kleinen Q-Faktoren assoziiert werden. Dies wurde beim Vergleichen von 53/47 Schichten (bestehend aus rhombohedrischer und tetragonaler Phase) mit tetragonalen Schichten, als auch beim Vergleichen von {100} Texturen mit (111) Texturen beobachtet. Sowohl bei Schichten mit 53/47 Zusammensetzung als auch bei {100} texturierten Schichten spielen ferroelastische Domänenwände eine grössere Rolle als bei tetragonalen Zusammensetzungen und bei (111) texturierten Schichten. Der grösste Gütefaktor von ungefähr 15 wurde beim Kombinieren von einer Zusammensetzung, die zu hoher Kopplung führt (53/47), mit einer Textur, die zu tiefen Verlusten führt (111), erreicht. Trotzdem sind die Dämpfungsverluste zu hoch für eine Anwendung in RF-Filtern. Kleine Q-Faktoren kombiniert mit hohen Kopplungskonstanten sind aber für eine andere Anwendung interessant, nämlich im Bereich der medizinischen Ultraschallabbildung, wo kleine Q-Faktoren erwünscht sind und immer höhere Frequenzen interessant werden.

Um die Dämpfungsverluste verursacht durch ferroelastische Domänen zu mindern, wurden drei potenzielle Lösungen untersucht. Die erste Idee war, die Domänenpopulation von auf Silizium aufgebrachten Schichten mit Hilfe von Wärmebehandlungen in Vakuum zu beeinflussen. Es ist bekannt, dass Silizium als Substrat unvorteilhaft ist um einen hohen Anteil an *c*-Domänen zu erreichen. Es wurde beobachtet, dass eine Wärmebehandlung im Vakuum bei 550°C bei tetragonalen (30/70) ({100}) zu einer Abnahme des *c*-Domänen Anteils führte. Wurde hingegen während der Wärmebehandlung zusätlich ein kompressiver Druck auf die Schicht ausgeübt, konnte der *c*-Domänen Anteil leicht erhöht werden. Bei der Analyse der Spannungs-Temperatur Kurven wurde ein theoretisch vorausgesagtes Verhalten beobachtet, nämlich der Phasenübergang von $c/a/c/a$ zu $a_1/a_2/a_1/a_2$ Domänenkonfigurationen. Dieser Phasenübergang wurde zum ersten Mal experimentell beobachtet. Obwohl Veränderungungen der Domänenkonfigurationen mit Wärmebehandlungen im Vakuum beobachtet werden können, ist dies keine geeignete Methode, einen genügend grossen *c*-Domänen Anteil zu erhalten.

Der zweite Ansatz, der erforscht wurde, ist die Anwendung von einem Substrat mit einem hohen thermischen Ausdehnungskoeffizient. Auf MgO gewachsene PZT Schichten sind kompressiv, da der thermische Ausdehnungskoeffizient von MgO grösser ist als der von PZT. Die Druckspannung führt zu Schichten mit der *c*-Achse senkrecht zur Substratebene. PZT Schichten mit (001) Orientierung wurden auf MgO Substraten erfolgreich aufgebracht, die Herstellung von Membranen auf diesem Substrat war jedoch schwierig. Die Methode ist vielverprechend, eine geeignete Ätztechnik für Resonatoren auf MgO Substraten muss jedoch noch erarbeitet werden.

Als dritte Methode, um ferroelastische Domänen zu vermeiden, wurde das uniaxiale Ferroelektrikum Kaliumlithiumniobat (KLN) in Betracht gezogen. Da nur eine ferroelektrische Achse in diesem Material existiert, können theorethisch alle Domänen durch Polen entfernt werden. KLN wurde mit Laserstrahlverdampfen (pulsed laser deposition (PLD)) auf Pt/Si Substraten aufgebracht. Die Filme sind piezoelektrisch mit einem piezoelektrischen Koeffizienten $d_{33,f}$ von ungefähr 10 pm/V und einer Dielektrizitätskonstante von 250. Piezoelektrische Eigenschaften von KLN Dünnschichten wurden zum ersten Mal gemessen. Die rauhe Oberfläche und die schwer kontrollierbare Zusammensetzung zeigen aber, dass die Studien dieser Schichten noch im Anfangsstadium sind, aber eine Anwendung in TFBAR's nicht auszuschliessen ist.

Stichwörter: Ferroelektrika, akustischer Raumwellen-Dünnschichtresonator, TFBAR, PZT, RF-MEMS

Contents

Chapter 1

Introduction

This Chapter starts with an introduction to bulk acoustic wave (BAW) resonators beginning by introducing acoustic waves in solids, explaining the operation principle of BAW resonators and illustrating a few applications. The principal materials in use or considered to be used for BAW applications are discussed next. The following section gives an overview of the state of the art of PZT in BAW resonators, PZT being the main material considered for high coupling BAW applications. Alternative materials and methods shall be introduced in Chapter 4. Since the main problem of PZT for BAW applications are the acoustic losses in the material, Section 1.4 is devoted to this subject. Finally the aims of this thesis will be described followed by an outline of the thesis.

1.1 BAW resonators: Introduction and Applications

1.1.1 Acoustic waves in solids

Just as we can only see a tiny part of the frequency range of the electromagnetic spectrum, human hearing is only a small fraction of the frequency range of the full acoustic wave spectrum. In each case the full spectrum can be described by one theory, the theory of electromagnetic waves for optics and the theory of stress waves in material media for acoustics.

Sound waves propagate in a variety of media, including gas, liquids, and solids. In solid materials there a two basic types of acoustic waves. One type is a longitudinal wave (see Figure 1.1a), in which the displacement is parallel to the wave vector. The velocity depends on the material, but is typically between 5000 to 10 000 m/s. The second basic wave type is the transverse (shear) wave, in which the displacement is normal to the wave vector (see Figure 1.1b). These waves generally have a lower velocity of typically 3000 to 6000 m/s. Waves can also propagate with a combined longitudinal and shear motion. The waves discussed up to now are called bulk acoustic waves (BAW's), meaning they can propagate freely in the bulk, as if in an infinite medium.

If the propagation medium is bounded, acoustic waves are mainly governed by the boundary conditions. When the wavelength is no longer much smaller than the dimensions of the medium, the boundary conditions define the propagating waves. The most common boundary conditions are surfaces and plates. A summary of some important wave types possible in solids is shown in Table 1.1.

Medium	**Acoustic Wave Types in Solids**	**Displacement**
Bulk	Longitudinal wave	Parallel to wave direction
Bulk	Transverse (Shear) wave	Perpendicular to wave direction
Surface	Rayleigh wave	Elliptical orbit close to surface in x-z plane
Plate	Lamb Wave	Elliptical orbit in x-z plane symmetrically or anti-symmetrically throughout plate thickness

Table 1.1: Wave types and their characteristic particle displacement.

One wave of great interest for electronics is the surface acoustic wave (SAW). The wave is guided along the surface, with its amplitude decaying exponentially with depth. Displacements result from both longitudinal and transverse motion to create an elliptic orbit. These waves are exploited to make SAW filters and also for surface inspection in ultrasonic imaging. This wave type was first proposed by Rayleigh to explain wave propagation during earthquakes.

Lamb waves can only be generated in structures a few wavelengths thick. As with surface acoustic waves, Lamb waves are a combination of longitudinal and transverse waves. There are two families of lamb waves, symmetric lamb waves have a symmetry plane in the middle of the plate and anti-symmetric lamb waves where both the top and bottom surface of the plate move in the same direction (see Figure 1.2). The velocity of these waves depends on the relationship of wavelength to plate thickness.

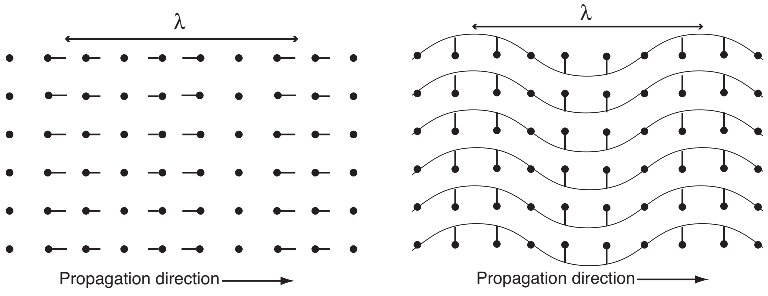

(a) (b)

Figure 1.1: Schematic of acoustic waves in an infinite solid (a) longitudinal mode (b) transverse (shear) mode. Dots represent particles at rest and lines indicate instantaneous position when a wave is present. After Weigel [1].

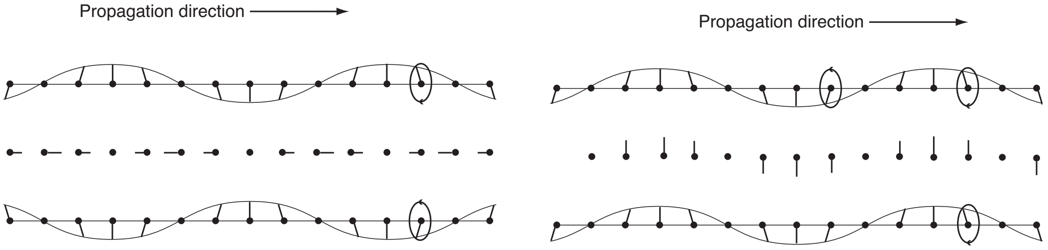

(a) (b)

Figure 1.2: Schematic of lamb waves in a plate (a) symmetric lamb wave (b) anti - symmetric lamb wave. Dots represent particles at rest and lines indicate instantaneous position when a wave is present.

1.1.2 Piezoelectricity

In most of the applications, piezoelectric materials are used to generate and detect acoustic waves. The lattice of a piezoelectric material is characterised by the absence of an inversion symmetry. Applying an electric field to this materials changes the mechanical dimensions. Conversely, applying a mechanical constraint an electrical field is generated.

In a piezoelectric the elastic and electrical parameters are coupled in a bilinear term. If the electric field E_i, stress T_{ij} and temperature θ are taken as independent variables the appropriate thermodynamic potential is the Gibbs free energy G of a dielectric:

$$G = U - \sigma\theta - S_{ij}T_{ij} - D_iE_i \tag{1.1}$$

where U is the internal energy of the system, σ the entropy, S_{ij} the strain and D_i the dielectric displacement. The differential free energy dG reads as:

$$dG = -\sigma d\theta - S_{ij} dT_{ij} - D_i dE_i \tag{1.2}$$

For small enough variables T_{ij} and E_i, the integral form can be expressed in bilinear terms as:

$$\tilde{G} = -\frac{1}{2} s^E_{ijkl} T_{kl} T_{ij} - \frac{1}{2} \varepsilon^T_{ij} E_i E_j - d_{ijk} T_{kl} E_i \tag{1.3}$$

when d$\theta = 0$. From this relation the dielectric, elastic and thermal equations of state can be written and from their differential form the compliances are obtained [2, 3]. The compliance coefficients relate different fields with each other, the most important ones are defined as the elastic compliance relating stress to strain, the permittivity relating displacement to electric field, piezoelectric constants relating stress/strain to displacement/electric field, pyroelectric constants relating displacement to temperature and thermal expansion coefficients relating strain to temperature [2]. With these definitions and with the more practical case of the temperature being constant the adiabatic piezoelectric equations can be derived:

$$S_{ij} = -\frac{\partial \tilde{G}}{\partial T_{ij}} = s^E_{ijkl} T_{kl} + d_{kij} E_k \tag{1.4}$$

$$D_i = -\frac{\partial \tilde{G}}{\partial E_i} = d_{ijk} T_{jk} + \varepsilon^T_{ij} E_j \tag{1.5}$$

with the compliance coefficients as described above: the elastic compliance s_{ijkl}, the piezoelectric constant d_{ijk} and the permittivity or dielectric constant ε_{ij}. It is important to note that the boundary conditions play a crucial role in the resulting response of the material, the difference of the dielectric permittivity at constant stress or constant strain can be considerable. The same applies for the electrical boundary conditions (electric field or displacement constant). It is often useful to use the strain S as independent variable. This leads to the following equations of state:

$$T_{ij} = c^E_{ijkl} S_{kl} + e_{kij} E_k \tag{1.6}$$

$$D_i = e^E_{ijk} S_{jk} + \varepsilon^T_{ij} E_j \tag{1.7}$$

where c_{ijkl} is the stiffness tensor and e_{kij} the piezoelectric tensor.

1.1.3 Bulk acoustic wave resonators

Since the velocity of acoustic waves in solids is small as compared to electromagnetic waves, resonators based on acoustic standing waves with very small sizes can be built. The thickness mode resonance of BAW in a thin uniform plate of thickness t is given when:

$$f = \frac{N \cdot v}{2t} \qquad N \in \{1, 3, 5...\} \tag{1.8}$$

with f the resonance frequency, v the wave velocity. Waves can be generated by applying a voltage on the piezoelectric material. The construction principle of such a resonator is shown in Figure 1.3. What is needed is an acoustically isolated piezoelectric layer (piezolayer) with a top and bottom electrode. The piezoelectric tensor of the piezolayer has to be suitably oriented with respect to the electrodes. A longitudinal acoustic wave can be generated in a piezolayer with the piezoelectric coefficient d_{33} perpendicular to the electrodes by applying a AC voltage. If the frequency is chosen correctly the layer will resonate between the two electrodes. The contour mode wave that could also be excited in the piezoelectric cannot follow at the frequencies of resonance for the thickness mode, since the thickness, t, is a lot smaller than the width, a, of the resonator. This means that the film can be assumed to be clamped in x and y directions, and free to move in z direction.

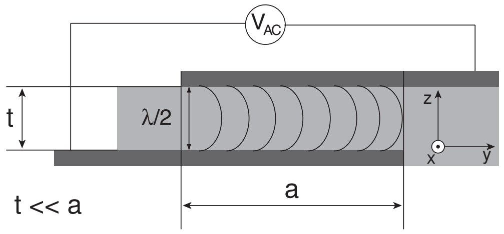

Figure 1.3: Schematic of a bulk acoustic resonance in a piezoelectric plate. The vertical dimension is exaggerated for the sake of clarity. The pressure amplitude for the fundamental mode is sketched in the vibrating part of the device.

Longitudinal sound waves in solids typically amount to 5'000 to 10'000 m/s. Evaluating Equation 1.8 for a practical thin film thickness of 0.1 to 5 μm, resonance frequencies in the range of 0.5 to 50 GHz are calculated. This covers the interesting range of 0.5 to 15 GHz in which ultrasonic resonators are superior to digital and pure electromagnetic solutions.

1.1.4 Types of bulk acoustic wave resonators

There are different approaches to obtain an acoustically isolated piezolayer. Figure 1.4 shows three possible device configurations based on thin films as the piezoelectric material. The first approach is a membrane structure supported at the edge by the substrate. The fabrication steps involve deposition of the piezoelectric film on a supporting substrate and removal of a portion of the substrate to create membranes. Since the acoustic impedance (defined as $Z_A = \rho \cdot v$ where ρ is the density and v the sound velocity) of air is a lot lower than of a solid, most of the energy is reflected at the air/solid boundary. Another approach, also using air to reflect the acoustic wave, is to micromachine the surface. By depositing a sacrificial layer before deposition of the piezolayer with its electrodes and removing this layer as the last step, an air gap under the resonator can be created. A quite different approach is the SMR (solidly mounted resonator) since the resonator is fixed to another solid. The acoustic isolation can be achieved by using an acoustic mirror. The acoustic mirror is made by alternating quarter wavelength thick films of a high and a low acoustic impedance. At each boundary between the high and low impedance layers a large percentage of the wave will be reflected and will sum up to the correct phase due to the $\lambda/4$ thickness of the layers. The result is a practically isolated acoustic resonator in a certain wavelength interval around λ.

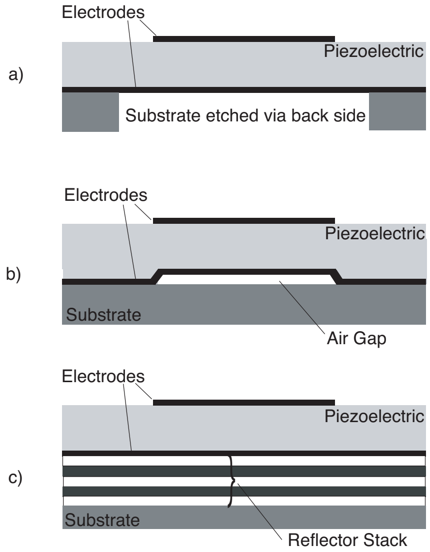

Figure 1.4: Configurations for thin film resonators. (a) Membrane formed by etching from the back side of the substrate. (b) Resonator isolated by an air gap. (c) Solidly mounted resonator using an acoustic reflector stack.

1.1.5 Bulk acoustic wave resonator applications

Thin film bulk acoustic wave resonators (TFBARs) are combined in order to fabricate BAW-filters. TFBARs can be used in filter design as bandpass filters or image rejection filters (narrow passband with signal rejection at adjacent lower frequencies). Passband filters may be realised with electrically coupled TFBARs using a ladder or lattice topology or may also apply acoustically coupled resonators which are stacked on top of each other. As an example, the construction principle of a ladder filter is shown in Figure 1.5 and its working principle in Figure 1.6. In ladder filters two groups of resonators are used, series resonators and shunt resonators. The series resonators are the resonators connected in series in the circuit diagram. All the series resonators have the same resonance frequency $f_{s,series}$ and the all the shunt resonators have a resonance frequency $f_{s,shunt}$, shifted down by adding an additional layer on these resonators. In the center of the passband the series resonators are at minimum impedance and thus let the signals pass, whereas the shunt resonators are at maximum impedance and thus will not shunt the signal.

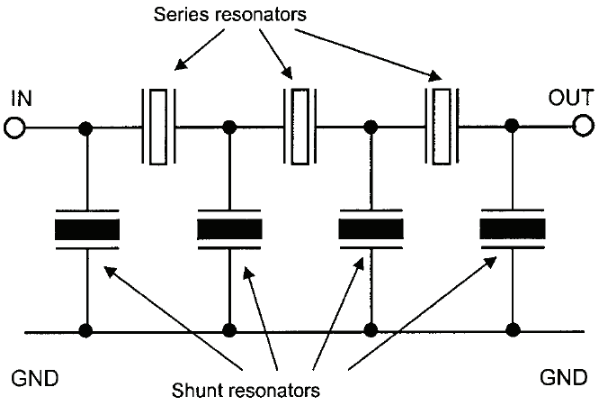

Figure 1.5: Topology of $3\frac{1}{2}$-stage ladder filter (After Aigner [6]).

Another way of realising bandpass filters is by lateral acoustic coupling of thickness- or shear-mode resonance. Grudkowski *et al.* [4] demonstrated in 1980 the laterally coupled, thin film Monolithic Crystal Filter (MCF) with 8.5 dB insertion loss and 40 dB rejection. Bandpass filters can also be realised by stacking two resonators which couple acoustically in the thickness mode. A large out-of-band rejection is achieved because of the grounded middle electrode. Lakin *et al.* [5] introduced the thin film Stacked Crystal Filter (SCF) in 1986, as well as the electrically coupled ladder filter.

The characteristics of these filters (see Figure 1.7) are highly dependent on the properties of the piezoelectric layer. While some parameters are a matter of design, insertion loss

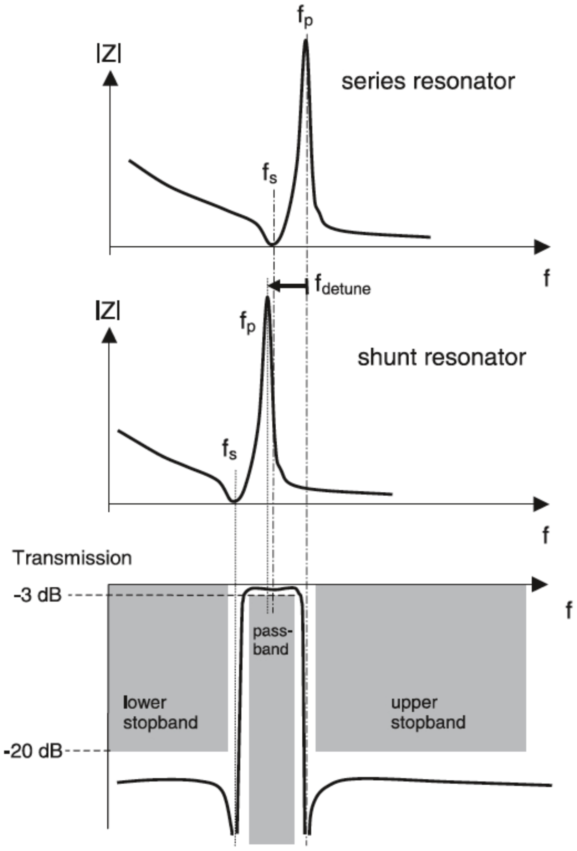

Figure 1.6: Working principle of a ladder filter (After Aigner [6]).

and bandwidth are ultimately defined by the acoustic and piezoelectric properties of the piezolayer. Depending on the application the demands on the filter characteristics differ. The main applications of RF-filters are mobile phones (400 MHz to 2.2 GHz), global positioning systems (GPS, 1.575 GHz), WLAN (Wireless Local Area Network) and short range systems such as Bluetooth and cordless phones [6]. The main types of RF-filters are ceramic filters, SAW and BAW filters. Since wireless systems continue to be miniaturised, the requirements on these filters increase. SAW technology provides high performance filters, avoiding the too large ceramic (dielectric) filters, but the tendency to go to higher frequencies is pushing this technology to its limits. Figure 1.8 shows the frequency range where BAW technology is interesting. BAW technology is needed at high frequencies where a small size and high performance are required. The performance of a filter can be judged by its power handling capabilities, size, the steepness of the filter skirts and insertion loss.

High coupling materials are needed for applications where a large bandwidth is demanded. Materials used currently as the piezoelectric in BAW resonators and materials being considered for future use shall be discussed in the following section.

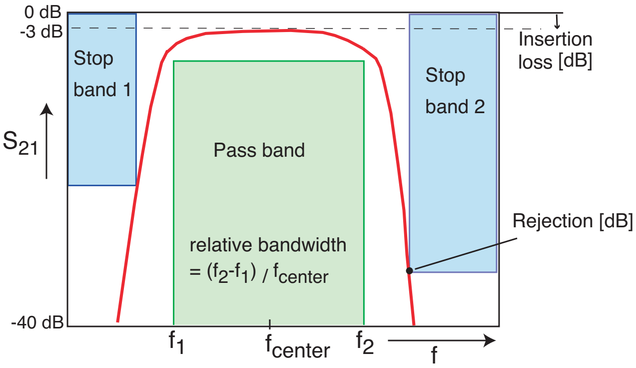

Figure 1.7: Schematic showing the main characteristic of a RF-frequency filter (After Aigner [7]).

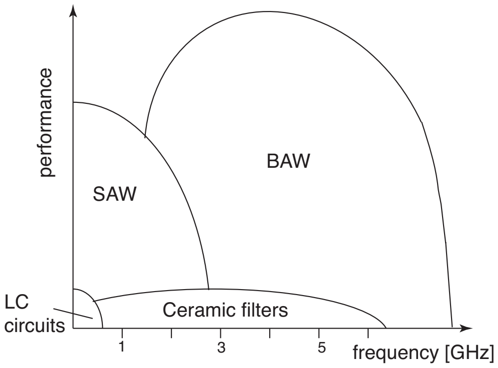

Figure 1.8: RF frequency range vs. performance of RF filters showing the frequency range where BAW technology is of interest (After Aigner [7]).

1.2 Materials used for thin film BAW devices

1.2.1 Material considerations for the piezoelectric layer

Ideally, the piezoelectric layer for thin film resonators should be a high quality single crystal, having a single orientation. On most substrates suitable for device microfabrication the deposited films are polycrystalline. Nonetheless high quality textured thin films with a columnar structure can be made to meet the requirements on TFBARs for telecommunication applications. The materials parameters of the piezoelectric layer that need to be considered for TFBAR applications shall be briefly described.

Piezoelectric coupling coefficient k_t^2

The piezoelectric coupling coefficient for thickness extensional mode k_t^2 is a dimensionless measure of electromechanical energy conversion efficiency of this mode. It is determined by the piezoelectric, elastic and dielectric constants as:

$$k_t^2 = \frac{e_{33}^2}{c_{33}^D \varepsilon_{33}^S} \tag{1.9}$$

where e_{33} is the piezoelectric constant, c_{33}^D is the elastic stiffness at constant electric displacement and ε_{33}^S is the clamped dielectric permittivity. The conversion efficiency is naturally bounded to $0 \leq k_t^2 < 1$. The coupling factor is important since it defines the maximum achievable bandwidth.

Acoustic velocity v_D

The acoustic velocity (or sound velocity) of the longitudinal mode along the polar axis 3 is given by

$$v_D = \sqrt{\frac{c_{33}^D}{\rho}} \tag{1.10}$$

and defines the resonance frequency of a slab cut perpendicular to the polar axis 3 (according to Equation 1.8). The velocity depends primarily on the elastic stiffness c_{33}^D and the mass density ρ of the material and to a lesser extent on the piezoelectric properties of the medium through the piezoelectric contribution to the elastic stiffness [8]:

$$\begin{aligned} c_{33}^D &= c_{33}^E + \frac{e_{33}^2}{\varepsilon_{33}^S} \\ \text{or } \; c_{33}^E &= c_{33}^D \cdot (1 - k_t^2) \end{aligned} \tag{1.11}$$

Acoustic loss

The material limited losses in acoustic materials can be expressed by the motional time constant [9]:

$$\tau_1 = \frac{\eta}{c_{33}^D} \tag{1.12}$$

which is dependent on the acoustic viscosity η and the elastic stiffness of the film. This quantity can also be seen as the imaginary part of the elastic constants proportional to the viscosity:

$$c_{33}^D{*} = c_{33}^D + i\omega\eta_{33}^D = c_{33}^D(1 + itan\gamma) = c_{33}^D(1 + i\omega\tau_1) \tag{1.13}$$

The mechanical quality factor of the piezoelectric layer can then be written as:

$$Q = \frac{1}{\tan\gamma} = \frac{1}{\omega\tau_1} \tag{1.14}$$

A high quality factor (Q-factor) is needed in order to limit damping of the wave. The effective Q-factor of a resonator also depends on other features of the device, such as resistive losses in electrodes.

Dielectric constant ε_r

The impedance level of a resonator is determined by the resonator size, the thickness of the piezolayer and the dielectric constant. A high dielectric constant allows for reduction of the resonator size at a given frequency. The dielectric constant in z direction of a clamped film is denoted $\varepsilon_{33,f}$.

Attractive materials for TFBARs exhibit high Q-factors and for RF applications in addition a high k_t^2.

1.2.2 AlN and ZnO

Both AlN and ZnO have a wurtzite structure and show a longitudinal piezoelectric response along the [0001] direction. To obtain good piezoelectric coefficients columnar grains with a (0001) texture with the same polar direction are needed. High quality films can be produced by reactive magnetron sputtering. Relevant properties of AlN and ZnO are shown in Table 1.2, together with PZT for comparison. Both AlN and ZnO meet the material property requirements to produce RF-filters for mobile communications. However AlN has some advantages. One important advantage is its compatibility with silicon semiconductor technology, whereas ZnO is more problematic. AlN has lower dielectric losses and higher thermal conductivity, which means it can handle higher power levels, whereas ZnO has high dielectric losses and tends to have a low resistivity [9, 10]. In conclusion TFBARs based on AlN meet the specifications needed for mobile communications and so far ZnO has not been demonstrated as a feasible alternative.

1.2.3 PZT solid solution system

The lead zirconate titanate system is commonly used in resonators, but as a ceramic material at low frequencies for example for medical applications at 3 to 10 MHz. PZT in thin film form has found applications in sensors and actuators due to its high piezoelectric constants. Resonators based on PZT thin films have not been commercialised yet. Pb(Zr$_x$,

Coefficients	**ZnO**	**AlN**	**PZT**
Longitudinal sound velocity v_D along direction 3 [m/s]	6350	11000	4000...6000
Dielectric constant ε_{33}^S	10.9	10.5	200...1300
Dielectric losses $\tan\delta$	0.01...0.1	0.003	0.01...0.03
Piezoelectric constant $d_{33,f}$ [pm/V]	5.9	3.9...5.1	60...130
Stiffness c_{33}^D [GPa]	208	395	90...160
Acoustic losses	low	low	high

Table 1.2: Comparison of piezoelectric materials for TFBARs. Values from references [6,10,11].

$Ti_{1-x})O_3$ is a solid solution of lead titanate ($PbTiO_3$) and lead zirconate ($PbZrO_3$) with a perovskite structure. At room temperature, the system Pb(Zr_x, Ti_{1-x})O_3 is tetragonal for x = 0-0.53 and rhombohedral when x > 0.53 [3, 12]. In the tetragonal case the ferroelectric polarisation points along the ⟨001⟩ direction, in the rhombohedral case it points along the ⟨111⟩ direction. A schematic of the tetragonal perovskite structure is shown in Figure 1.10. The lead zirconate titanate ($PbZrO_3$ - $PbTiO_3$) phase diagram is shown in Figure 1.9 [13]. The narrow region where these two symmetries meet, at a Ti/Zr ratio of 53/47, is called the morphotropic phase boundary (MPB). At or near this boundary, many properties peak: the piezoelectric coefficients, the coupling coefficient and the relative permittivity. The high values of these parameters are exploited in many applications such as sensors, transducers and applications in the field of microelectromechanical systems (MEMS). These high values of piezoelectric coefficients at the morphotropic phase boundary are due to the presence of both rhombohedral and tetragonal phases, which enhances the possibilities of polarisation orientation. Or, according to newer theory, the existence of a monoclinic phase in which the polarisation can be rotated with almost no anisotropy in the {110} plane [14]. PZT thin films with a tetragonal composition are one of the main candidates for non-volatile memory applications due to their large remanent polarisation.

The properties of PZT thin films are sensitive both to the composition of the system and to the crystallographic orientation of the film. This means that films can be tailored to suit the requirements of a certain application. However as will be shown in the following Chapters these properties are correlated and cannot be adapted independently. In practice this means that certain compromises need to be made when choosing the composition and orientation of the PZT film.

For BAW applications, when compared to AlN and ZnO, PZT offers larger coupling co-

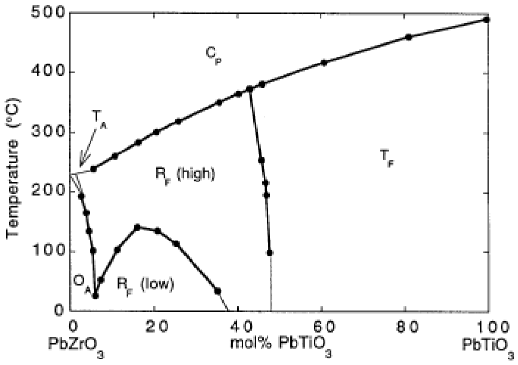

Figure 1.9: Phase diagram of the Pb(Zr$_x$, Ti$_{1-x}$)O$_3$ solid solution. The morphotropic phase boundary separates the tetragonal and rhombohedral ferroelectric phases. The subscripts A and F stand for antiferroelectric and ferroelectric phases, the letters C, T, R and O stand for cubic, tetragonal, rhombohedral and orthorombic phases. After Jaffe [13].

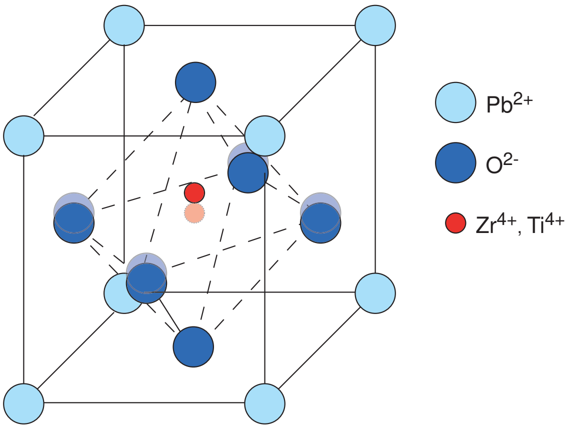

Figure 1.10: Schematic of the tetragonal PZT unit cell with a perovskite structure. Semitransparent circles indicate equilibrium position of the cubic perovskite structure. The displacement of the centre ion and the surrounding oxygen ions creates a dipole.

efficients, leading to larger bandwidth, lower sound velocity, which means thinner films for a given frequency and higher dielectric constants, reducing resonator areas. PZT is of interest for BAW resonator applications with frequencies around 1-2 GHz, since these frequencies require very thick films for materials such as AlN. In addition tailoring of its properties to meet the requirements is easier, due to the composition, orientation also doping control is possible, as discussed above. The main drawback of PZT for BAW applications are the material losses, which shall be discussed in detail in Section 1.4 .

1.3 State of the art of PZT in BAW resonators

The high coupling material PZT is a promising material for applications where a wider bandwidth is needed. The three main methods for making high quality PZT thin films are sputtering, sol-gel deposition and metal-organic vapour deposition (MOCVD). It appears that the latter technique was mostly used for memory applications and rarely for RF applications. Pb(Zr_x, Ti_{1-x})O_3 thin film based resonators have been studied by various groups. In this section historical developments and the state of the art of PZT thin film resonators shall be summarised and discussed.

First studies of bulk acoustic properties of PZT thin films were performed by Sreenivas *et al.* in 1988 [15]. Their films fabricated using a co-sputtering technique had varying compositions from rhombohedral to tetragonal and were randomly oriented. They observed the acoustic pulse trains using a wideband pulse echo system and used a reflection scanning acoustic microscope (SAM) to observe wave velocities. They found that the surface acoustic wave (SAW) attenuation of their films is very high and attributed this to the micro-pores or surface protrusions present in their films. The high density of surface defects and high electrical conductivity of their films were observed by the SAM and showed that surface roughness and high dielectric losses are not ideal for acoustic applications.

The first application of PZT thin films in a TFBAR was reported by Yamaguchi *et al.* [16] and Hanajima *et al.* [17] in 1997, who studied the ultrasonic properties of sol-gel deposited PZT films in UHF-SHF ranges (UHF - ultra high frequency 300 MHz to 3GHz, SHF - super high frequency 3 GHz to 30 GHz). Yamaguchi showed a resonator consisting of a Si/SiO_2/Ti/ Pt/ Pb($Zr_{0.53}$, $Ti_{0.47}$)O_3/Al membrane with a PZT film thickness of 0.8 μm, had a resonance at 1.7 GHz (thickness of residual Si 12 μm). They found a quality factor of 84 at antiresonance and 50 at resonance frequencies. From transducer impedance measurements the coupling constant k_t^2 was estimated to be around 16% at 730 MHz for a film thickness of 2.65 μm [16]. Hanajima *et al.* studied the same structure and observed a mechanical quality factor (Q-factor) of 237 and a coupling constant k_t^2 of 9.6% at an applied voltage of 15.3 V [17]. Sol-gel films were further studied by Arscott *et al.* [18]. They studied resonators both on Si and GaAs substrates. For the Si substrates they used electromechanical polishing to achieve a wedge shape of the substrate and then measured, where approximately 10 μm of Si remained. The results were reported for the devices consisting of Si/SiO_2/Ti/Pt/Pb($Zr_{0.53}$, $Ti_{0.47}$)O_3/Pt with a PZT thickness of 0.4 μm. They stated the fundamental parallel resonance to be at 0.1 GHz with a effective electromechanical coupling constant k_t^2 of 49% and a QF (product of quality factor and frequency) of 10^{11} Hz. The resonance frequency in this work does not correspond to the thickness of the film, thus the high coupling constant and quality factor reported are doubted.

Note that the publications mentioned up to now all used PZT with a composition at the morphotropic phase boundary. Loebl *et al.* [19] continued studying sol-gel PZT in BAW devices, but this time with a tetragonal composition of $Pb_{1.1}(Zr_{0.35}, Ti_{0.65})O_3$. They reported results for a resonator with the thickness of the piezoelectric layer of 1.3 μm , resulting in a resonance frequency of 0.9 GHz. Another difference of this work compared to previous works is that the structure was a SMR using a ceramic SiO_2 layer. They found they could reach a coupling constant k_t^2 up to 25% by using appropriate poling conditions and a Q-factor of 67. They specified that large acoustic losses need to be introduced when modelling the data, the introduction of dielectric losses was found not to be sufficient. Further work on tetragonal sol-gel PZT films was published by Su *et al.* [20] using the membrane structure again and a $Pb(Zr_{0.30}, Ti_{0.70})O_3$ film with a thickness of 0.75 μm. From the resonance, observed at around 1.6 GHz, a quality factor of 54 and a coupling constant k_t^2 of 19.8% were derived. They also reported values for filter bandwidths of ladder filters based on PZT films and found a bandwidth of 100 to 120 MHz at a centre frequency of 1.6 GHz, which is larger than the bandwidths for ZnO-based filters. In 2002 another method to obtain the TFBAR structure using surface micro-machining was presented by Cong *et al.* [21]. They used a SiO_2 layer to adjust the resonance frequency. But this work mainly concentrates on the fabrication techniques of the devices and there is little information on the PZT layer. They reported only the thickness of 0.5 μm resulting in central frequencies of the obtained filters from 1.7 to 2 GHz.

Since homogeneous films of sputtered PZT are difficult to achieve, first TFBARs using sputtered films of the PZT family are based on the binary oxides system $PbTiO_3$ (PT). Misu *et al.* [22] developed a TFBAR structure with a membrane consisting of Si/ SiN/ Ti/Pt/ $PbTiO_3$/ Ti/ Pt, with a PT layer thickness of 0.9 μm. The resonance is observed at 1.4 GHz with a coupling constant k_t^2 of 4% and a Q-factor of 70. Further work on this system, which studied the lanthanum doping of the PT layer resulted in a coupling constant k_t^2 of 1% and a Q-factor of 100. The lanthanum improved the Q-factor by reducing the number of pores, but the crystallinity of the film and thus the coupling constant decreased [23]. Later they reported values of 11% for the coupling constant k_t^2 and 70 for the Q-factor for resonators containing slightly more lanthanum [24].

The first reports of sputtered PZT in TFBARs were not published until 2004. Park *et al.* [25] use a magnetron sputtering with a PZT single target to make $Pb(Zr_{0.53}, Ti_{0.47})O_3$ films with thicknesses of 0.5 μm, 1 μm and 2 μm on $Si/TiO_2/Pt$ substrates. The orientation of the films was random and scanning electron microscopy (SEM) images showed porous films. They obtained resonance frequencies of 1.48, 1.01 and 0.71 GHz for the thicknesses 0.5 μm, 1 μm and 2 μm, respectively. No information on coupling constant or quality factor of the devices is given. Further results on resonators based on sputtered PZT with compositions around the morphotropic phase boundary were reported by Zinck *et al.* [26]. Similar to the previous work single target magnetron sputtering was used and the obtained films were randomly oriented. Here the SEM showed a dense microstructure of the films and the piezoelectric constant d_{33} was reported to be about 30 pm/V at 200 kV/cm. The resonance frequency was 1.4 GHz for a PZT film thickness of 0.6 μm. The maximum Q-factor was found for the parallel resonance and was measured to be 85. By observing the influence of bias voltage on the device they found the coupling coefficient could be increased from 4.1% to 7.3% and also noticed the variations of both resonance and antiresonance frequencies. Schreiter *et al.* [27] had previously mentioned that PZT films with a composition at the morphotropic phase boundary should show this behaviour.

Note that the publications described up to this point do not report films with a preferential orientation, some XRD diffraction patterns are shown, but they are used to check phase purity. The first results of textured PZT films in BAW resonators were reported by Schreiter *et al.* [27] and Larson *et al.* [28]. In Ref. [27] the properties of sputtered (111) textured Pb(Zr$_x$, Ti$_{1-x}$)O$_3$ films with a composition ranging from x = 0.25 to 0.6 were studied. They used reactive magnetron sputtering of multiple metallic targets to deposit the films. The films thickness ranged from 0.35 to 0.425 μm to produce a resonance frequency around 2 GHz and the SMR structure of the resonators was based on a Pt/ZnO acoustic mirror stack. They reported the coupling constant k_t^2 for five compositions from x = 0.25 to 0.58 and found it increased from 4.4% for the tetragonal symmetry to 9% for rhombohedral symmetry. The Q-factor for the 25/75 PZT resonators was reported to be 220 for the series resonance. They observed strong bias dependencies of the parallel resonance for the tetragonal films and the series resonance for the rhombohedral films. The films studied in this work have the most similarities to the films presented in this thesis and their results shall be discussed in detail in Section 3.4. Further work on sputtered tetragonal films, this time with a {100} texture was presented by Larson *et al.* [28]. They used a ceramic target to produce Pb(Zr$_{0.40}$, Ti$_{0.60}$)O$_3$ films with a thickness of 1.4 μm. The measurements of this film were performed on an unreleased TFBAR, which means the last step of removing the silicon has not been accomplished. In the same publication [28] they also presented films deposited by metal-organic vapour deposition (MOCVD), sol-gel deposition and jet vapour deposition (JVD). The JVD films were also evaluated on unreleased resonators, whereas the MOCVD and sol-gel films were measured in 'released' TFBARs. They extracted values for the coupling constant k_t^2, the Q-factor and also for the relative dielectric constant, dielectric losses and acoustic attenuation. They tried to compare the different deposition methods. Although this is difficult since films have different compositions and film orientations, their conclusion was reasonable: the acoustical attenuation and thus Q-factor are mainly dependent on the microstructure and the most desirable films are columnar and smooth. The values of coupling coefficient and Q factor for these for four different devices are shown in Table 1.3.

Table 1.3 gives a summary of BAW resonators based on PZT films. Values for the dielectric constant were included when stated in the respective publication. The figure of merit (FOM) is simply the product of $k_t^2 * Q$ and gives an indication of the performance of the resonator. It can be seen that the highest FOM values have been achieved by Hanajima [17] using sol-gel PZT films and by Larson with sputtered PZT films [28]. As illustrated in Figure 1.11 from the experimental data it seems as if increasing the coupling constant k_t^2 means decreasing the Q-factor and vice versa.

1.4 PZT Materials Losses and Domain Considerations

1.4.1 PZT Materials Losses

Losses in piezoelectric materials can be divided into three components: dielectric, mechanical (or elastic/acoustic) and piezoelectric losses. The dielectric displacement as a function of electric field, strain as a function of stress and the strain as a function of electric field or stress as a function of dielectric displacements are not necessarily hysteresis free linear relations as shown in Figure 1.12 [29]. The effects may have a delayed time response resulting in hysteretic behaviour with related losses of the coupling energy. To include these losses in the piezoelectric equations, the dielectric, elastic and piezoelectric constants can be written as complex components:

$$\varepsilon^T = (\varepsilon^T)' - i(\varepsilon^T)'' = \varepsilon^T(1 - i * \tan\delta) \tag{1.15}$$

$$s^E = (s^E)' - i(s^E)'' = s^E(1 - i * \tan\phi) \tag{1.16}$$

$$d = d' - id'' = d(1 - i * \tan\eta) \tag{1.17}$$

It is well known that the relative dielectric constant is frequency dependent. The dispersion of the dielectric function can be divided into the following contributions: electronic polarisation, ionic polarisation, orientation polarisation, space charge polarisation and domain wall polarisation [30]. Each contribution leads to dielectric losses, which are described by

Table 1.3: Overview of literature results for PZT in BAW resonators

Date	**Author**	**Growth method**	**Device type**	**Zr/Ti ratio**	**Film thickness (μm)**	**Res. freq. (GHz)**	**Film orientation**	k_t^2	$\varepsilon_{33,f}$	**Q**	**FOM**	**Ref.**
2004	Larson	MOCVD	FBAR	30/70	0.4	2.1	111	22	420	30	6.6	[28]
		sol-gel	FBAR	30/70	2.3	0.6	100	35	330	45	15.8	
		sputtering	FBAR (unreleased)	40/60	1.4	1.1	100	17	470	125	21.3	
		JVD	FBAR (unreleased)	50/50	1.9	0.8	100	5	430	22	1.1	
2004	Schreiter	sputtering	SMR	25/75	0.35 - 0.43	2	111	4.4	285	220	9.7	[27]
2004	Zinck	sputtering	FBAR	52/48	0.2-0.8	1.4	random	7	700	85	5.95	[26]
2004	Park	sputtering	FBAR	53/47	0.5/1/2	1.5/1/0.75	random		650-950			[25]
2002	Cong	sol-gel	FBAR		0.5	1.7-2						[21]
2001	Su	sol-gel	FBAR	30/70	0.75	1.5		19.8		54	10.7	[20]
2001	Loebl	sol-gel	SMR	35/65	1.3	0.9	100 + 111	25	556	67	16.8	[19]
1998	Arscott	sol-gel	FBAR	53/47	0.4	0.1	111 + 100	49	1080			[18]
1997	Hanajima	sol-gel	FBAR	52/48	0.8	1.7		9.61		237	22.8	[17]

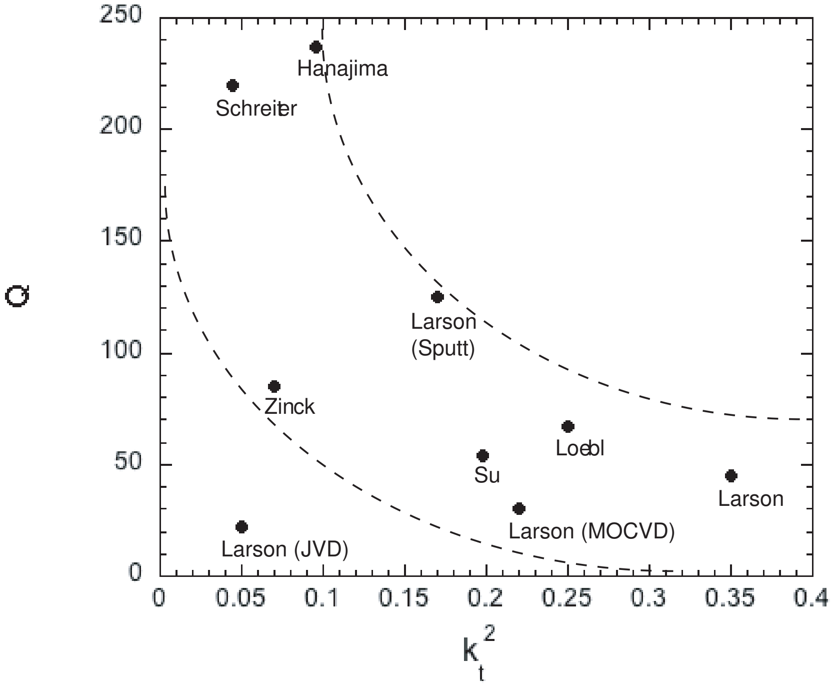

Figure 1.11: Literature data for coupling constant k_t^2 vs. Q-factor for PZT resonators. Dotted lines indicate possible correlations between the two values. Growth method is by sol-gel unless otherwise indicated.

the loss tangent $\tan\delta$. The elastic and piezoelectric losses are less studied and mechanisms of loss less well known. Haerdtl *et al.* [31] proposed four mechanisms for electrical and mechanical losses: A portion due to domain wall motion, a fundamental lattice part, a micro-structural portion and a conductivity portion. The losses due to domain wall motion are thought to be the main contribution for ferroelectric materials [31] and shall be addressed in more detail in the following paragraph. Piezoelectric losses were not mentioned in Ref. [31] and are often neglected since they are small according to Xu [3]. In general the difference is made between intrinsic losses, which are due to the lattice, and extrinsic losses, due to non-lattice contributions. Uchino *et al.* [29] explain how to measure dielectric, elastic and piezoelectric losses and how to separate intrinsic and extrinsic contributions. Experimental data of the contributions to intrinsic and extrinsic dielectric, elastic and piezoelectric losses for soft and hard PZT ceramics were reported by Tsurumi *et al.* [32]. Values are reported for intrinsic and extrinsic contributions to the losses for soft and hard PZT. It was observed that both for soft and hard PZT, dielectric losses are mainly intrinsic. The observation that the elastic loss is much larger for soft than for hard PZT (one order of magnitude), indicates a strong contribution of extrinsic losses,

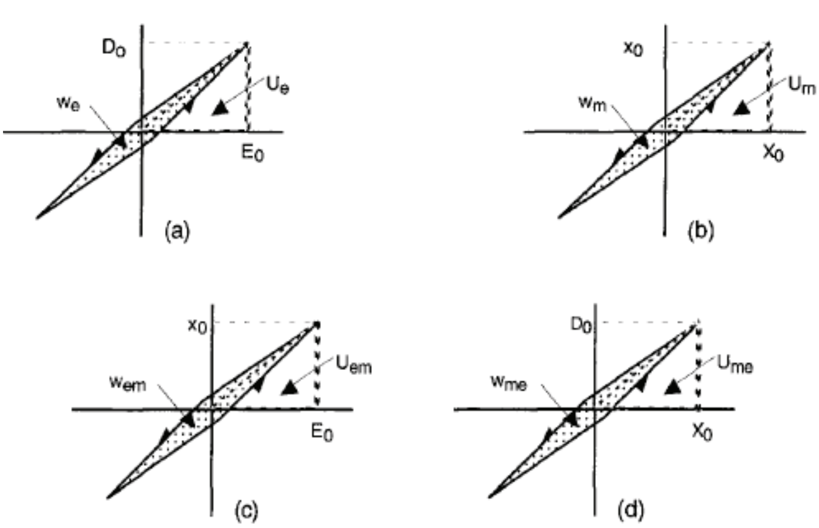

Figure 1.12: (a) D vs. E (stress free), (b) S vs. T (short-circuit), (c) S vs. E (stress free), and (d) D vs. T (open-circuit) curves with a slight hysteresis in each relation. After Uchino *et al.* [29]

but the ratio's of intrinsic/extrinsic losses are reported to be 87% for the soft and 79% for the hard PZT, which does not confirm this assumption. For the piezoelectric losses a higher contribution of the extrinsic mechanisms is found, around 50% for both hard and soft PZT. They conclude that domain wall pinning strongly reduces elastic loss but its effect on dielectric and piezoelectric losses is small.

1.4.2 Ferroelectric Domains and their Contribution to Losses

A ferroelectric is defined as a crystal, which has two or more stable orientations of electrical polarisation, that can be switched by an electric field. At zero electric field, the orientational states differ only in the direction of the polarisation vector [2]. At high temperatures the highest symmetry phase is found, which is non-polar for most ferroelectrics. The Gibbs free energy is then a function of P^2 with an equilibrium value of P^2=0. Below the Curie temperature θ_C, the material becomes ferroelectric, as P^2 becomes larger than zero. This means that if P=P_0 is a solution, the inverted polarisation -P_0 is also a solution. The energetically favourable position for the positively charged ion in the middle of the perovskite structure is no longer in the centre, but a double energy well exists. A schematic of a possible position and the effect of an applied field are shown in Figure 1.13.

If the polar axis originates from a unique symmetry axis of the high temperature phase (as for example a hexagonal axis), P=P_0 and -P_0 are the only solutions and we deal with a uniaxial ferroelectric. If however, the polar axis originates from multiple (n) equivalents axes of the high temperature phase, then we deal with $2n$ possible polarisation directions.

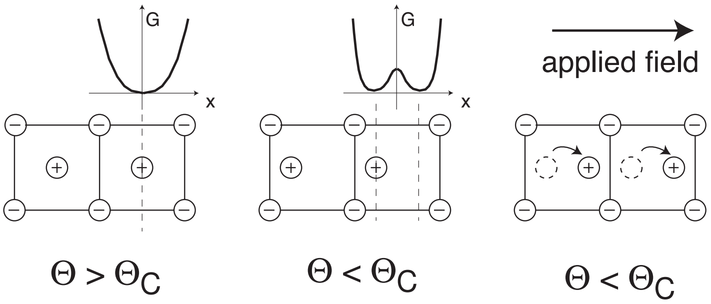

Figure 1.13: Schematic representation of the ferroelectric phase transition and the effect of an external electric field (After Lines and Glass [2]).

A region with only one type of polarisation direction is called a domain. A mono-crystalline region (e.g. grain) that is large enough will generally contain domains of all possible $2n$ kinds in absence of electric fields and mechanical forces. In an electric field, domains tend to grow or shrink in order to minimise the free energy term $-P \cdot E$. To understand the impact of mechanical forces, one has to note that the unit cell dimensions are changed at a ferroelectric phase transition according to the spontaneous strain formed at the transition. It usually means that the unit cell grows along the polar axis, and shrinks perpendicular to it. This leads to so-called ferroelasticity: A multidomain ferroelectric body will develop strains in all directions depending on the domain configuration. This means that external forces may influence the domain configuration. Domain walls at which the polarisation is turned by an angle other than 180° are called ferroelastic domain walls (see Figure 1.14). In the presence of stresses, ferroelastic domain walls adapt to minimise the free energy (the -$S \cdot T$ term).

A particular issue is the depolarisation field due to polarisation charges that exist under certain conditions at domain boundaries. At the surface of a ferroelectric domain polarisation charges appear according to the angle this surface forms with the polarisation, the charge density being the point product of $P \cdot n$, where n is the surface normal pointing outwards. In a multidomain structure these charges are normally compensated by the charges of the neighbouring domains. 180° domain walls do not have charges at all. If the polarisation charges are not compensated at the border of the ferroelectric, not by defects and not by charges in an electrode, then a depolarisation field is formed that opposes the polarisation: $E_{dep} = -P/\varepsilon$. This field increases the free energy potential, with the consequence that domain patterns may be modified. The effect is especially evident in slab shapes when narrow 180° domains are formed to reduce the average depolarisation field in the interior of the material.

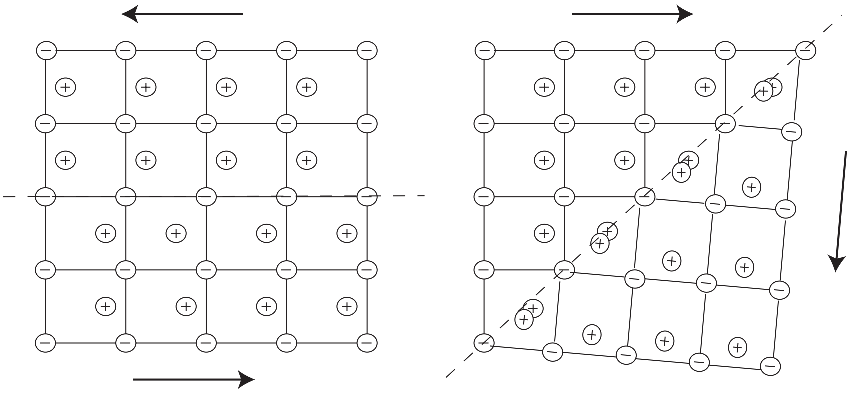

180° domain wall egion

90° domain wall egion

Figure 1.14: Two-dimensional structural models of a 180° and 90° domain wall in a tetragonal perovskite structure. The distortion due to the tetragonal lattice is exaggerated for sake of clarity (After Kittel [30]).

The domain pattern of a crystal can be changed by applying an external electric field. The polarisation will try to align with the electric field. This can be observed by measuring a ferroelectric hysteresis loop with a Sawyer-Tower circuit [33]. The polarisation as a function of the applied electric field of a ferroelectric is shown in Figure 1.15 including the domain configuration. The area within the loop corresponds to the energy to reverse the polarisation twice, this energy can be related to the dielectric loss. Applying an external electric field therefore induces a macroscopic polarisation in a crystal or ceramic by aligning the polarisation in many domains. A schematic drawing of the poling process for thin films is shown in Figure 1.16. In practice a single domain state is difficult to achieve, due to local fields caused by defects (electrical and mechanical) or other mechanical constraints. 180° domain walls are easier to move, since this does not change the elastic energy. The mobility of domain walls will be influenced by several parameters of the material, including grain size, crystal structure and orientation, defects, dopants and external fields and stresses.

From measurements of dielectric, elastic and piezoelectric materials coefficients it is clear that domain wall motion is responsible for the main dependence of these properties on frequency, electric field and temperature [34]. These contributions are called extrinsic since they do not come from the lattice response. Many authors attribute losses of ferroelectric materials to the vibration of ferroelastic domain walls. Arlt *et al.* [35] derive the complex materials constants from the damping of a vibrating domain wall. They assume a poled

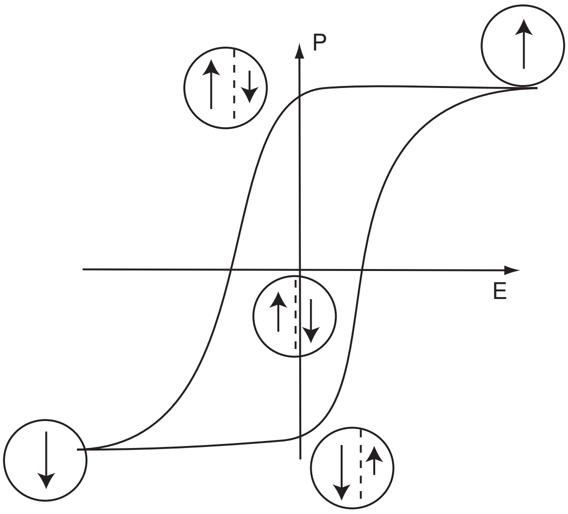

Figure 1.15: Ferroelectric (P-E) hysteresis loop, a schematic representation of the domain configuration is shown in the insets assuming no ferroelastic domains are present (After Damjanovic [34]).

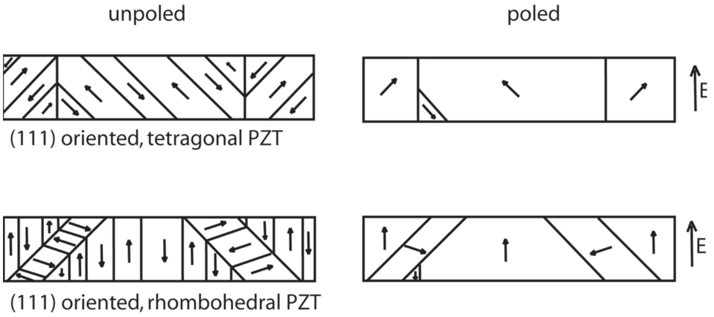

Figure 1.16: Schematic domain states in poled and unpoled tetragonal and rhombohedral PZT thin films.

ferroelectric ceramic with mainly 90° domain walls. They introduce the displacement Δl of the domain wall induced by electric or elastic fields and describe the vibration of a domain wall as:

$$m\Delta l'' + b\Delta l' + k\Delta l = -(\frac{\partial W_E}{\partial \Delta l} + \frac{\partial W_M}{\partial \Delta l}) \tag{1.18}$$

where m is the mass of the domain wall, b the damping constant of the domain wall motion and k the force constant, all per unit area of the domain wall. W_E and W_M mean the total electrostatic energy (e.g $-E \cdot P$), and the total elastic energy (e.g. -$S \cdot T$).

The term of inertia $m\Delta l''$ is neglected, since the measuring frequencies (lower than 10 MHz) are assumed to be a lot lower than the resonance frequency of the domain walls. They thus obtain an expression for the displacement of domain walls as a function of b, k, external electric and stress fields, spontaneous strain and polarisation and a geometrical factor to take the orientation of the domain walls into account. They calculate the change of polarisation and deformation induced by external fields by integrating over the number of walls per volume. Thus the domain wall contribution to the complex materials coefficients dielectric permittivity, elastic and piezoelectric coefficients can be calculated. The losses are found to be dependent on spontaneous polarisation and deformation and on the number of walls per unit volume. They find the elastic losses to be proportional to the square of spontaneous deformation, the dielectric losses proportional to the square of the spontaneous polarisation and the piezoelectric losses proportional to the product of spontaneous polarisation and spontaneous deformation. The calculations of materials coefficients based on this model show good agreement with experimental results. Later, they mention that from measurements near the absolute zero a residual loss mechanism needs to be considered [36]. Gerthsen *et al.* [37] [37] , also using a model based on domain wall oscillation, derive dielectric and elastic losses and find a proportionality factor, which is essentially determined by materials properties like spontaneous striction, polarisation, elastic compliance and permittivity. Their calculations are also confirmed by experimental results and they conclude that dielectric and elastic losses are mainly caused by vibrating 90° domain walls.

More recently an experimental study of the crystallographic dependence of loss in lead titanate single crystals was reported [38]. They observe (001) oriented crystals having high acoustic losses and high electromechanical coupling factors k_{33}, whereas for the (111) orientation the opposite was observed. They explain this with the fact that the (111) oriented crystals are in a 'pseudomonodomain' state after poling, since the two domain states still present have an equivalent energy in the electric field (compare Figure 1.16). They state that the dielectric losses originate from 180° domain walls and mechanical losses from non-180° domain walls.

These calculations and experiments show that the domain wall vibrations are indeed a major contribution to materials constants and losses.

1.5 Thesis aims and approach

The aim of this thesis is to study high coupling materials in BAW resonators. For this purpose TFBAR structures are designed and fabricated using microfabrication techniques.

The main candidate to be studied is PZT. The behaviour of PZT thin films in BAW resonators is studied in terms fabrication technique (sol-gel and sputtering), film texture and film composition. The properties of the films are related to the characteristics of the resonators such as coupling constant and quality factor. The mechanisms leading to observed high losses in PZT are studied.

In the second part of the thesis alternative materials and methods are studied. The uniaxial ferroelectric potassium lithium niobate (KLN) films are fabricated by PLD as an alternative high coupling material. Its properties an applicability to BAW resonators are evaluated. The other alternative method is to use PZT thin films on a substrate inducing compressive stress in the PZT films. This allows for the fabrication of highly c-axis oriented films and thus for higher coupling. Devices on MgO substrates are fabricated and this technique evaluated.

1.6 Thesis outline

Apart from this introducing Chapter dedicated to the state of the art of PZT in BAW resonators and materials losses in PZT, this thesis has been structured as follows:

Chapter 2 describes the fabrication of PZT thin films by sol-gel and sputter techniques. Apart from standard characterisation techniques like X-ray diffraction and electron microscopy, the mechanical stresses of PZT thin films are studied as well, in order to evaluated possible process impacts on the final domain pattern. Furthermore, the dielectric properties at RF frequencies are of particular interest in this work. It is investigated whether the dielectric response decreases with frequency.

Chapter 3 focuses on thin film bulk acoustic resonator (TFBAR) devices based on the PZT described in Chapter two. The design and fabrication steps of the devices are illustrated and the parameters derived from impedance data of the devices are presented. The data were fitted using an equivalent circuit model and a model based on materials parameters. The comparison of materials parameters obtained from these data with values from direct measurements (Chapter 2) are included in this Chapter. Since an electric field was applied during the impedance measurements the field dependence of a TFBAR based on PZT could be studied and is also represented.

Chapter 4 describes two alternative approaches to finding a material with high coupling and low losses. One approach is a new material, potassium lithium niobate (KLN), which is a material with a high coupling and since it is an uniaxial ferroelectric the losses due to domain oscillations are thought to be lower. The fabrication of thin KLN films and first measurements of film properties are presented in the first part of this Chapter. The second part describes the fabrication of TFBARs based on PZT on single crystal MgO substrates. MgO allows for the preparation of highly c-axis oriented PZT thin films. These highly oriented films should result in devices with higher coupling.

Chapter 5 is the conclusion and outlook and will suggest some approaches to continue work in this field.

Chapter 2

PZT thin films: Synthesis and Properties

The properties of the piezoelectric material in a BAW resonator will determine the characteristics of the resulting device: the sound velocity and thickness of the material define the anti-resonance frequency, the coupling coefficient has a direct influence on the bandwidth of resulting filters and the dielectric constant defines the resonator area. PZT thin films offer a large scope of properties depending on composition and texture. In order to find suitable properties of PZT for BAW resonators and especially to increase understanding of PZT thin film behaviour in this application, films with either tetragonal or MPB composition and $\{100\}$ or (111) textures are studied. In practise, composition and orientation of PZT films are not the only variables that are important. The residual stress and microstructure (grain size, porosity, roughness) will also influence the materials properties of PZT thin films. These depend crucially on processing. As we will see, the two deposition methods used, sol-gel deposition and sputtering, result in different residual stresses and microstructures. Figure 2.1 gives an overview of the fabricated and characterised films. The characterisation of these films is performed regarding properties relevant for BAW resonator applications. The most important property is the coupling coefficient k_t^2. The coupling coefficient of the fundamental thickness mode k_t^2 of a piezoelectric plate (z direction perpendicular to the plane of the plate) can be expressed by material properties as defined in Chapter 1 (see Equation 1.9). By interferometric techniques [39] the so-called clamped piezoelectric coefficient can be measured:

$$d_{33,f} = \frac{e_{33}}{c_{33}^E} \tag{2.1}$$

This coefficient is the piezoelectric coefficient of the film perpendicular to the substrate surface according to the usual notations for thin film properties. From 1.9 and 2.1 the conclusions can be made that a high piezoelectric constant $d_{33,f}$ and low dielectric permittivity are needed in order to achieve a high coupling coefficient.

This Chapter will begin with introducing the applied deposition methods, centre on the specific conditions used in this work for the fabrication of PZT films with varying compositions and orientations. In the second part measurements of PZT thin film properties shall be presented, including the methods used and the results obtained for the in-plane stress measurements, dielectric as well as piezoelectric properties of the films. Some domain considerations are discussed, relating state of stress of tetragonal PZT films with their domain structures. The dielectric characterisation of the films includes measurements of field and frequency dependency of the dielectric constant. Measurements of dielectric and piezoelectric constants described in this Chapter will be compared to measurements derived from the impedance data of the devices in Chapter 3.

2.1 PZT deposition methods

2.1.1 Sol-gel deposition of PZT

Sol-gel processing is a wet-chemical technique for the fabrication of ceramics and an ideal method for making ceramic films since the colloidal suspension containing the materials to be deposited (sol) can easily be deposited in thin film form, by spinning, spraying or dipping [40]. The sol is prepared by dispersing metal or metalloid element surrounded by ligands in a solvent. The most widely used precursors are metal alkoxides because they react readily with water forming hydroxyl groups (hydrolysis):

$$M(OR)_4 + H_2O \rightarrow HO - M(OR)_3 + R - OH$$

Hydrolysed molecules can then link together in a condensation reaction, such as:

$$(OR)_3M - OH + OH - M(OR)_3 \rightarrow (OR)_3M - O - M(OR)_3 + H_2O$$

or

$$(OR)_3M - OR + OH - M(OR)_3 \rightarrow (OR)_3M - O - M(OR)_3 + ROH$$

This type of polymerisation reaction will continue and a gel will be formed. A schematic of the synthesis of thin ceramic films is shown in Figure 2.2. The precursor solution is

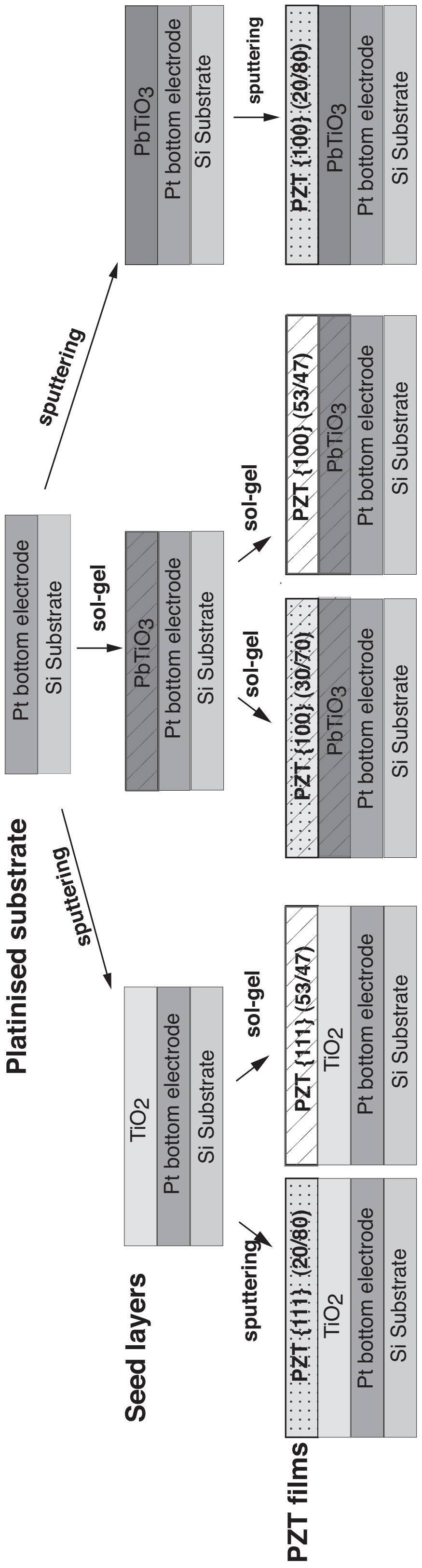

Figure 2.1: Overview of fabricated and characterised films, the hatched areas represent films prepared by sol-gel, non-hatched films are sputtered, dotted PZT films represent tetragonal composition, PZT films without dots have a composition at the morphotropic phase boundary.

deposited on the substrate in a first step. The polymerisation reaction will start during the deposition and intensify as the solvent evaporates. After deposition a pyrolysis will remove all the remaining solvent and organic components leaving an amorphous and porous inorganic metal oxide layer. Finally an annealing step will enable the sintering and crystallisation of the film.

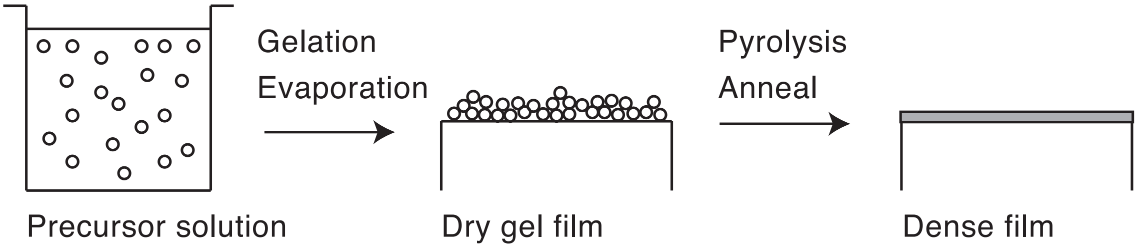

Figure 2.2: Principle of the sol-gel process.

In order to produce a multicomponent system like PZT multicomponent alkoxides can be used or soluble inorganic salts can be added. This method was used by Gurkovich [41] for the sol-gel deposition of $PbTiO_3$ and Budd [42] for $Pb(Zr, Ti)O_3$. Budd used a complex alkoxide made by reacting titanium isopropoxide and zirconium n-propoxide with an addition of lead acetate as precursors and 2-methoxyethanol as a solvent. The solutions used to make the sol-gel PZT films for this work are base on the route developed by Budd. In the following the details of the precursor solution preparation used shall be described.

Three different types of PZT films were prepared: A tetragonal $Pb(Zr_x,Ti_{1-x})O_3$ film with x = 0.3 and two films with a composition at the MPB (x = 0.53), one exhibiting a larger gradient in the Zr and Ti components and the other optimised to be gradient free [43]. Two solutions, one containing 10% lead excess, the other 30%, are needed for the preparation of each film of a certain composition to balance the lead loss during rapid thermal annealing (RTA). For the gradient free film four solutions with varying compositions are used, in this case three have a lead excess of 10% and one an excess of 30%. The necessary steps to prepare a precursor solution are shown in Figure 2.3. In a first step the lead-acetate trihydrate is dissolved in 2-methoxyethanol at 100°C / 500 mbar for 45 min. The water is then removed by distillation at 125°C / 300 mbar for 30 min. In the next step the dry powder is re-desolved in 2-methoxyethanol at 110°C / 500 mbar during 1 h. A solution containing tetraisopropylorthotitanate, zirconium n propoxide and 2-methoxyethanol is then added to the solution and refluxed for 3 h at 100°C / 500 mbar. A final distillation at 110°C / 300 mbar allows the adjustment of the concentration of the precursors to 0.45 M. To improve the behaviour of the sol-gel when drying 4% vol. of formamide is added to the solution(to reduce the hydrolysis rate [40]). The solution is then filtered using a 0.2 μm PTFE syringe filter and stored under dry argon.

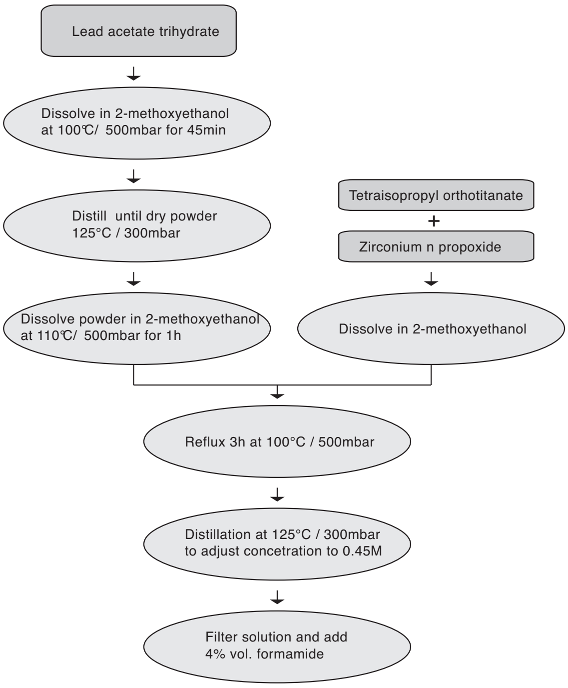

Figure 2.3: Schematic of the PZT solution precursor preparation.

Spin-coating was used to deposit the precursor solution on the platinised silicon wafers. This has the advantage of producing layers with a homogeneous thickness. The thickness depends on the rotation speed and the viscosity of the film. For a speed of 3000 rpm a monolayer thickness of about 60 nm is obtained with the 0.45 M solution described above. Thus 16 monolayers are needed to make a 1 μm thick PZT film. Since the film thickness has a great influence in the drying process, and thus shrinkage and cracking of the film, each monolayer is individually pyrolysed at 350°C.A schematic of the sol-gel deposition technique is shown in Figure 2.4. After four monolayers, the first three containing 10% lead excess and the fourth 30% lead excess, the film is crystallised at 650°C using rapid thermal annealing in an oxygen flow of 100 sccm. The ramp used depends on the desired orientation. The ramps used for (111) and {100} preferred orientations are shown in Figure 2.5. The seed layers needed to achieve a pure perovskite phase with the desired orientation shall be described in Section 2.2.

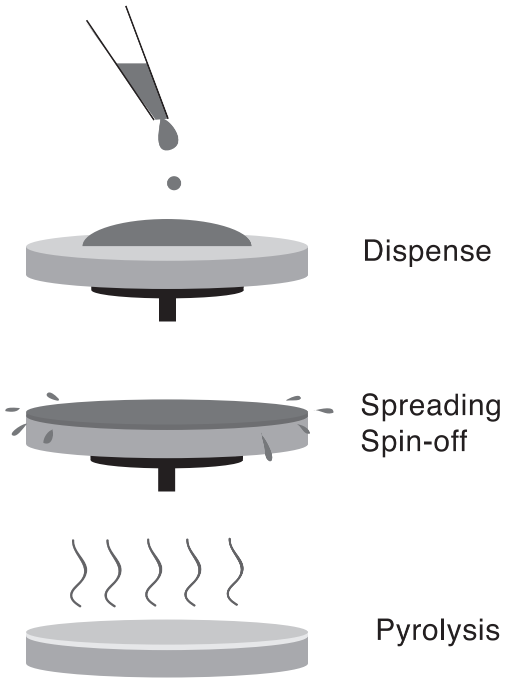

Figure 2.4: Schematic of the sol-gel deposition technique.

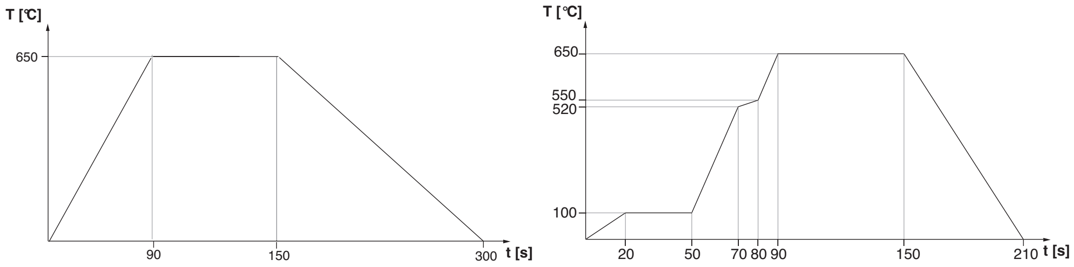

(a)

(b)

Figure 2.5: (a) Rapid thermal annealing ramp used to obtain (111) textured films. (b) Rapid thermal annealing ramp used to obtain {100} textured films.

2.1.2 Sputter deposition of PZT

Sputter deposition is a very common method used for depositing metallic and ceramic thin films. For fabricating ceramic thin films two general methods need to be distinguished; sputtering of ceramic targets using radio frequency (RF) power or reactive sputtering of metallic targets using RF, direct current (DC) or pulsed DC power. Multicomponent ceramics thus can be made either by sputtering the multicomponent ceramic or by reactively sputtering more than one metal at the same time. The latter can be done either by using an alloy target or by using multiple targets. Multiple targets systems have either a confocal or perpendicular sputtering geometries and have a rotating substrate stage to achieve homogeneity. The reactive gas, such as oxygen or nitrogen, will react with the metal atoms on the target and film surfaces. PZT thin films have been produced by all of these methods. The approach using ceramic PZT [44,45] or a pressed mixture of TiO_2, ZrO_2 and PbO [46] has some disadvantages. In order to crystallise the film during deposition, elevated temperatures are needed, which results in a loss of PbO. Thus an optimised excess of lead needs to be added to the target for a given temperature. Repeated use of the target will also change the stoichiometry of the surface, resulting in poor reproducibility of the films. Another disadvantage is that the power applicable to a ceramic target is limited which leads to low deposition rates. Many of these disadvantages can be avoided by using reactive sputtering in an oxygen or argon/oxygen atmosphere. The stoichiometry of the target stays constant, higher power can be applied on a metallic target resulting in a increased deposition rate. In the case of a multicomponent target [47,48] the flexibility of the system is still limited since the composition of the target will define the stoichiometry. However this arrangement has the highest deposition rate, because unlike the multitarget system it is static: in the case of perpendicular multitarget systems with the substrate rotating above or below the targets the deposition rate is decreased. Nevertheless this setup offers many advantages; since power can be applied to each target separately, the amount of lead flow can be adjusted for each deposition and the Zr/Ti ratio can be chosen simply by adjusting the power on the targets. The deposition rate per substrate can be compensated by coating several substrates at the same time.

For each of these methods, one needs to differentiate between ‘ex-situ’ methods and ‘in-situ’ methods. These terms refer to the crystallisation, which in the case of ‘ex-situ’ method does not take place during deposition, but in a second annealing step. That means an amorphous film is deposited, for instance by sputtering from a ceramic target, reactively sputtering or sol-gel deposition, and the film is then crystallised using rapid thermal annealing. The ‘in-situ’ method has only one step, the film is deposited at elevated temperatures so that the crystallisation can take place during the deposition.

The method used for the fabrication of sputtered thin films in this study was ‘in-situ’ reactive magnetron sputtering from multiple metallic targets. The system used is a Nordiko 2000 (Nordiko Ltd, Havants, Hants, UK) equipped with four targets and a rotating substrate holder (see Figure 2.6). The substrate holder can be heated using quartz lamps for ‘in-situ’ deposition and can either be rotated continuously or positioned directly over one target. The targets are equipped with magnetron sources, which increase the sputter efficiency by using a magnetic field to confine the plasma near the target. Two DC and one RF power sources can be used simultaneously. The flow of the sputter gases Ar, O_2 and N can be controlled using flow meters. This setup allows the co-sputtering of lead, titanium and zirconium targets in an O_2 atmosphere to create the corresponding oxides. The oxides synthesise and crystallise directly on the heated substrate rotating above the targets. The substrate is rotated at 6 rpm which corresponds to about one mono-layer per round. The general deposition parameters are shown in Table 2.1.

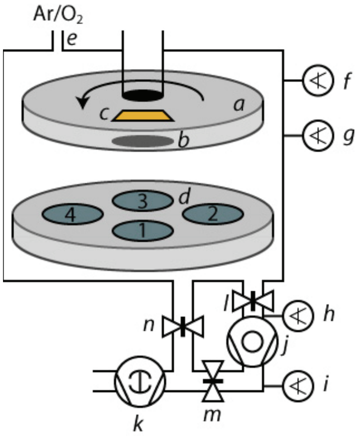

Figure 2.6: Configuration of the reactive magnetron sputtering tool Nordiko a) Rotating substrate holder, b) 4” substrate, c) heating lamps, d) target carousel, e) entry for process gases Ar and O_2, f) Baratron gauge used during process, g) Pirani gauge used during pumping, h) Pirani gauge, i) Penning gauge, j) turbo pump, k) primary pump, l) high-vacuum valve, m) foreline valve, n) roughing valve. The four power generators for targets (2 DC and 1 RF) and substrate bias (1 RF) are not shown on this scheme.

2.2 Growth issues

Epitaxial PZT films can be fabricated on single crystal substrates such as MgO, Al_2O_3 etc. For applications where microfabrication is needed, polycrystalline films on silicon substrates are more relevant. Some measures have to be taken in order to obtain single phase, well oriented PZT films on silicon wafers. The first requirement is an adequate bottom electrode, then using a seed layer ensures desired orientation. This section will describe the methods used to obtain single phase, highly textured PZT films and microstuctures and diffraction data shall be presented.

Table 2.1: General deposition parameters for sputtering of 20/80 PZT films

Preparation	
residual gas	8.10^{-6} mTorr (1 mPa)
substrate surface desorption	450°C / 10'+600°C / 10'
pre-sputtering	10' in O_2
Deposition parameters	
sputter gas pressure	16 mTorr (2.1 Pa)
gas	pure O_2
flow	20 sccm
rotation speed	6 rpm
temperature	700°C substrate holder centre
	570°C top surface of the substrate
Pb power	180 W Radio-Frequency (RF)
Zr power	76 W Direct Current (DC)
Ti power	400 W Direct Current (DC)
Cooling conditions	
gas	O_2
pressure	80 mTorr (10.5 Pa)

2.2.1 Platinum bottom electrode

It was observed that the processing of the bottom electrode has a large influence over the quality and orientation of the PZT film. It was reported by Maeder *et al.* [49] that Pt alone does not prevent lead diffusion: according to this study, when using a platinum electrode with a titanium adhesion layer, oxygen diffuses down to the titanium, the titanium diffuses up via the platinum grain boundaries, which results in a platinum film with TiO_2 inclusions at the grain boundaries and porous TiO_2 instead of a dense adhesion layer. PbO diffuses easily through the resulting structure. For this reason a stable diffusion barrier is needed. The adhesion layer, the diffusion barrier layer and the deposition temperature need to be adjusted carefully. The platinum bottom electrodes in this study used a titanium adhesion layer with a thickness of 2 nm, a TiO_2 layer of 40 nm thickness as diffusion barrier layer and a platinum layer with a thickness of 100 nm or 150 nm. The films were sputter deposited with a nominal/real deposition temperature of either 455°C/300°C (Balzers BAS 450) or 500°C/400°C (Nordiko 2000) depending on the sputtering system used. Depositions in both systems resulted in highly (111) textured Pt films.

2.2.2 Orientation control for (111) preferred orientation

Since nucleation of PZT films is mainly dependent on the underlying substrate, the most straightforward way to influence the texture of the film is to adapt the interface. Muralt *et al.* [50] reported the use of a thin (1 to 5 nm) TiO_2 film to obtain (111) textured $PbTiO_3$ and PZT thin films. The same technique was used to achieve a preferred (111) orientation in this study. Both for sol-gel and for sputtered PZT thin films a 2 nm thick sputtered TiO_2 film was used as a seed layer. The seed layer was deposited on the platinum bottom electrode in the Nordiko system at 570°C using reactive sputtering. The texture of the films were characterised using standard θ-2θ X-ray Diffraction (XRD). A Kristalloflex 805 (Siemens, Germany) diffractometer with CuKα radiation was used. In Figure 2.7 the XRD diffraction pattern of a 2 μm thick sol-gel film with a composition at the morphotropic phase boundary is shown. The film is a single phase perovskite, with a preferential (111) orientation. In Figure 2.8a the diffraction pattern of a tetragonal sputtered film is shown. The diffraction pattern of this sputtered $Pb(Zr_{0.20}, Ti_{0.80})O_3$ film (1 μm) has a close resemblance to the MPB film shown in Figure 2.7. It is also a single phase perovskite with a (111) texture. When looking at the diffraction pattern of the 20/80 PZT film on a logarithmic scale (see Figure 2.8b) a difference can be observed; the tetragonality of the 20/80 PZT film is revealed in the splitting of the {100} peak into (001) and (100) peaks. A texture index to quantify the preferential orientation of a film can be calculated by normalising the peak intensities with the corresponding peaks of randomly oriented powder according to the following equation [51] :

$$P(hkl) = \frac{\frac{I(hkl)}{I_0(hkl)}}{\frac{1}{N}\left(\sum_1^N \frac{I(hkl)}{I_0(hkl)}\right)} \tag{2.2}$$

Using this formula and the peak intensities from powder data [52] a preferred orientation of 97.5% for the sol-gel film shown in Figure 2.7 and 97.2% for the sputtered film shown in Figure 2.8a. These values vary slightly from one deposition to the other, but in general it can be said that the films are well oriented and no second phases are observed.

A scanning electron microscope (SEM, Zeiss LEO 1550) was used to observe the microstructure of the films. Figure 2.9 shows the cross-sections of a 2 μm thick sol-gel film with a 53/47 composition (Figure 2.9a) and of a 1 μm thick sputtered film with a 20/80 composition Figure (2.9b). The fact that the nucleation starts at the bottom electrode enables the growth of a columnar microstructure both for sol-gel and sputtered films. Both films show a dense, columnar microstructure. A relatively flat surface can be distinguished for the sol-gel film, whereas the sputtered film seems to have a higher roughness.

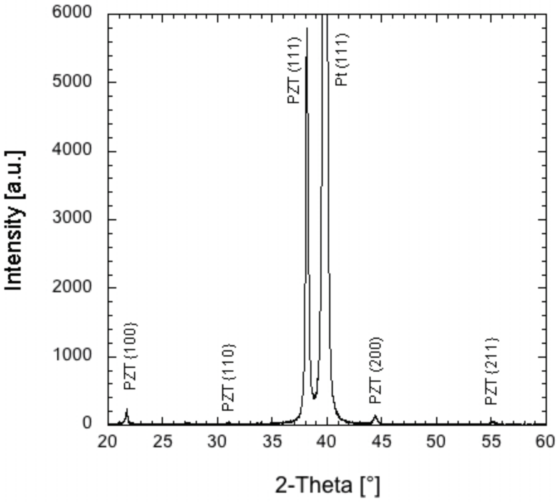

Figure 2.7: X-Ray diffraction pattern of a 2 μm thick Pb($Zr_{0.53}$, $Ti_{0.47}$)O_3 film deposited on a TiO_2 seed layer by sol-gel.

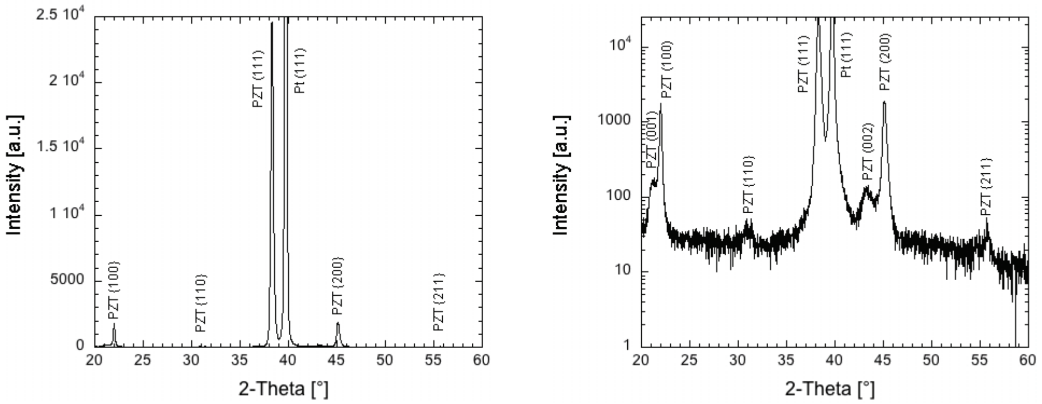

(a) (b)

Figure 2.8: (a) X-Ray diffraction pattern of a 1 μm thick Pb($Zr_{0.20}$, $Ti_{0.80}$)O_3 film deposited on a TiO_2 seed layer by sputtering. (b) the same pattern as in (a) using logarithmic scale for the intensity.

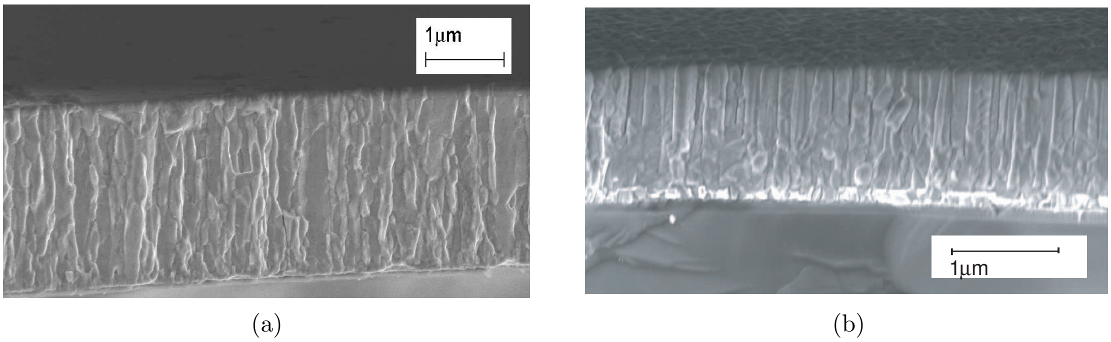

Figure 2.9: (a) SEM cross-section of a 2 μm thick sol-gel film with a 53/47 composition and a preferred (111) orientation. (b) A 1 μm thick sputtered film with a 20/80 composition and a preferred (111) orientation

2.2.3 Orientation control for {100} preferred orientation

Both for sol-gel and for sputtered PZT films a sputtered $PbTiO_3$ seed layer can be used to obtain a {100} orientation as reported previously by Ledermann [53] and Hiboux [54] respectively. In this work the $PbTiO_3$ seed layer for sol-gel films was produced by sol-gel techniques in the same way as the PZT films. The $PbTiO_3$ solution was fabricated using the same route as described in Section 2.1.1 for PZT, with 30% lead excess and a dilution in order to obtain a 20 nm thick film with one single spin. The rapid thermal anneal corresponds to the anneal for the {100} PZT film as shown in Figure 2.5b. Optimal conditions for sol-gel $PbTiO_3$ seed layer crystallisation were studied by Calame [55]. For the sputtered PZT films sputter deposited seed layers were used using a multitarget sputtering system (Nordiko 2000). The 3 nm thick $PbTiO_3$ layer was deposited as described in Section 2.1.2 with 150 W RF on the lead target and 450 W DC on the titanium target in an oxygen atmosphere. Three types of films were made with a {100} preferred orientation, two sol-gel deposited films, one gradient free with a 53/47 composition, the other standard with a 30/70 composition and one sputtered with a 20/80 composition. The XRD patterns of these films are shown in Figure 2.10 showing the 53/47 PZT film and Figure 2.11 showing the sol-gel and sputtered tetragonal films. The gradient free $Pb(Zr_{0.53}, Ti_{0.47})O_3$ film has a preferred {100} orientation and the {100} peak of the $PbTiO_3$ seed layer is also visible. No second phases were observed. When comparing the sol-gel and the sputtered tetragonal films a similar texture index is obtained, but a significant difference in the ratio of the (100) to (001) peak intensities is observed. This difference results from the deposition process and the stress it entails. The sputtered film has more domains with the c-axis perpendicular to the substrate. The a/c ratio of tetragonal films will be discussed in further detail in the next section. In Figure 2.12 the SEM cross-sections of a sol-gel deposited gradient free Pb($Zr_{0.57}$, $Ti_{0.43}$)O_3 and of a sputtered Pb($Zr_{0.20}$, $Ti_{0.80}$)O_3 film with thicknesses of 1 μm are shown. As for the (111) oriented films a columnar microstructure is observed in both cases and a higher roughness is apparent.

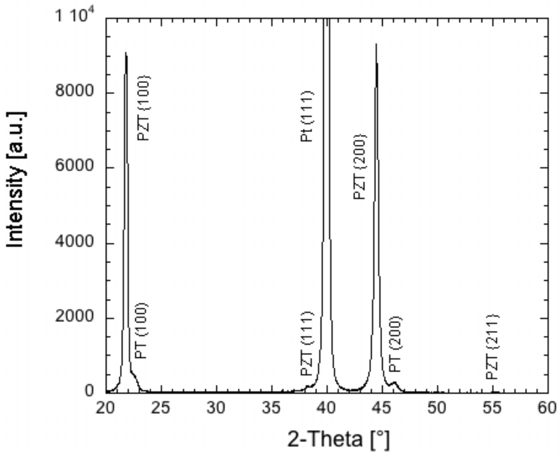

Figure 2.10: X-Ray diffraction pattern of a 1 μm thick gradient free Pb($Zr_{0.53}$, $Ti_{0.47}$)O_3 film deposited on a $PbTiO_3$ seed layer by sol-gel.

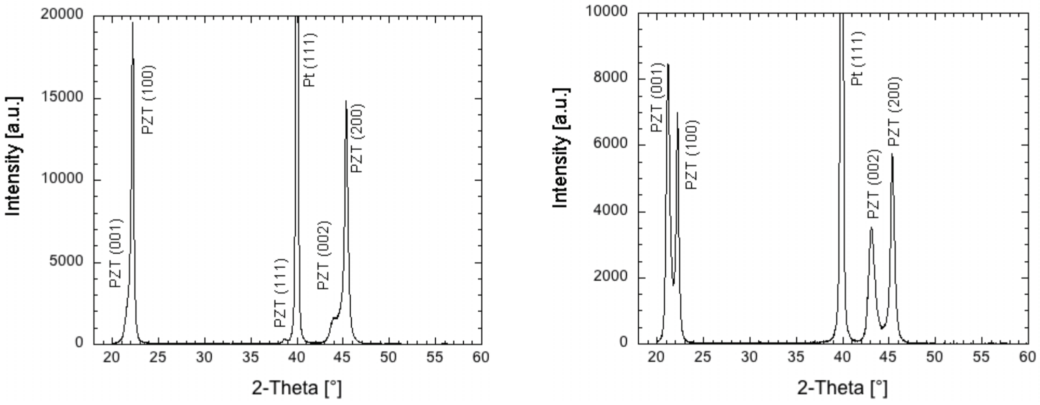

(a) (b)

Figure 2.11: (a) X-Ray diffraction pattern of a 1 μm thick Pb($Zr_{0.30}$, $Ti_{0.70}$)O_3 film deposited on a $PbTiO_3$ seed layer by sol-gel (b) X-Ray diffraction pattern of a 1 μm thick Pb($Zr_{0.20}$, $Ti_{0.80}$)O_3 film deposited on a $PbTiO_3$ seed layer by sputtering.

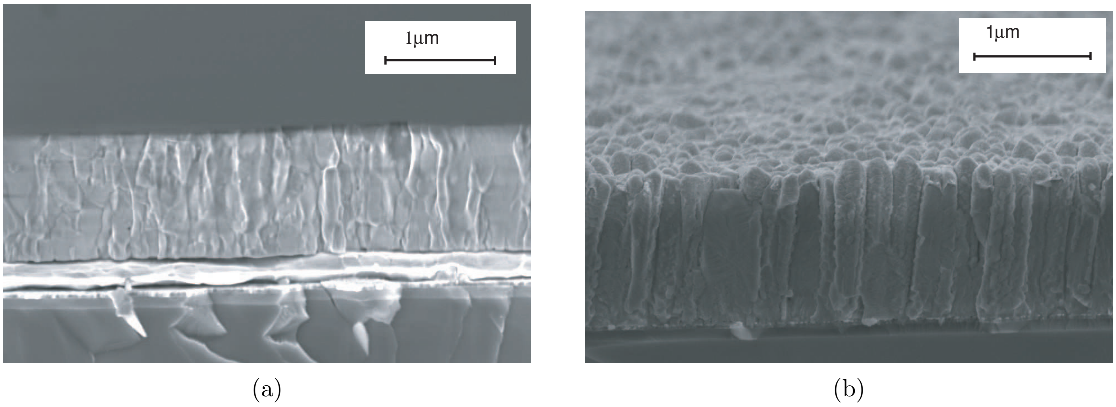

(a) (b)

Figure 2.12: (a) SEM cross-section of a 1 μm thick gradient free sol-gel film with a 53/47 composition and a preferred {100} orientation. (b) A 1 μm thick sputtered film with a 20/80 composition and a preferred {100} orientation.

2.3 Domain considerations in tetragonal PZT films

As was discussed in Section 1.4.2 the orientation of the domains depends on the crystalline orientation of the film. The orientation of these domains and the domain walls will affect the properties of the PZT films. In this section the domain configurations for (111) and {100} textured tetragonal PZT films shall be discussed. In the case of tetragonal {100} textured films the a/c domain ratio depends on the stress in the film. This stress is dependent on the thermal expansion mismatch of the substrate, but as will be seen the deposition method also plays an important role. For this reason the subsection concerning {100} textured tetragonal PZT films is divided into two parts, the first part describing sol-gel films, the second sputtered films.

2.3.1 (111) textured tetragonal PZT films

The vibration of domain walls in an alternating electric field is thought to be one of the main contributions to PZT materials losses. As discussed in Chapter 1 the ferroelastic domain walls (90°) are most relevant, since they can not be substantially removed by poling, as long as the film is clamped on the substrate. As shown in Figure 2.13 the 90° domain walls in a (111) textured tetragonal PZT are parallel to the electric field. This means that the two domain states left after poling have the equivalent energy in the electric field. This should mean that (111) textured tetragonal films have reduced losses due to domain vibration and thus are favourable to achieve higher values for the quality factor of the resonator. It has been shown for relaxor-PT single crystals that the Q-factors for (111) oriented crystals are higher than for (001) oriented crystals [38] as mentioned in Section 1.4.2.

The coupling factor of a resonator based on a (111) textured tetragonal film is expected to be lower than for a (001) oriented film, as its piezoelectric coefficient is lower. The domain structure after poling contains charged domain walls as shown in Figure 2.13. The negatively charged domain walls are probably compensated by oxygen vacancies.

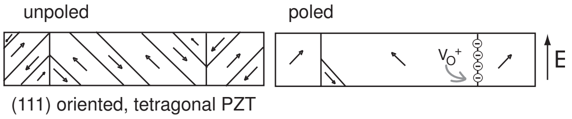

Figure 2.13: Domain structure of (111) oriented films before and after poling in the direction indicated.

2.3.2 {100} textured tetragonal PZT films

The $PbTiO_3$ seed layer favours growth of the {100} direction, which results in films containing domains with a mixture of (001), (100) and (010) orientations. An illustration of the cubic phase and the three possible tetragonal variants (a_1, a_2 and c) is shown in Figure 2.14. In the following discussion the coefficient $d_{33,f}$ will be referred to as d_{zz}, the piezoelectric coefficient perpendicular to the substrate surface (z-direction) in order to avoid confusion with the piezoelectric coefficients of the single crystal. Figure 2.15 illustrates piezoelectric coefficients d_{33} and d_{15}, the two coefficients which can be excited by an electric field E_3 perpendicular to the substrate surface. The (100) and (010) orientations have the tetragonal c-axis and thus also the polarisation in the plane of the substrate (see Figure 2.16). The resulting d_{zz}, value of these orientations is low, since d_{33} for these crystallites is zero. In order to obtain a high d_{zz} value a c-axis oriented, i.e. a (001) oriented film is needed, which enables the $S_3 = d_{33} \cdot E_3$ excitation, where S_3 is the strain in the (001) direction. As stated in Section 1.4.2 the {100} orientation results in higher losses due to the vibration of non-180° domain walls. These walls move in the electric field since two neighbouring domains do not have the same energy and one of the domain states is preferred depending on the orientation of the electric field. Losses will also be generated by the domains with their polarisation in plane since the energy invested in these domains is used to excite unwanted acoustic waves.

When cooling through the phase transition the a-domains will lead to in-plane expansion while the c-domains will lead to in-plane contraction (see Figure 2.17). According to the stresses in the film during phase transformation these three types of crystallites will develop a configuration in order to minimise the stress. The stress of a piezoelectric film is generally imposed by the underlying substrate, due to mismatch in the lattice parameters and different thermal expansion coefficients of the film and the substrate, since the film is clamped to the substrate. Roytburd *et al.* [56] observed the stress relaxation due to domain formation at the phase transition in 450 nm thick epitaxial $PbZr_{0.2}Ti_{0.8}O_3$ films deposited by PLD. They report the films completely relaxed their stress by assembling all three domain variants to create a three dimensional stress free domain structure as shown in Figure 2.18. Calculations of the thermodynamically stable domain configurations dependent on the thermal strain difference between the film and the substrate for epitaxial thin films, were performed by Pertsev *et al.* [57,58]. They show 'misfit strain - temperature' phase diagrams calculated for various compositions. These diagrams will be used to discuss the observed stress behaviour in {100} textured tetragonal films. Since the deposition method also plays a role in determining the residual stress in the films, the following paragraphs will introduce works published on sol-gel deposited and sputtered films and compare them with films studied in this thesis.

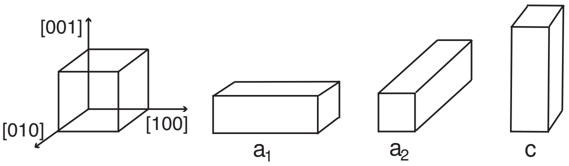

Figure 2.14: Cubic phase and the three tetragonal variants.

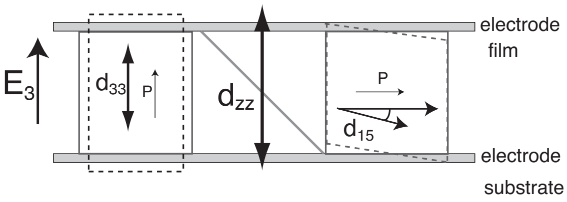

Figure 2.15: Illustration of the piezoelectric coefficients excited in {100} oriented tetragonal films. The piezoelectric constant d_{zz} of a clamped piezoelectric film corresponds to $d_{33,f}$.

Sol-gel films

The characterisation of residual stress in sol-gel derived PZT films has been subject of many studies and was first reported by Yi and Sayer [59]. The shrinkage of the film

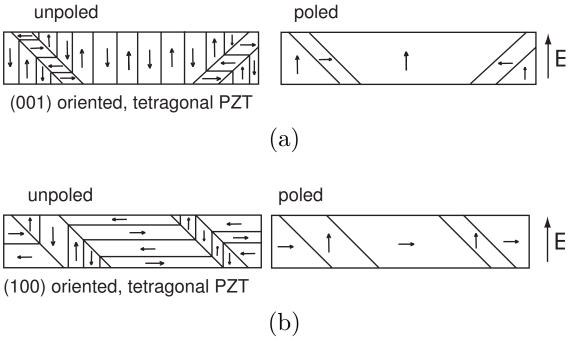

Figure 2.16: Domain structure of (a) (001) and (b) (100) oriented tetragonal films before and after poling in the direction indicated.

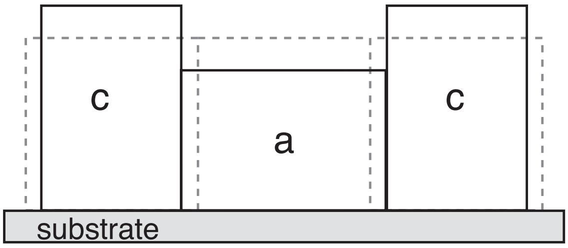

Figure 2.17: Cubic to tetragonal phase transition producing regions of different crystal orientation.

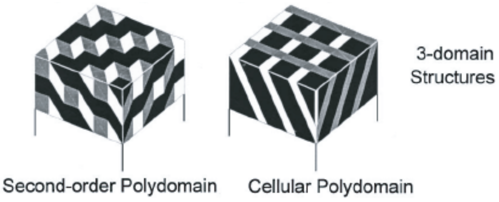

Figure 2.18: Polydomain configurations containing all three domain variants (From [56]).

due to solvent evaporation and firing during the sol-gel process leads to tensile stress. A systematic study of the evolution of stress during sol-gel processing was reported by Sengupta *et al.* [60]. They found a shrinkage of almost 40 % normal to the substrate during firing and significant changes in the stress state. They also state that the stress behaviour upon cooling is dominated by the thermal expansion mismatch between the coating and the substrate. They give the thermal expansion mismatch as a reason for the difference in stress for a single layer (200 MPa tensile stress) and a multilayer consisting of five layers (20 MPa compressive stress). Similar results have recently been reported by Corkovic *et al.* [61]. Tuttle *et al.* [62] used the thermal expansion mismatch as a tool to create layers with different states of stress. They used different substrates to induce either tensile or compressive strain in PZT thin films and found that the state of stress at the Curie point controls the domain configuration at room temperature. They observed compressive stress induced by the thermal expansion mismatch of the MgO substrate and the PZT caused preferential *c*-axis alignment upon cooling through the Curie point. In contrast the films on silicon substrates are under tension, and the crystallites are oriented with their polarisation vector parallel to the films surface. The consequences of these different domain configurations were also reported, an increase in polarisation and decrease in dielectric constant is shown for *c*-axis oriented films. Many experimental [63–67] and theoretical [68,69] studies have been performed observing the influence of applied external stress on the ferroelectric and piezoelectric film properties. These studies do not take the stress state at the Curie point into account, i.e. no annealing treatments are performed on externally stressed films. In the work of Lee *et al.* [70] an annealing treatment is used to induce a permanent compressive stress and improved ferroelectric properties were found. Spierings *et al.* reported the change in stress of a PZT layer from tensile to compressive when a top electrode was deposited and the sample annealed above the Curie temperature. Apart from Tuttle *et al.* [62] most of the above-mentioned studies do not analyse the domain configuration of {100} oriented films.

For a better understanding of the relations between stress and domain configurations of sol-gel deposited PZT films, $Pb(Zr_{0.3}Ti_{0.7})O_3$ on platinised silicon substrates were studied in this thesis. The influence of an annealing cycle in vacuum on the stress state of the film was analysed. The application of a mechanical constraint above Curie temperature was used to be able to change the stress variable for further insight into domain configuration versus temperature phenomena.

The platinised silicon wafer with a 1 μm thick $Pb(Zr_{0.3}Ti_{0.7})O_3$ deposited by sol-gel was diced into samples of dimensions 10 mm x 30 mm. Samples with three different thermal histories were compared: as deposited samples, samples annealed in vacuum and samples annealed in vacuum with additional externally applied stress. The vacuum anneal consisted in heating with a ramp of 36°C/min to 550°C, where the sample was kept for 15 min followed by a cooling ramp of 36°C/min. The vacuum anneal with externally applied stress is identical to the annealing cycle described above, the only difference is that the sample is mounted in a four-point bending apparatus. The four-point bending apparatus used to apply compressive stresses on the films is shown in Figure 2.19. This external stress was applied during the RTA treatment to be able to change the stress state above the Curie temperature. To calculate the compressive strain in the film Equation 2.3 was used. This equation gives the stress in the centre due to a known deflection at the loading points z_l for the given geometry (dimensions l and a see Figure 2.19a, $t_{substrate} = 380$ μm). Using the Young's modulus of the substrate, $E_{substrate} = 180.5$ GPa, this stress can then be transformed to film strain. In these experiments the maximum deflection at the loading points that could be applied before breaking of the sample was 0.75 mm, which results in a compressive strain of 0.2 %.

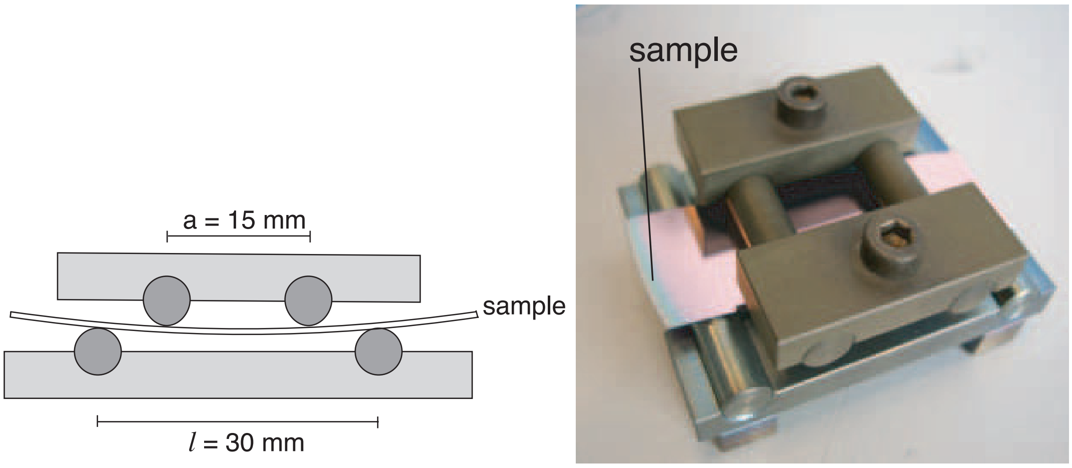

(a) (b)

Figure 2.19: (a) Schematic of a four-point bending apparatus (b) apparatus used in experiments with mounted sample.

$$\sigma = \frac{-3 \cdot z_l \cdot E_{substrate} \cdot t_{substrate}}{a \cdot (3l - 4a)} \tag{2.3}$$

Samples with and without anneal were analysed in terms of crystallographic structure and stress. The thin film stresses were measured by using a Tencor FLX 2900 stress analyser, which enables measurement of the stress during thermal cycling. A schematic of the working principle is shown in Figure 2.20. The radius of curvature of the sample is measured, as derived from the deflection angle θ of a laser beam reflected from the surface of the sample. A positive radius of curvature corresponds to tensile stress in the film and a negative curvature to compressive stress. In order to remove contributions to the stress of the underlying layers, the samples were measured first with the PZT film (radius of curvature r_2) and again after removal of the PZT by wet etching (radius of curvature r_1). With this method the changes in stress in the platinum film induced by the PZT layer are taken into account. The measurements are taken at periodic intervals during a thermal cycle. The thermal cycle used a heating/cooling rate of 3°C/min up to 550°C. The stress T can be calculated as a function of the Young's modulus of substrate, the Poisson coefficient of the substrate ν, the thickness of the substrate and of the film, t_{film}, and the radii of curvature without (r_1) and with (r_2) the PZT film according to the following equation (Stoney Equation [71]) :

$$T = \frac{E_{substrate} \cdot t_{substrate}^2}{6(1-\nu) \cdot t_{film}} \left(\frac{1}{r_2} - \frac{1}{r_1} \right) \tag{2.4}$$

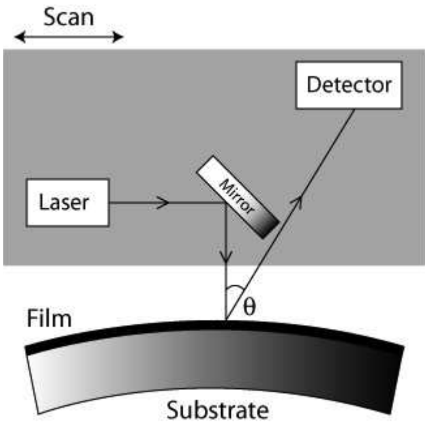

Figure 2.20: Schematic of the Tencor Flex 2900 stress gauge.

Negative values for T indicate compressive stress and positive values tensile stress. Figure 2.21 shows X-ray diffraction pattern of the $Pb(Zr_{0.3}Ti_{0.7})O_3$ film after deposition and the same film after the vacuum anneal described above. It can be seen that the (001) peak intensity is notably reduced. It is assumed that the tensile stress in the film at high temperatures forces the *c*-axes to lie in-plane. This configuration seems to be stabilised by oxygen vacancies, since the same anneal in oxygen leaves the domain configuration unchanged. The diffraction patterns showing the {200} peak of all three samples are displayed in Figure 2.22. The *c*-domain proportion is calculated using powder data file for 30/70 PZT [72]. Since (002) peak in the XRD pattern is wide, the areas underneath the (002) and the (200) peak were compared to get a more accurate value for the *c*-domain proportion. For the as deposited film the *c*-domain proportion was found to be around of 0.48. For the two annealed films very wide (002) peaks can be distinguished. Using the surfaces of these peaks *c*-domain proportions of 0.2 for the annealed film and 0.4 for the film annealed under compression are estimated.

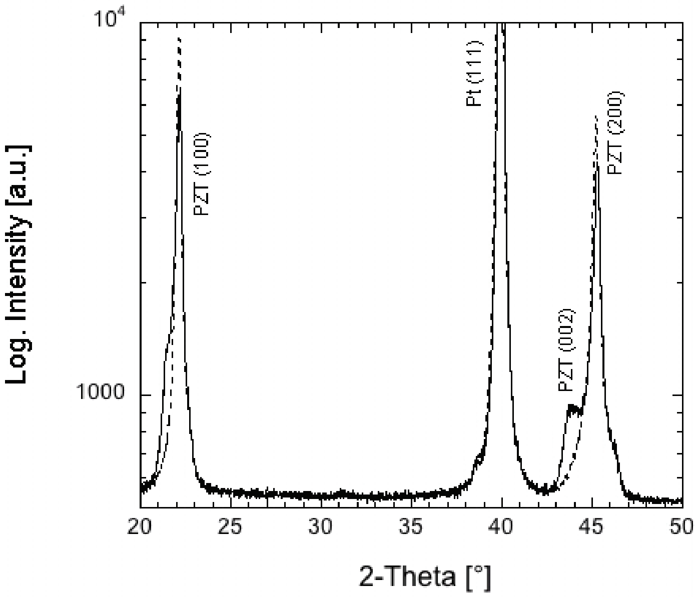

Figure 2.21: X-Ray diffraction pattern of a 1 μm thick sol-gel Pb(Zr$_{0.30}$, Ti$_{0.70}$)O$_3$ film after deposition (full line) and annealed in vacuum (dotted line).

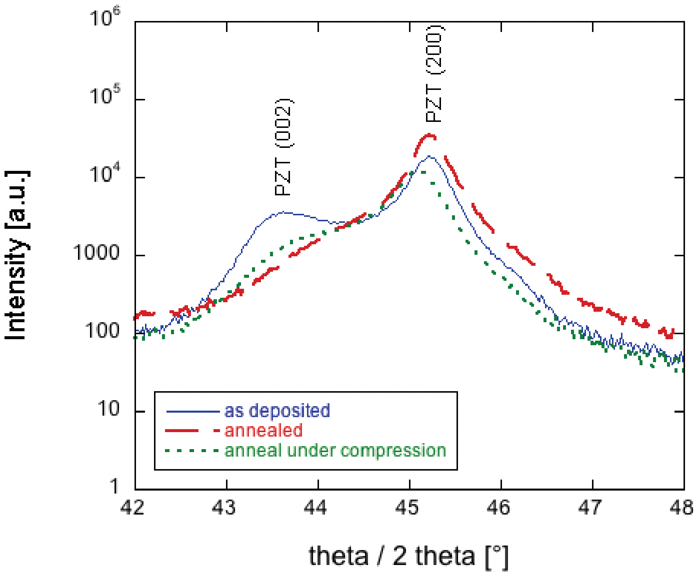

Figure 2.22: X-Ray diffraction pattern of the {200} peak of a 1 μm thick sol-gel Pb(Zr$_{0.30}$, Ti$_{0.70}$)O$_3$ film after deposition, annealed in vacuum and annealed in vacuum under compression.

The stress versus thermal history of these three sample types show clear differences as can be seen in Figure 2.23. It can be seen that the film without any annealing treatment (denominated as 'as deposited') is in a relaxed state at room temperature. The film is in a tensile state at the maximal annealing temperature of 550°C due to the deposition method and becomes more tensile when cooling down, until it reaches the Curie temperature θ_C at approximately 480°C. This is due to the thermal expansion coefficient of the cubic PZT being bigger than the thermal expansion coefficient of silicon. Beneath θ_C the thermal expansion coefficient of the PZT film is smaller than for silicon creating compressive stresses upon cooling. The thermal expansion coefficient of the PZT beneath θ_C depends on the ratio of c/a domains, since the thermal expansion coefficients of the ferroelectric phase are strongly asymmetric, with a negative and positive thermal expansion coefficient for the c-axis and the a-axis, respectively. In the case of the as deposited film the observed thermal expansion coefficient smaller than for silicon indicates a strong contribution of the negative coefficient in c-direction. This means many domains with their c-axis lying in plane are present.

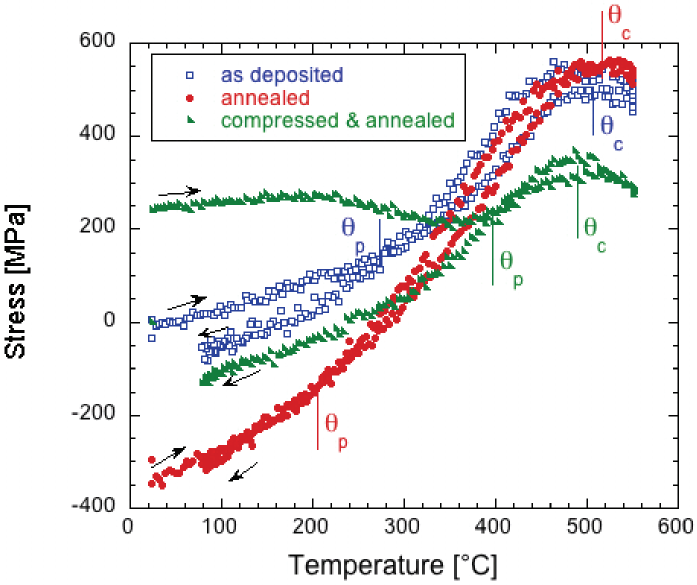

Figure 2.23: Stress measurements of a 1 μm thick sol-gel Pb($Zr_{0.30}$, $Ti_{0.70}$)O_3 film as deposited, annealed and annealed under compression. θ_C and θ_P indicate Curie and domain pattern transition temperatures, respectively.

Cook *et al.* [73] measured the thermal expansion coefficients of bulk polycrystalline Pb($Zr_{0.52}Ti_{0.48}$)O_3 doped with 1% Nb_2O_5 parallel and perpendicular to the polarisation axis. Spierings *et. al* [74] used this data to calculate thermal stress curves for thin films with the polar axis parallel and perpendicular to the film surface (see Figure 2.24). When comparing with the data presented in Figure 2.24 the shape of the stress curve of the as deposited film is similar to with the curve with the polarisation parallel to the surface, confirming the presence of many *a* oriented domains.

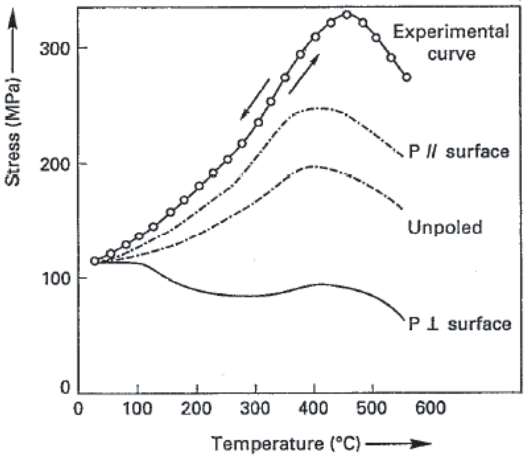

Figure 2.24: Stress in a 220 nm thick sol-gel film compared with data measured on poled and unpoled polycrystalline PZT (from Spierings *et al.* [74])

The stress curves of the two annealed films mainly differ in the slope beneath θ_C. The film annealed in vacuum has a bigger slope, i.e. the thermal expansion coefficient is even smaller than for the as deposited film, indicating more domains with their *c*-axis in plane are present. The heating and cooling curves follow the same stress-temperature dependence, showing that this process is reversible. For the film annealed under externally applied stress a thermal expansion coefficient close to that of silicon is observed up to around 240°C, indicating that the film has more *c*-axis orientation. However upon heating these domains return to a configuration similar to the as deposited film. These measurements show that applying compressive stress and heating above θ_C helps to obtain *c*-axis orientation, however the domain configuration is not stable and is changed by subsequent heating. In contrast the anneal in vacuum creates a very stable domain state with a large proportion of *a*-domains.

In the stress-temperature curves of all three samples the slopes are not constant, a kink is observed at different temperatures depending on the sample. These kinks can be interpreted by looking at the 'misfit-strain - temperature' phase diagram introduced by Pertsev *et al.* [57, 58]. The phase diagram for a $PbZr_{0.3}Ti_{0.7}O_3$ film is shown in Figure 2.30. The change in thermal expansion coefficient takes place when the $a1/a2/a1/a2$ configuration transforms to the $c/a/c/a$ configuration at the phase transition temperature θ_P. The stress curves can be modelled by taking this phase transition into account. The total in-plane stress in the film is induced by the strain due to the process, $S_{process}$, the thermally induced strain, which includes the stress due to mismatch of thermal expansion coefficients of the substrate, α_{Si}, and the cubic film, α_{PZT}, minus the temperature dependent term of strain due to domain configuration, $S_{spontaneous}$, as shown in Equation 2.5. This term is dependent on the a/c domain configuration below θ_P and on the a/a domain configuration above θ_P.

$$T_{film} = \frac{1}{s_{11} + s_{12}} \cdot (S_{process} + (\alpha_{Si} - \alpha_{PZT})(\theta - \theta_0) - S_{spontaneous}) \tag{2.5}$$

The temperature dependence of the domain contribution can be included by using the lattice constants as a function of temperature as reported by Haun *et al.* [75]. This data for a PZT film with a 32/68 composition is shown in Figure 2.25. For a tetragonal {100} oriented film the spontaneous strain below θ_P in the film plane is given by Equation 2.7 (Derived from Ref. [57]), where ϕ is the proportion of *c*-domains. Using Equation 2.5 and the lattice constants from Figure 2.25 a value for ϕ can be estimated. The values used to model the heating data up to θ_P are shown in Table 2.2. The *c*-domain proportion of 0.40 for the as deposited film is close to the value of 0.48 calculated from the XRD data shown in Figure 2.22. The XRD measurements also confirm the decrease of *c*-domain proportion when annealing in vacuum. However the increase of *c*-domains when applying external stress to the film was not observed using XRD.

$$\begin{aligned} S_{spontaneous} &= (1 - \phi) \cdot (S_a + S_c) + \phi \cdot S_a \\ S_a &= \frac{a(\theta) - a_0}{a_0} \\ S_c &= \frac{c(\theta) - a_0}{a_0} \end{aligned} \tag{2.6}$$

Above θ_P the film is in a $a_1/a_2/a_1/a_2$ domain configuration. The spontaneous strain due to the domain configuration is given by Equation 2.7, where ψ is the proportion of a_1-domains. Using Equation 2.5 with $S_{spontaneous}$ for the $a_1/a_2/a_1/a_2$ domain configuration the stress curves can be fitted above θ_P. As a variable fitting parameter the proportion of a_1-domains, ψ, was used. Since one would assume the a_1/a_2 to be 1:1 fitting was also performed by using compliance constants $s_{11} + s_{12}$ as the variable fitting parameter. The sum of $s_{11} + s_{12}$ becomes nearly three times higher than the theoretical value, which could be due to the mobility of domain walls at high temperatures.

Parameters used for these fits are shown in Table 2.2.

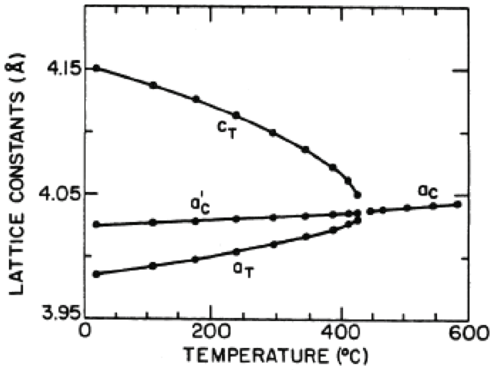

Figure 2.25: Lattice constants of PZT 32/68 versus temperature, from [75].

$$S_{spontaneous} = (1 - \psi) \cdot S_a + \psi \cdot S_c \tag{2.7}$$

common parameters			
α_{Si} $[10^{-6} \cdot \mathrm{C}^{-1}]$	3.9 [76]		
α_{PZT} $[10^{-6} \cdot \mathrm{C}^{-1}]$	6.6 [75]		
θ_0 [C]	550		
s_{11} $[10^{-12} \cdot \mathrm{Pa}^{-1}]$	8.4 [57]		
s_{12} $[10^{-12} \cdot \mathrm{Pa}^{-1}]$	-2.7 [57]		
a_0 [Å]	4.037 [75]		
	as deposited film	**annealed film**	**annealed & compressed film**
$S_{process}$ $[10^{-3}]$	2.16	2.28	1.42
θ_P [C]	300	200	380
θ_C [C]	500	510	480
ϕ	0.40	0.30	0.48
ψ	0.55	0.51	0.61
$s_{11} + s_{12}$ $[10^{-12}\ \mathrm{Pa}^{-1}]$	11	6.5	14

Table 2.2: Properties used for fitting the stress vs. temperature behaviour of 1 μm thick sol-gel deposited 30/70 PZT films. The data were fitted using Eq. 2.5 with the spontaneous strain described by Eq. 2.7 below θ_P and Eq. 2.7 above θ_P .

The stress curve of the as deposited film with the simulated curves below and above θ_P

are shown in Figure 2.26. The fits for the annealed films can be found in the Appendix C.

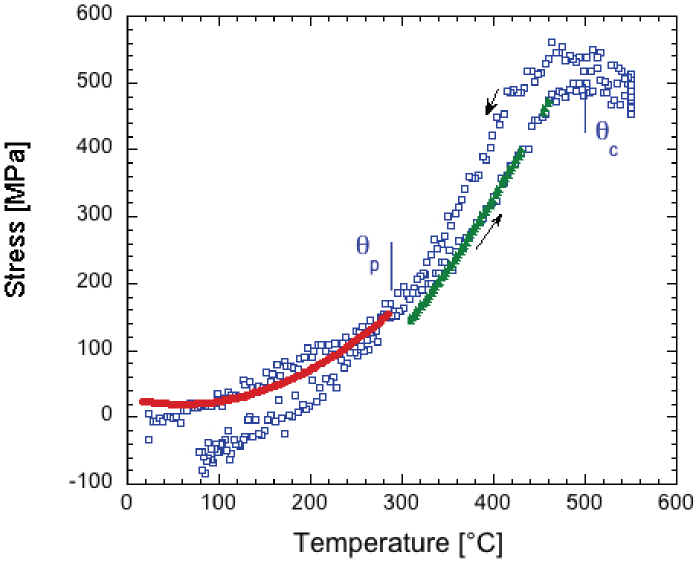

Figure 2.26: Stress vs. temperature curve for the 1 μm thick sol-gel 30/70 PZT film 'as deposited'. The simulated data shown was found using Eq. 2.5 with the spontaneous strain described by Eq. 2.7 below θ_P and Eq. 2.7 above θ_P.

The value for misfit-strain $S_m$in the works of Pertsev *et al.* [57, 58] is defined as:

$$S_m = \frac{b^*(\theta) - a_0(\theta)}{a_0(\theta)} \tag{2.8}$$

where, b^* is the substrate effective lattice parameter and a_0 is the cubic lattice constant of the free standing film. To compare the stress data with the 'misfit-strain - temperature' phase diagram [57, 58] the data needs to be converted to strain, which can be done by approximating the Young's modulus to be constant. Then the spontaneous strain term needs to be subtracted, since the the 'misfit-strain' axis in the phase diagram does not include the strain due to domain configurations. One obtains the temperature dependence of strain as:

$$S_m = S_{process} + (\alpha_{Si} - \alpha_{PZT})(\theta - \theta_0) \tag{2.9}$$

The term named $S_{process}$ includes residual strain from the deposition method, strain due to defects such as oxygen vacancies and strain due to applied external stress. Using Equation 2.9 with the values for $S_{process}$ obtained from fitting the stress curves the temperature dependencies of strain for the three samples can be plotted in the 'misfit-strain -

temperature' phase diagram as shown in Figure 2.27b. The configuration transformation $a_1/a_2/a_1/a_2$ to $c/a/c/a$ observed in the stress curves is not confirmed when plotting in the misfit strain diagram as shown in Figure 2.27b. Since the theory is based on epitaxial films, grain boundaries could play a role. Another explanation would be deviations of the film composition, which would also lead to differences when comparing to the 'misfit-strain - temperature' phase diagram for 30/70 films. The film annealed in vacuum has a larger S_m than the as deposited film. Oxygen vacancies would lead to an increase of the lattice constants, and thus to compression, meaning a lower S_m. It is possible that the annealing temperature is of 550°C is too close to θ_C. The tensile stress in the film leads to an $a_1/a_2/a_1/a_2$ pattern to relax the stress during the anneal. The oxygen vacancies formed during an anneal must play a role in stabilising this domain pattern, since when the same anneal is performed in oxygen, the domain pattern does not change. For the film annealed with externally applied stress the S_m also includes contribution of the compressive external stress, lowering the value for S_m and thus increasing the proportion of c-domains.

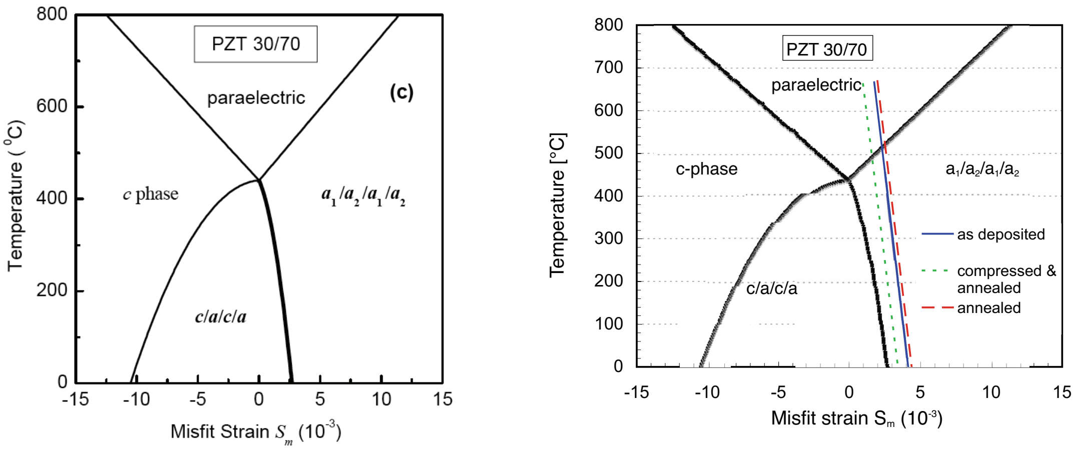

(a) (b)

Figure 2.27: (a) Calculated 'misfit strain - temperature' phase diagrams for PZT 30/70 (From [57])(b) Phase diagrams as in (a) including data derived from stress measurements of 30/70 sol-gel PZT films shown in Figure 2.23.

Sputtered films

A detailed stress analysis of sputtered PZT films can be found in the work of Bruchhaus *et al.* [77]. They use the stress temperature curves to extract the lattice parameters of

PZT films with 10/90 and 48/52 compositions. They found that the tetragonal film was in a compressed state whereas the MPB film was in a tensile state after deposition. These films were prepared by multi-target sputtering and had a preferential (111) orientation.

The sputtered Pb($Zr_{0.20}$, $Ti_{0.80}$)O_3 film with a {100} texture as presented in Section 2.2.3 (XRD pattern is shown in Figure 2.11) was not easily reproduced. Although the deposition parameters were not changed, the c/a ratio could not easily be controlled. The substrate and the deposition of the bottom electrode will play a great role in determining the c/a ratio, but even when keeping substrate and Pt deposition parameters constant, the same c/a ratio varied significantly. For this reason this film could be studied on platinised substrate, but not as a device structure for high frequency measurements.

The platinised silicon wafer with a sputtered Pb($Zr_{0.20}$, $Ti_{0.80}$)O_3 film was cut into samples with the dimensions of 30 mm x 10 mm. The annealing cycles were performed as described above for the sol-gel samples. Three sample types were obtained: the as deposited sample, the sample annealed in vacuum to 550°C, and the sample using the same annealing cycle in addition to an externally applied compressive force.

The diffraction patterns showing the {200} peak of these three samples are displayed in Figure 2.28. The c-domain proportion is calculated for all three samples using the powder diffraction data for 20/80 PZT [78]. Using the surfaces of the (002) and the (200) peaks the c-domain proportions are 0.6 for the as deposited film, 0.5 for vacuum annealed film and 0.6 for the film annealed under compression.

The stress versus temperature curves for the three samples are shown in Figure 2.29. As for the sol-gel film, the as deposited film is relaxed at room temperature. At the maximal annealing temperature of 550°C the films are highly compressive in contrast to the sol-gel films. The films become increasingly tensile upon cooling, indicating the thermal expansion coefficient of the PZT is bigger than the thermal expansion coefficient of silicon. This means that the negative thermal expansion of the c-axis does not play a big role and thus the film has a high degree of c-axis orientation. The sample annealed while being subjected to externally applied stress was found to be in a state of large tensile stress which was reduced after the thermal cycle to values similar to the vacuum annealed sample. As for the sol-gel, film the domain configuration induced by the externally applied stress was not reversible and a kink is observed in all the curves. This kink is at around 450°C for all three samples. A second change in slope is visible at around 520°C, which is thought to correspond to θ_C. The 'misfit-strain - temperature' phase diagram for a $PbZr_{0.2}Ti_{0.8}O_3$ film is shown in Figure 2.30a [58]. The stress curves were modelled using the lattice constants as a function of temperature for 15/85 PZT reported by Kohli [79]. The fitted curves can be found in the Appendix C. The values used for these fits are

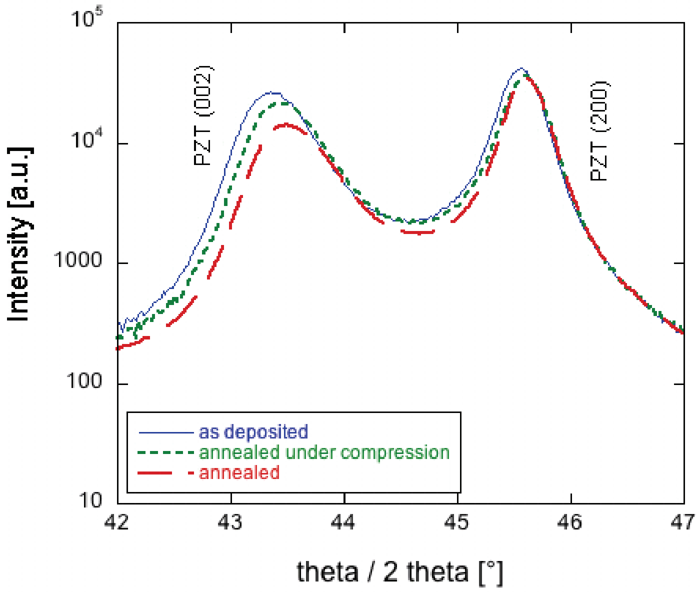

Figure 2.28: X-Ray diffraction pattern of the {200} peak of a 1 μm thick sputtered Pb(Zr$_{0.20}$, Ti$_{0.80}$)O$_3$ film after deposition, annealed in vacuum and annealed in vacuum under compression.

shown in Table 2.3. The film annealed under compression was found to have slightly more c-domains. As for the sol-gel films this was not observed using XRD, where the proportion of c-domains was comparable to the as deposited film. The decrease of c-domains for the vacuum annealed film observed by XRD was not confirmed using stress measurements, where this film is similar to the as deposited film.

Using Equation 2.9 with the values for $S_{process}$ obtained from fitting the stress curves the temperature dependencies of strain for the three samples can be plotted in the 'misfit-strain - temperature' phase diagram as shown in Figure 2.30b. The values for θ_P and θ_C correspond well to the kinks observed in the stress curves. Since the curves are close it is difficult to make any conclusions on the influence of the annealing treatment. It seems that for this sputtered film the influence of the annealing treatment is small, which confirms the XRD measurements.

2.4 Dielectric characterisation

The effective dielectric constant $\varepsilon_{33,f}$ and the loss factor $\tan\delta$ were determined from capacitance measurements using an impedance analyser (Hewlett-Packard, HP-4194) or an LCR bridge with the same experimental conditions as for the measurements of the piezoelectric

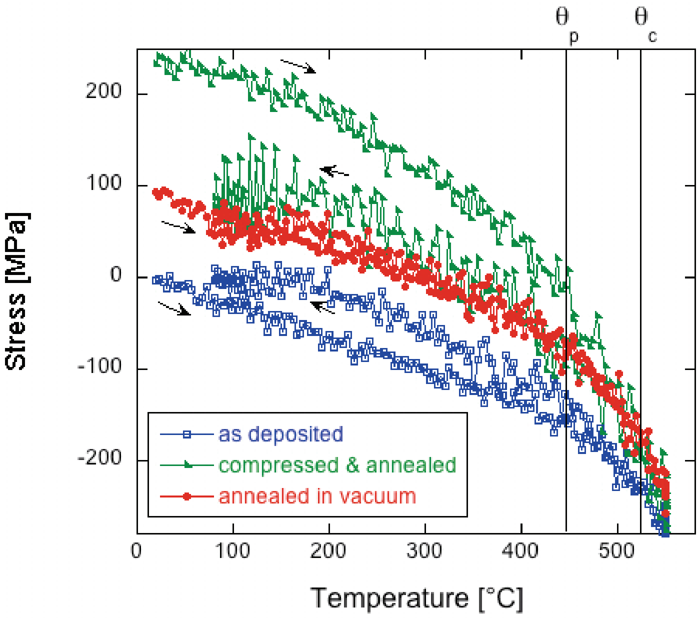

Figure 2.29: Stress measurements of a 1 μm thick sputtered $Pb(Zr_{0.20}, Ti_{0.80})O_3$ film, as deposited, annealed and annealed under compression.

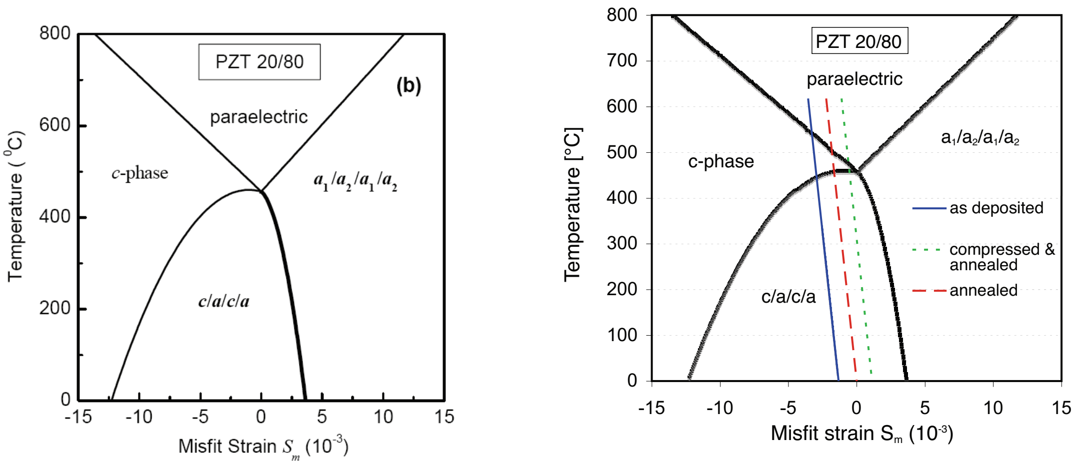

(a) (b)

Figure 2.30: (a) Calculated 'misfit strain - temperature' phase diagrams for PZT 20/80 (From [57])(b) Phase diagrams as in (a) including data derived from stress measurements of 20/80 sputtered PZT films shown in Figure 2.29.

common parameters			
α_{Si} [$10^{-6}\cdot$ C^{-1}]	3.9 [76]		
α_{PZT} [$10^{-6}\cdot C^{-1}$]	6.6 [75]		
θ_0 [C]	550		
θ_C [C]	520		
s_{11} [$10^{-12}\cdot Pa^{-1}$]	8.2 [57]		
s_{12} [$10^{-12}\cdot Pa^{-1}$]	-2.6 [57]		
a_0 [Å]	4.00 [79]		
	as deposited film	**annealed film**	**annealed & compressed film**
$S_{process}$ [10^{-3}]	-1.68	-1.12	-1.23
θ_P [C]	450	450	450
ϕ	0.54	0.50	0.56

Table 2.3: Properties used for fitting the stress vs. temperature behaviour of 1 μm thick sputtered Pb($Zr_{0.20}$, $Ti_{0.80}$)O_3 films. The data were fitted from room temperature to the phase transition temperature θ_P using Eq. 2.5.

coefficient d_{33} as described in the Chapter piezoelectric characterisation. The thin film PZT samples were prepared for these measurements by wet etching of the PZT to obtain access to the platinum bottom electrode and evaporating Cr(10 nm)/Au(100 nm) circular top electrodes with a diameter of 550 μm using a hard mask (Evaporator Edwards). The high frequency behaviour of the films was measured using an HP 8722D network analyser (Agilent Technologies, Palo Alto, CA) on the device structure, using an unreleased resonator structure with a capacitance area of two times 60 x 60 μm in series. In this section the dielectric constant of the films will be analysed as a function of the electric field and of frequency.

2.4.1 Field dependence of the dielectric constant

The capacitance versus voltage $C(V)$ measurements were performed (AC bias 0.1 V, 5 kHz) on all different film types. In order to compare the results, the samples were grouped in either compositions at the morphotropic phase boundary or tetragonal compositions. In this way the influence of the film texture can be estimated. Theoretical predictions of the dielectric constant near the MPB as a function of film orientation were reported by Du *et al.* [80,81] and are shown in Figure 2.31. For tetragonal compositions the dielectric constant is found to be much higher along the (111) direction than along the (001) direction.

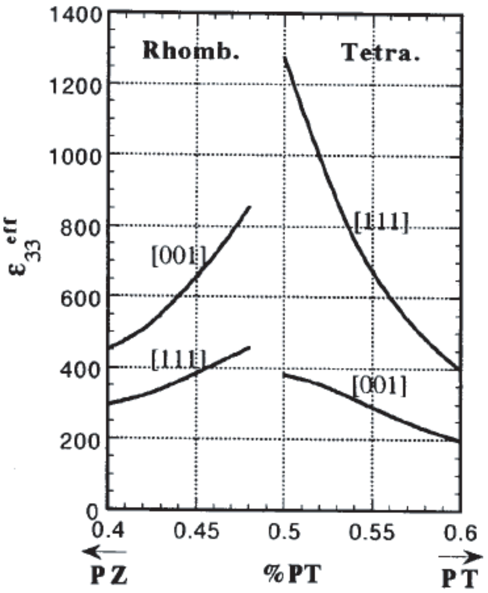

Figure 2.31: Theoretical predictions for the dielectric constants of PZT depending on the films orientation for PZT compositions around the morphotropic phase boundary (from Du [80]).

The dielectric constant and loss factor $\tan\delta$ for the two films with a 53/47 composition are shown in Figure 2.32. Both films were prepared by sol-gel, the (111) textured film has a thickness of 2 μm and the {100} textured film a thickness of 1 μm and was fabricated using the method for making gradient free films. The values of dielectric constant at zero field for these two films do not correspond to what is expected from theory (see Figure 2.31). There are several reasons which could explain this. Since the film thicknesses and the exact deposition conditions of these two films differ, the microstructure (grain size, domain configuration) and stress state will vary. The contribution of domain walls [82] and influence of stress [83] to the dielectric constant have been experimentally observed. The variation of the dielectric constant with the electric field shows the influence of the domain walls on the dielectric constant, the initial rise indicates some domain walls which were pinned are now able to move. With increasing field the domain wall contributions start to freeze out and the number of domains is reduced. Both these effects decrease the dielectric constant.

The dielectric constant and loss factor are shown for the tetragonal films in Figure 2.33. In this graph two of the measurements are of sputtered $Pb(Zr_{0.20}, Ti_{0.80})O_3$ films with 1 μm thickness and a preferential orientation of either (111) or {100}. The third measurement depicted in Figure 2.33 was performed on a 1 μm thick $Pb(Zr_{0.30}, Ti_{0.70})O_3$ film prepared by

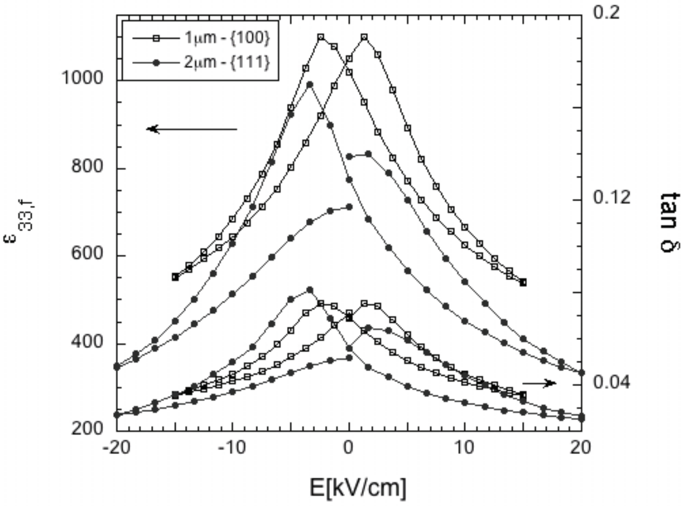

Figure 2.32: Dielectric constant vs. electric field for Pb($Zr_{0.53}$, $Ti_{0.47}$)O_3 films with either a (111) or a {100} preferred orientation. The (111) textured film has a thickness of 2 μm, whereas the {100} textured film has a thickness of 1 μm and was produced by the gradient free sol-gel route. The corresponding losses (tan δ) are shown.

the sol-gel method. The two sputtered films with a 20/80 composition were both fabricated in similar conditions with the only difference of having either a TiO_2 or a $PbTiO_3$ seed layer. Here the higher dielectric coefficient for a (111) textured film compared to the {100} textured film seems to correspond to the theoretical predictions. But since the theoretical predictions only discuss compositions up to 40/60 the values cannot be fairly compared. Little data is available for the orientation dependence of the dielectric constants for thin films with compositions away from the morphotropic phase boundary. Hiboux [84] who also studied PZT films with tetragonal compositions found dielectric constants of around 300 for {100} textured films and around 200 for (111) textured films (thickness 300 nm). The difference may again be caused by different stress states of the films, since the films have different thicknesses and also different ratios of a/c domains. The data for the sol-gel film with a 30/70 composition also shown in Figure 2.33 has a comparable dielectric constant to the sputtered film of the same composition studied by Hiboux [54] (around 550 at zero field).

When comparing the dielectric field dependence of the films with a composition at the MPB (Figure 2.32) with the tetragonal films (Figure 2.33) a difference in the slope of the curves is observed. The steep slope for films at the MPB shows the domain walls can move more easily than the domain walls in the tetragonal films, where the slope is flatter.

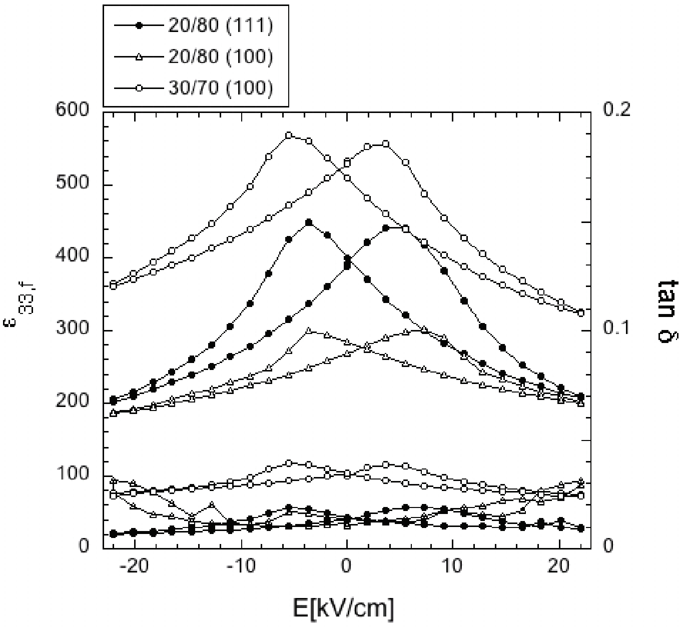

Figure 2.33: Dielectric constant vs. electric field of a {100} textured, 1 μm thick Pb(Zr$_{0.30}$, Ti$_{0.70}$)O$_3$ film deposited by sol-gel and two 1 μm thick Pb(Zr$_{0.20}$, Ti$_{0.80}$)O$_3$ films deposited by sputtering with either a {100} or a (111) preferred orientation. The corresponding losses (tan δ) are shown.

2.4.2 Frequency dependence of the dielectric constant

The dielectric constant as a function of frequency was studied on the device wafers using an HP 8722D network analyser (Agilent Technologies, Palo Alto, CA). The S_{11} scattering parameters obtained from these measurements were used to calculate the electrical admittance Y. The structures used to measure the dielectric constant were the same as the structures used to measure the resonance (see Chapter 3.) except that the membrane was not released. The resulting structure is a double capacitor in series, the data displayed here were measured on capacitors with an area of 60 x 60 μm. The sputtered Pb(Zr$_{0.20}$, Ti$_{0.80}$)O$_3$ film was not evaluated by this method since it could not be produced on a device wafer as explained above. The admittance data was fitted using an equivalent circuit as shown in Figure 2.34 and is given by Equation 2.11 .

$$Y = \frac{1}{R - \frac{i}{\omega C_{tot}}(1 - \frac{\omega^2}{\omega_0^2})} \tag{2.10}$$
$$\omega_0 = \frac{1}{\sqrt{L \cdot C_{tot}}}$$

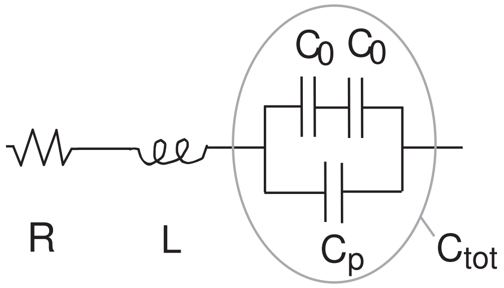

Figure 2.34: Equivalent circuit of device structure without resonance. It includes lead inductance and resistance and the parasitic capacitance caused by the lead structures.

The capacitance C_{tot} includes a parasitic capacitance C_p depending on the design of the device, this capacitance is caused by the alternating electric field between the silicon substrate and the top electrode of the device, which is much bigger than the top electrode of the resonator structure. The value for the parasitic capacitance was estimated using two methods. Firstly by comparing devices with different resonator sizes and extrapolating the size to zero the value of the parasitic capacitance could be determined. The other method was to destroy the membrane mechanically and measure the capacitance of the residual structure. Both these methods lead to very similar values. The total capacitance extracted from the fit of the admittance data was used to calculate the dielectric constant according to:

$$\varepsilon_{33,f} = \frac{(2(C_{tot} - C_p)) \cdot d}{A \cdot \varepsilon_0} \tag{2.11}$$

The values for the dielectric constants derived from measurements from 50 MHz to 2 GHz evaluated as described above are shown in Figure 2.35 and Table 2.4. The data could be fitted using a constant total capacitance, which means that the variation of the dielectric constant lies within the experimental error. In Table 2.4 the values for the dielectric constant from low frequency measurements are also displayed. The values measured at high frequencies are reduced by 30-50% compared to the low frequency dielectric constants. Although this reduction is expected, the effect is difficult to quantify because the applied measurement technique is prone to significant errors. Nevertheless the constant ε value in the range of 50 MHz to 2 GHz is a fact and means that domain wall mobility of mostly 180° domains hardly changes. The contribution of the ferroelastic domain walls to the dielectric constant is either weak, or constant in the considered frequency range.

To compare the field dependence of the films at low and high frequencies the network analyser was equipped with a voltage source. The obtained admittance data was evaluated as above, measuring from 0 kV/cm to up to 25 kV/cm every 2.5 kV and fitted to obtain

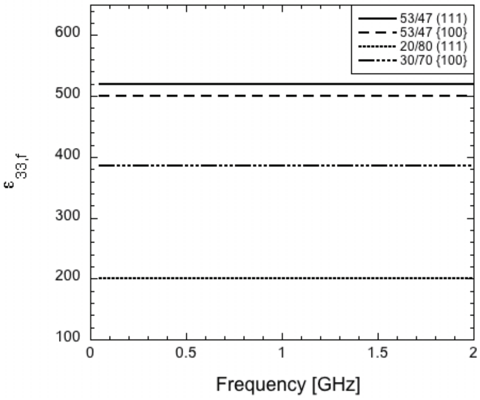

Figure 2.35: Dielectric constant vs. frequency derived from impedance data of a double capacitance structure.

Film	growth method	$\varepsilon_{33,f}$ 50 MHz to 2 GHz	$\varepsilon_{33,f}$ 5 kHz
53/47 (111)	sol-gel	520	800
53/47 {100}	sol-gel	500	1050
20/80 (111)	sputtered	200	400
30/70 {100}	sol-gel	385	520

Table 2.4: Overview of dielectric constants at zero field from impedance measurements (50 MHz - 2 GHz) on the unreleased device structure and from low frequency measurements on simple capacitance structures.

a value for the dielectric constant. Loops of dielectric constant versus electric field are shown for a sol-gel $Pb(Zr_{0.53}, Ti_{0.47})O_3$ film in Figure 2.36. The data measured on the simple capacitance structure of the same films was plotted for comparison. The shape of the two curves is similar, indicating the domain wall mobility up to 2 GHz is comparable to the mobility at 5 kHz.

The dielectric constant as a function of the electric field for the tetragonal films showed no measurable variation. As for the measurements of the dielectric constant versus frequency the variations of the dielectric constant for the tetragonal films with applied electric field are within the experimental errors and thus can not be observed.

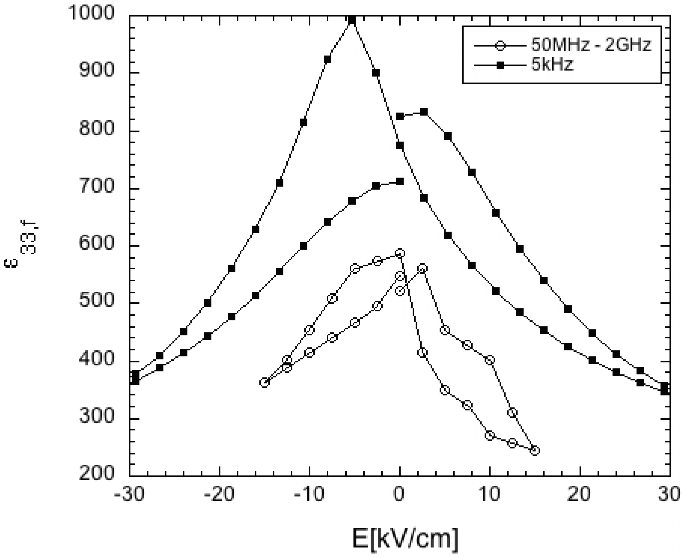

Figure 2.36: Dielectric constant vs. electric field for a sol-gel Pb(Zr$_{0.53}$, Ti$_{0.47}$)O$_3$ film from impedance measurements (50 MHz - 2 GHz) on the unreleased device structure and from low frequency measurements on a simple capacitance structures.

2.5 Piezoelectric characterisation

In order to measure the longitudinal piezoelectric coefficient, referred to as $d_{33,f}$, a double beam laser interferometer setup was used as shown in Figure 2.37. Details on this setup can be found in reference [39]. The interferometer measures the converse piezoelectric effect, i.e. change in physical dimensions due to an applied electric field, perpendicular to the film plane. This corresponds to the longitudinal piezoelectric coefficient in the direction (*hkl*), where (*hkl*) refers to the orientation of the film. The piezoelectric constant $d_{33,f}$ was measured using an AC voltage of 0.1 V at 5 kHz, superimposing a DC voltage of up to 20 kV/cm.

To compare the obtained data the films were grouped in films with a composition at the MPB and tetragonal films as in Section 2.4. In Figure 2.38 the $d_{33,f}$ coefficient as a function of electric field is shown for two Pb(Zr$_{0.53}$, Ti$_{0.47}$)O$_3$ films, the (111) textured film having a thickness of 2 μm and the {100} textured film, a gradient free film with a thickness of 1 μm. The influence of the orientation on the piezoelectric properties has been theoretically predicted by Du *et al.* [80, 81]. Figure 2.39 shows the piezoelectric constants $d_{33,f}$ of PZT for various compositions around MPB depending on the film orientation. On the tetragonal side of the boundary a higher piezoelectric constant for the [001] orientation than for the [111] orientation. The experimental data for ceramics plotted in the same

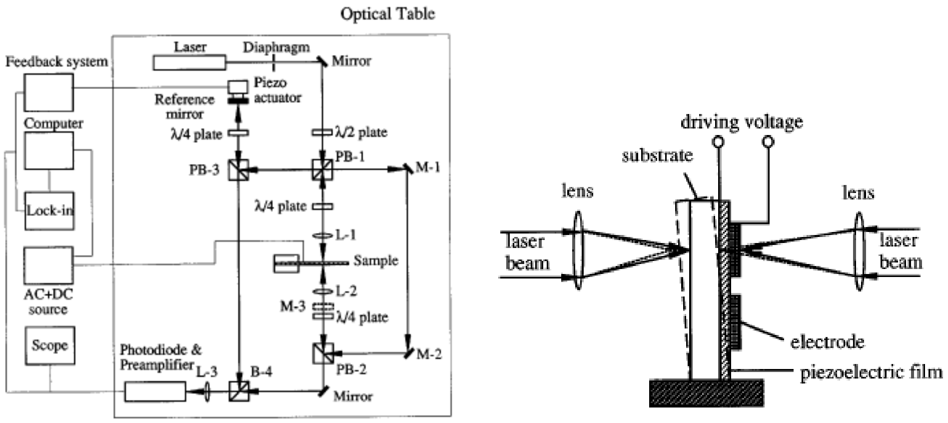

(a) (b)

Figure 2.37: (a) Schematic of double beam laser interferometer setup (b) principle of the elimination of bending motion (From [39]).

graph show values significantly lower than those from calculations on single crystals. This is explained by the random orientation of the grains in the ceramic material. Experimental investigations on the orientation dependency of the piezoelectric constant $d_{33,f}$ have been reported by Taylor and Damjanovic [85] for rhombohedral PZT 40/60 films and found results that agreed qualitatively with the theoretical predictions, i.e. a higher coefficient for the {100} textured films ($d_{33,f} = 100$ pm/V) and a lower value for the (111) textured films ($d_{33,f} = 63$ pm/V). In Table 2.5 experimental values of d_{33} depending on the film orientation at compositions near the MPB from this work and from other groups [54,64,86] are compared. It can be seen that all values agree with the theoretical predictions.

The $d_{33,f}$ constant for the tetragonal films are shown in Figure 2.40. In this graph two measurements are of sputtered $Pb(Zr_{0.20}, Ti_{0.80})O_3$ films with 1 μm thickness and a preferential orientation of either (111) or {100}. The third measurement depicted in Figure 2.40 was performed on a 1 μm thick $Pb(Zr_{0.30}, Ti_{0.70})O_3$ film prepared by the sol-gel method. As expected the piezoelectric coefficient $d_{33,f}$ is lower for these compositions than for the compositions around the MPB. Again we can observe higher values for {100} textured films in comparison to (111) textured films. Hiboux [84] measured the $d_{33,f}$ coefficient on sputtered films with tetragonal compositions and obtained around 20 pm/V for (111) textured 20/80 films and around 35 pm/V for the {100} textured films. The same tendency with higher values for the {100} films was observed but the values are slightly lower than the data shown in Figure 2.40.

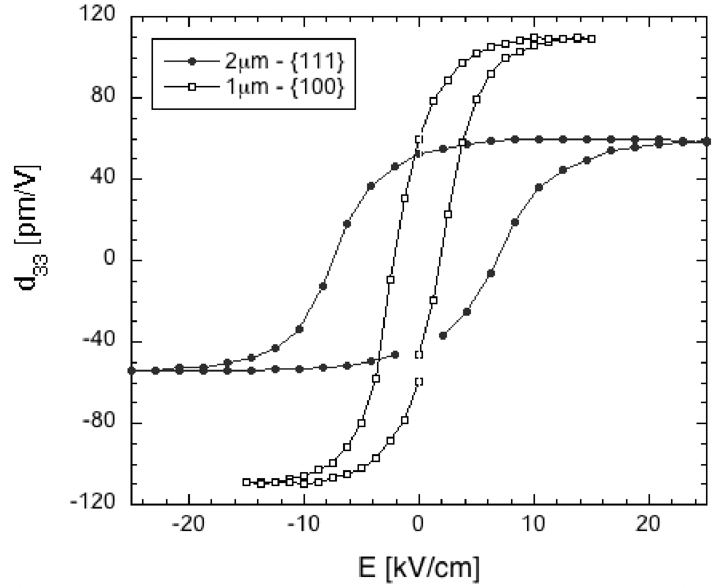

Figure 2.38: Piezoelectric constant $d_{33,f}$ vs. electric field for Pb(Zr$_{0.53}$, Ti$_{0.47}$)O$_3$ films with either a (111) or a {100} preferred orientation. The (111) textured film has a thickness of 2 μm, whereas the {100} textured film has a thickness of 1 μm and was produced by the gradient free sol-gel route.

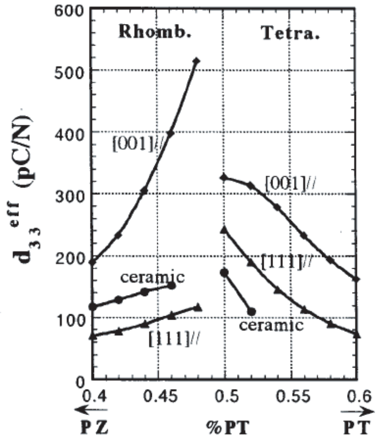

Figure 2.39: Theoretical predictions for the piezoelectric constant $d_{33,f}$ depending on the films orientation for PZT compositions around the morphotropic phase boundary (from Du [80]).

2.6 Summary

Sol-gel and sputtered PZT films with varying compositions and textures have been fabricated on platinised silicon substrates. Advantages and disadvantages of growth techniques

Table 2.5: Overview of literature results for $d_{33,f}$ values for PZT films close to the morphotropic phase boundary.

Author	**Composition**	**Deposition method**	$d_{33,f}$ **(100) [pm/V]**	$d_{33,f}$ **(111) [pm/V]**	**Reference**
Taylor *et al.*	60/40	sol-gel	100	63	[85]
Lian *et al.*	52/48	sol-gel	98	86	[87]
Cho *et al.*	52/48	sol-gel	85	60	[86]
Hiboux *et al.*	45/55	sputtering	80	50	[54]

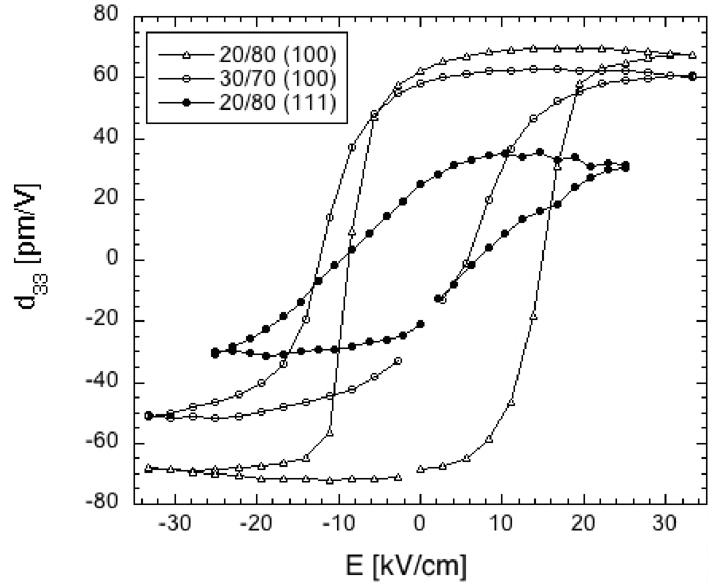

Figure 2.40: Piezoelectric constant vs. electric field of a {100} textured, 1 μm thick Pb($Zr_{0.30}$, $Ti_{0.70}$)O_3 film deposited by sol-gel and two 1 μm thick Pb($Zr_{0.20}$, $Ti_{0.80}$)O_3 films deposited by sputtering with either a {100} or a (111) preferred orientation.

have been described. Both sol-gel and sputtered films can be textured using seed layers: TiO_2 to achieve a (111) and $PbTiO_3$ for a {100} texture.

Films with compositions either at the morphotropic phase boundary or tetragonal were characterised in terms of crystal structure, morphology, dielectric and piezoelectric properties. All films have a dense, columnar grain structure and are well textured. The dielectric constants are comparable to literature values. From the field dependance of the dielectric constant a lower mobility of domain walls contributing to the dielectric constant was observed for tetragonal films than for films at the morphotropic phase boundary. In order to obtain the frequency dependance of the PZT impedance data of a capacitance structure were collected from 50 MHz to 2 GHz. This data could be fitted using an equivalent circuit without any variation of the dielectric constant in this frequency range. This indicates the involved domain wall mobility hardly changes up to 2 GHz.

The interferometry measurements confirmed higher piezoelectric constants for {100} textured films than for (111) textured films and higher piezoelectric constants for the compositions at the morphotropic phase boundary than for the tetragonal compositions. The materials parameters described in this Chapter will be compared to parameters derived from the impedance data of the PZT TFBARs in Section 3.5.

Special attention is paid to the stress state of {100} textured tetragonal films in this Chapter, since the stress state, the domain configuration and the properties of the films are correlated. For BAW applications a *c*-axis orientation would be ideal. The influence of a vacuum annealing treatment with and without externally applied stress has been studied. The detailed mechanism by which the vacuum anneal influences domain formation and film stress is not yet well understood. As the misfit strain S_m is increased by the vacuum anneal, one cannot ascribe the effect to an increase of the lattice constants by oxygen vacancy formation. The effect is rather compatible with the idea that the 550°C annealing temperature is close to θ_C, leading to an $a_1/a_2/a_1/a_2$ pattern during the anneal in order to relax the tensile stress in the film. The role of the oxygen vacancies and electrons formed at the same time, is not clear. They may help to stabilise the ferroelectric ordering above the expected θ_C. This mechanism would explain why the strain S_m increases for a film annealed in vacuum, but not for a film annealed in oxygen.

Chapter 3

TFBAR Fabrication and Characterisation

In this Chapter PZT films with either tetragonal or MPB composition and (111) or {100} texture (as described in Chapter 2) are characterised in bulk acoustic wave resonators at frequencies of either 400 MHz, 900 MHz or 2 GHz. Parameters significant for resonator characterisation are extracted, as well as materials parameters of the films at high frequencies. This Chapter is divided into five sections. The first section will describe the design and fabrication steps used to produce the test structures. The second will introduce the methods of measurement and the models used to characterise the resonators. The third section presents the results obtained from the numerical models for each type of PZT film. In the fourth section the field dependency of a resonator based on 53/47 PZT with a (111) orientation is presented. The last section compares materials parameters obtained from simulations to measured values or to literature values.

3.1 Resonator design and fabrication steps

3.1.1 Design

The thin film bulk acoustic wave resonators (TFBARs) used in this work are based on a membrane structure to confine the bulk acoustic wave in the piezoelectric film. In order to avoid etching of the PZT film to access the bottom electrode the design uses a double resonator structure [88] according to Figure 3.1. In this design two resonators are in series. For the present work devices with resonance frequencies of around 400 MHz, 900 MHz and 2 GHz were targeted. This results in film thicknesses of 4 μm, 2 μm and 1 μm, respectively.

These values are approximate since they don't take mechanical loading of the electrodes and other additional layers into account. For optimal power transfer and the device has to be matched to 50 Ohm impedance. This can be adapted by adjusting the area of the device. The impedance can be approximated as:

$$Z_0 \approx \frac{1}{\omega C} \approx 50\Omega \tag{3.1}$$

Expressing this same formula with the dimensions and materials parameters of the device one obtains the device surface a^2 matched to Z_0 as:

$$a^2 \approx \frac{t}{\omega \varepsilon Z_0} \tag{3.2}$$

Since the dielectric constant is variable the impedance can not be matched for different film compositions and orientations. In order to impedance match with variable dielectric constants, but also to have a design that can be used at different frequencies five different sizes were chosen: 60 x 60 μm, 50 x 50 μm, 45 x 45 μm, 40 x 40 μm and 30 x 30 μm. The design of the electrodes will change the resistivity and inductance of the device, but no special attention was paid to these effects since they can be included when modelling. One main design was used, which is shown in Figure 3.2. Variations of this design include rounded resonators and a design with a smaller top electrode area to reduce the resistance and parallel capacitance shown in Figures 3.3a and 3.3b, respectively. Apart from the bottom electrode, additional platinum surfaces next to the resonator and surrounding the whole device were added. These surfaces were added for the sputtering process, in order to minimise temperature instabilities. Since the process temperature of the sputtering system is calibrated using wafers completely covered with platinum and the processes were not reproducible on the device wafers, the emission of heat from the surfaces not covered with platinum were thought to be responsible for reduced heating of device wafers.

3.1.2 Process flow

In this paragraph the fabrication steps to realise a TFBAR with a double resonator membrane structure shall be briefly explained. The substrates used were Si (001) wafers covered with 100 nm of thermal oxide. A Ti/TiO_2 (2 nm / 10 nm) adhesion layer was sputter deposited onto the substrate prior to the deposition of the 100 nm Pt bottom electrode (either using the Nordiko 2000 or the BAS 450 system). The bottom electrode was patterned by dry etching using a photoresist mask. The etching is done using chlorine chemistry in a dry etcher (STS multiplex ICP). Subsequently the PZT film was deposited on top by

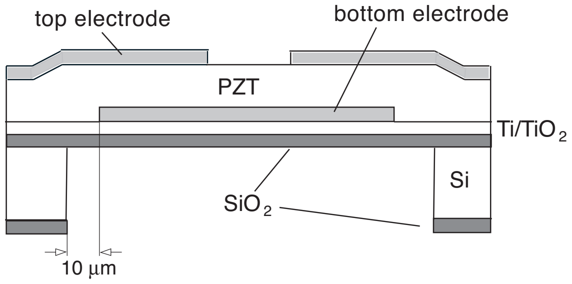

Figure 3.1: Schematic cross-section of a TFBAR with double resonator membrane structure.

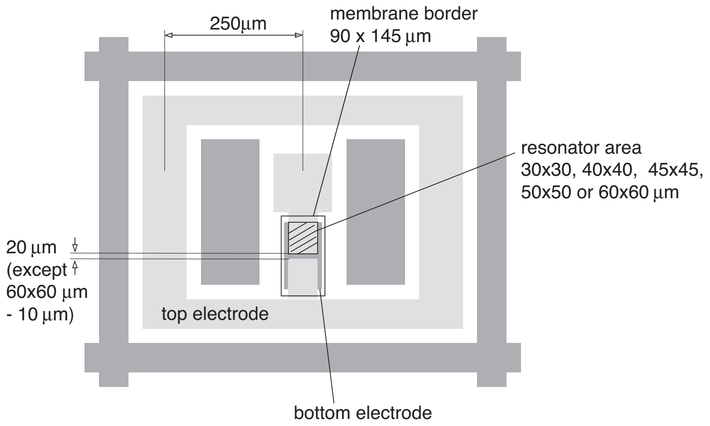

Figure 3.2: Schematic top view of a TFBAR with double resonator membrane structure.

sputtering or by spin coating with a sol-gel solution as described in the previous Chapter. A TiO_2 seed layer (2 nm) was sputter deposited onto the bottom electrode to promote the {111} orientation of the PZT film or a $PbTiO_3$ layer (20 nm), sol-gel or sputtered, to promote {100} orientation were deposited prior to the deposition of the PZT film. After the deposition of the PZT film the Pt top electrode (100 nm) was sputter deposited at room temperature using the BAS system. The top electrode was then structured by dry etching with chlorine chemistry using a photoresist mask. To liberate the membrane the wafer was structured and dry etched (deep silicon etching, Bosch process) from the back side (Alcatel 601E, Dry etcher, fluorine chemistry). For this process another mask was used, which makes a total of three lithography steps. Resonator devices with dimensions

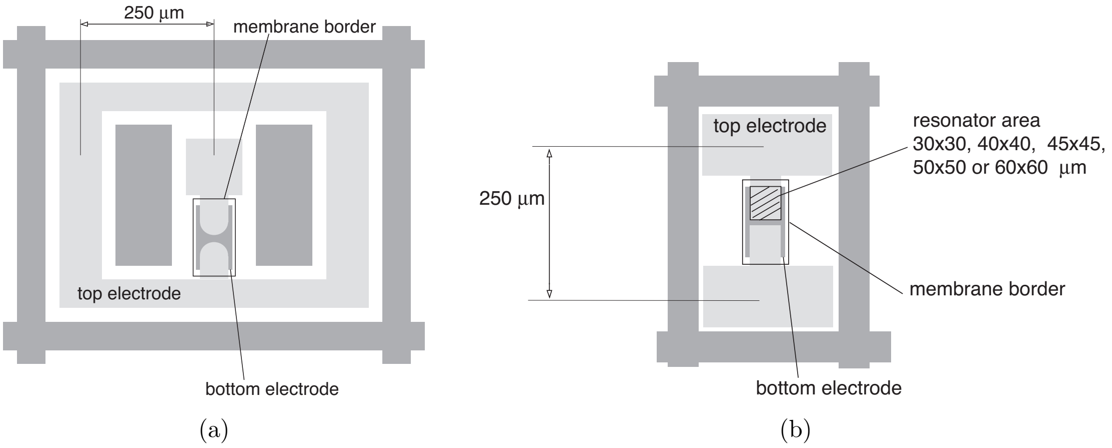

Figure 3.3: Schematic top view of a TFBAR with double resonator membrane structure. (a) A three port structure with rounded top electrodes. (b) Two port structure with angular electrodes.

ranging from 30 μm to 60 μm were obtained. An overview of this process flow is shown in Figure 3.4.

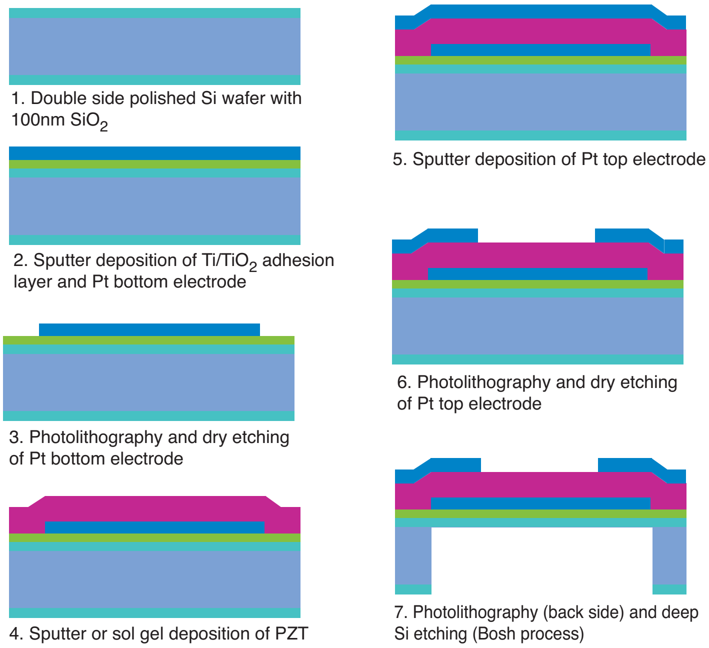

Figure 3.4: Process flow showing the steps to realise a TFBAR with double resonator membrane structure.

Typical images of finished devices are shown in Figures 3.5 and 3.6. These Figures show devices with double resonator membrane structures, the images in Figure 3.5 have a three port structure (Ground-Signal-Ground), whereas the images in Figure 3.6 have a two port structure (Ground-Signal). The two variations with either an angular or rounded top electrode were present on all designs. The design with the two port structure was only used for the resonators based on 4 μm thick PZT. In the images in Figure 3.5 the PZT is translucent and the cavity in the silicon appears dark. This was observed for all devices apart from the devices with 4 μm thick PZT, which is no longer translucent.

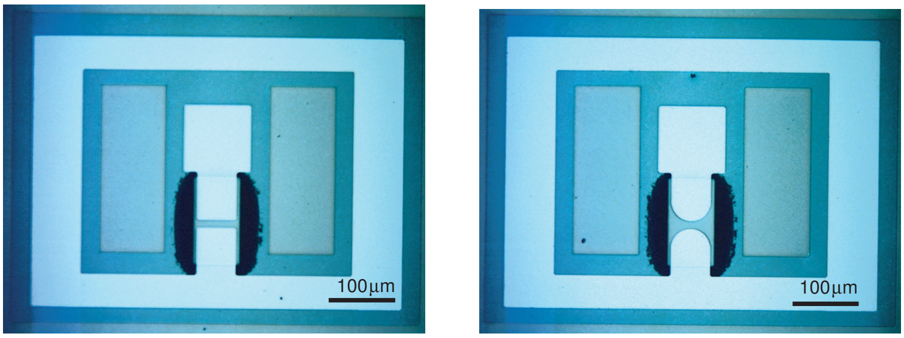

(a) (b)

Figure 3.5: Optical microscopy image of a TFBAR top view with double resonator membrane structure with a three port design (a) with angular top electrodes (b) with rounded top electrodes.

A SEM image of a membrane cross-section is shown in Figure 3.7. The membrane is broken at the right edge due to sample preparation. Top electrodes for the double resonator membrane structure can be recognised on top of the PZT membrane.

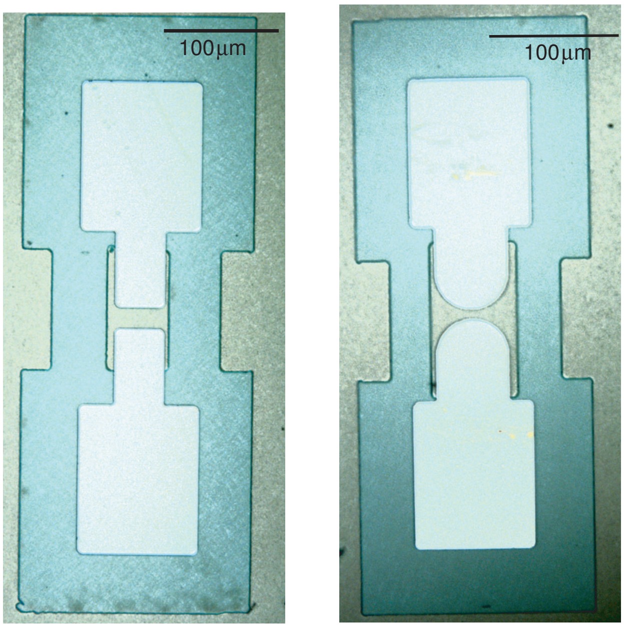

(a) (b)

Figure 3.6: Optical microscopy image of a TFBAR top view with double resonator membrane structure with a two port design (a) with angular top electrodes (b) with rounded top electrodes

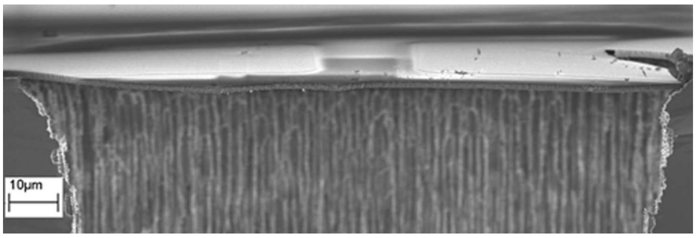

Figure 3.7: SEM image of a membrane cross-section showing the double resonator structure.

3.2 Resonator measurement and modelling

The resonators were characterised by measuring the frequency response using an HP 8722D network analyser (Agilent Technologies, Palo Alto, CA). The S_{11} scattering parameters obtained from these measurements were used to calculate the electrical admittance Y defined in Equation 3.3. To observe the influence of the polarisation of the films on the response of the resonators the network analyser was equipped with a voltage source used for biasing the samples.

$$Y = \frac{1}{Z_0}\left(\frac{1-S_{11}}{1+S_{11}}\right) \tag{3.3}$$

The admittance data obtained from the measurements of the S_{11} scattering parameter using the network analyser were simulated using two different methods. To achieve an optimal fit of the admittance data the resistivity R_s and inductance L_s of the electrodes need to be taken into account as shown in Figure 3.8a. The inductance of the electrodes is due to parallel conduction lines in the design of the device, which are not adjusted to 50 Ohm. This results in a value of around 0.1 nH for L_s. A small capacitance C_p in parallel to the resonator was added to take the parasitic capacitance of the device into account. To simulate the resonator shown in Figure 3.8a two methods were used. One method was to use an equivalent circuit model based on the Butterworth Van-Dyke (BVD) model as shown in Figure 3.8b.

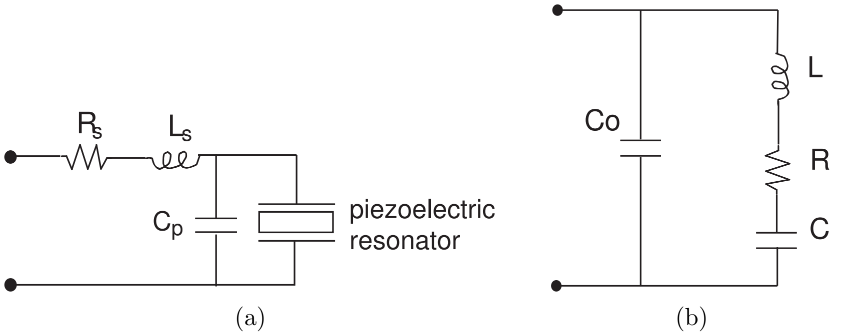

Figure 3.8: (a) General schematic of the equivalent circuit including parasitic elements used, (b) Schematic of the Butterworth Van-Dyke (BVD) equivalent circuit model used for the piezoelectric resonator.

The BVD model uses four real circuit parameters to represent the impedance of a piezoelectric resonator, the resistance-inductance-capacitance (RLC) circuit to describe the resonance and C_0, which represents the clamped capacitance of the transducer plate. It provides an accurate fit for a single resonance of a material without any significant losses. To take the losses into account the model can be generalised by representing the losses as complex components [89]. In this work the dielectric losses were taken into account by considering the bulk capacitance C_0 to be complex (see Equation 3.4).

$$\begin{aligned} Y &= i\omega C_0 = \omega C_0'' + i\omega C_0' \\ \text{with } \frac{C_0''}{C_0'} &= tan\delta \\ Y &= \omega C_0 tan\delta + i\omega C_0 \end{aligned} \tag{3.4}$$

Using the equivalent circuit parameters the resonance f_r and antiresonance f_a frequencies, the coupling constant k_t^2 and the quality factor Q are given by the following Equations 3.5 - 3.8.

$$f_r = \frac{1}{2\pi\sqrt{LC}} \tag{3.5}$$

$$f_a = f_r\sqrt{1 + \frac{C}{C_0}} \tag{3.6}$$

$$Q = \frac{\sqrt{LC}}{RC} \tag{3.7}$$

$$k_t^2 = \frac{C}{C_0} \tag{3.8}$$

Another way the admittance of a piezoelectric resonator can be derived is by using the linear equations of piezoelectric elasticity [90] for a one-dimensional case. In Ref. [90] the electrical impedance was expressed in terms of piezoelectric materials properties and the impedances of the mechanical loads of the resonator. Using the expression derived in Ref. [90] (see Equation 3.9) the resonators were modelled taking the electrodes and the SiO_2 layer into account.

$$Z = \frac{1}{i\omega C_0}(1 - k_t^2 \frac{\tan\phi}{\phi} \frac{(z_r + z_l)\cos^2\phi + i\sin 2\phi}{(z_r + z_l)\cos 2\phi + i(z_r z_l + 1)\sin 2\phi}) \tag{3.9}$$

where $\omega = 2\pi f$ is the angular frequency, $\phi = \omega t/2v_D$ with $v_D = \sqrt{(c_{33}^D/\rho)}$ the sound velocity and t the thickness of the piezoelectric film, c_{33}^D the elastic stiffness at constant electric displacement and ρ is the density of the piezoelectric material. The coupling constant k_t^2 for pure thickness mode vibration can be calculated using materials parameters as defined in Chapter 1 (Equation 1.9). Material losses were included in the model by adding complex terms to the clamped capacitance C_0, the elastic stiffness and the dielectric constant. All structures attached to the piezoelectric resonator, in this case the electrodes and the SiO_2 layer, need to be included in the mechanical load impedances z_l and z_r which are the terminating impedances at the left side and at the right side of the structure, respectively. These can be calculated by the successive use of the transmission line equation and need to be normalised by the impedance of the piezoelectric film as described in Ref. [90].

3.3 Numerical model simulation results

In this section all fabricated devices shall be described by showing typical impedance data and using the two models described above to extract resonator characteristics and materials parameters. Constants used for the fit using materials parameters are summarised in Table 3.1.

constants	
SiO_2 thickness [μm]	0.1
v_{SiO_2} [m/s]	5790
v_{Pt} [m/s]	4320
Z_{SiO_2} [N s/m^3]	$1.28{\cdot}10^7$
Z_{Pt} [N s/m^3]	$8.64 \cdot 10^7$
Z_{PZT} [N s/m^3]	$2.98 \cdot 10^7$
ρ [kg/m^3]	7750

Table 3.1: Constants used in the model based on materials parameters as described in Section 3.3.

Resonator based on sol-gel 53/47 PZT with preferred (111) orientation

These resonators were fabricated using 2.1 μm thick sol-gel PZT with a composition at the morphotropic phase boundary. One problem encountered during fabrication of these devices was cracking of the sol-gel film. The surface of the wafer before deposition of sol-gel PZT is largely SiO_2 with a thin layer of TiO_2 (2 nm) used as a seed layer on the platinum. The platinum bottom electrodes only cover a very small surface in this first design used. The SiO_2/TiO_2 surface is not an ideal surface to grow PZT as diffusion into the substrate can take place leading to pyrochlore formation and large stresses in the film. Nevertheless many devices had no cracks and could be measured. The devices were not poled before measuring, but a DC field applied simultaneously to the measurement was used to orient the domains. Figure 3.9 shows typical impedance data as well as the curves used to fit the data via an equivalent circuit model and a model based on materials constants as described in Section 3.3. The data shown in Figure 3.9 was measured with an applied bias of 15 kV/cm, which results in 7.5 kV/cm per resonator since it is a double resonator structure. Table 3.2 shows the parameters used for fitting this data. Both models result in similar values for Q-factor and coupling constant k_t^2. The Q-factor of around 50 and coupling constant of about 0.25 are the highest values found for PZT in TFBARs in this study. These devices were used to study the field dependency of resonance frequencies and coupling constant, which shall be presented in Section 3.4.

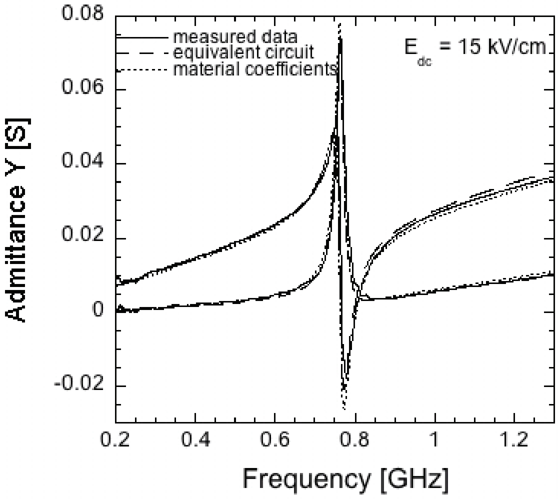

Figure 3.9: Frequency response of a TFBAR based on 2.1 μm thick sol-gel 53/47 PZT film with a preferred (111) orientation shown as real and imaginary part of the admittance characteristics. Simulated curves are plotted as dotted lines.

common parameters			
L_s [nH]	0.01		
R_s [Ω]	6		
C_p [pF]	3.05		
equivalent circuit parameters		**material coefficients**	
L [nH]	90	PZT thickness [μm]	2.1
R [Ω]	8.2	Pt thickness [μm]	0.1
C [pF]	0.48	SiO_2 thickness [μm]	0.1
C_0 [pF]	2	v_D [m/s]	4846
$\tan\delta$	0.01	ρ [kg/m^3]	7750
f_r [GHz]	0.766	ε_{33}^S	260
f_a [GHz]	0.852	e_{33} [C/m^2]	10
		c_{33}^D [GPa]	180
		$\tan\gamma$	0.017
		$\tan\delta$	0.01
		$d_{33,f}$ [pm/V]	79
Q	52.8	Q	58.8
k_t^2	0.240	k_t^2	0.240
k_t^2 *Q	12.672	k_t^2 *Q	14.112

Table 3.2: Comparison of parameters from equivalent circuit and material coefficients models used to simulate resonance of a 2.1 μm thick sol-gel 53/47 PZT TFBAR with (111) preferential orientation with an applied electric field of 15 kV/cm.

Resonator based on sol-gel 53/47 PZT with preferred {100} orientation

The devices based on sol-gel 53/47 PZT with preferred {100} orientation were fabricated using the gradient-free sol-gel route for the deposition of the PZT film. The design was slightly adapted for these devices, in order to have a large surface of the wafer covered with platinum. This prevented the formation of pyrochlores and cracking of the film. The impedance data and simulated curves are shown in Figure 3.10 and the parameters used for fitting are shown in Table 3.3. Both models show similar results. When looking at the parameters obtained from the fit using materials coefficients a high tanγ is observed, i.e. the film has high elastic/acoustic losses, which results in a low Q-factors (Q=1/tanγ). These high losses are thought to be caused by the vibration of domain walls in the electric field. The vibrations of elastic domain walls are thought not to play a role for the (111) oriented films and to have a bigger influence for {100} oriented films as discussed in Chapter 1. When comparing devices based on 53/47 PZT with preferred (111) orientation (see below) with these devices this prediction was confirmed.

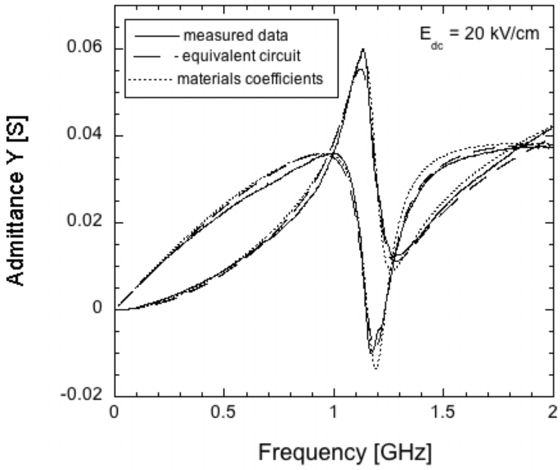

Figure 3.10: Frequency response of a TFBAR based on a 1 μm thick sol-gel 53/47 PZT film with a preferred {100} orientation shown as real and imaginary part of the admittance characteristics. Simulated curves are plotted as dotted lines.

Resonator based on sputtered 20/80 PZT with preferred (111) orientation

The tetragonal composition was chosen in order to have less movement of domain walls which should result in lower elastic losses. The 1 μm thick (111) textured PZT film was fabricated by sputtering on a TiO_2 seed layer. For sputtered films no problems of cracking were encountered even for the design with little platinum coverage of the wafer. Typical impedance data is shown in Figure 3.11 and the parameters used for fitting are shown in Table 3.4. Again the two models correspond very well. The Q-factor of around 65 is the highest value measured in this work. However the piezoelectric coefficients found for the (111) textured tetragonal composition are low, which results in a low coupling constant of only 0.03. The material parameters will be discussed in Section 3.5.

Resonator based on sol-gel 30/70 PZT with preferred {100} orientation

Sol-gel deposited tetragonal films with a preferred {100} orientation were also used for device fabrication. The {100} orientation should provide higher piezoelectric coefficients than the (111) orientation, but since these films have a lot of (100) domains the coefficients

common parameters			
L_s [nH]	0.01		
R_s [Ω]	13		
C_p [pF]	3.69		
equivalent circuit parameters		**material coefficients**	
L [nH]	15	PZT thickness [μm]	1.0
R [Ω]	6.0	Pt thickness [μm]	0.15
C [pF]	1.30	SiO_2 thickness [μm]	0.1
C_0 [pF]	3.2	v_D [m/s]	5389
$\tan\delta$	0.01	ρ [kg/m^3]	7750
f_r [GHz]	1.14	ε_{33}^S	192
f_a [GHz]	1.352	e_{33} [C/m^2]	11.5
		c_{33}^D [GPa]	225
		$\tan\gamma$	0.045
		$\tan\delta$	0.01
		$d_{33,f}$ [pm/V]	100
Q	18	Q	22
k_t^2	0.41	k_t^2	0.36
$k_t^2 {*} Q$	7.38	$k_t^2 {*} Q$	7.92

Table 3.3: Comparison of parameters from equivalent circuit and material coefficients models used to simulate resonance of a 1 μm thick sol-gel 53/47 PZT TFBAR with {100} preferential orientation with an applied electric field of 20 kV/cm.

in z direction are low (see Section 2.4.2). The impedance data for a device based on 30/70 {100} textured sol-gel PZT are shown in Figure 3.12 with the corresponding data used for fitting presented in Table 3.5. As observed for the other film with {100} texture the elastic losses in this film is high resulting in a low Q-factor. The coupling constant is higher than for the (111) textured film as expected, but with the low Q-factor it results in a similar figure of merit as the 20/80 (111) textured films.

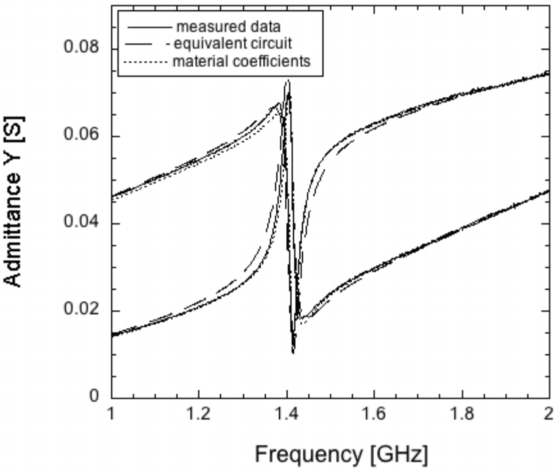

Figure 3.11: Frequency response of a TFBAR based on a 1 μm thick sputtered 20/80 PZT film with a preferred (111) orientation shown as real and imaginary part of the admittance characteristics. Simulated curves are plotted as dotted lines.

common parameters			
L_s [nH]	0.1		
R_s [Ω]	6		
C_p [pF]	3.49		
equivalent circuit parameters		**material coefficients**	
L [nH]	80	PZT thickness [μm]	1.0
R [Ω]	10.8	Pt thickness [μm]	0.1
C [pF]	0.16	SiO_2 thickness [μm]	0.1
C_0 [pF]	4.1	v_D [m/s]	4501
$\tan\delta$	0.02	ρ [kg/m^3]	7750
f_r [GHz]	1.406	ε_{33}^S	248
f_a [GHz]	1.434	e_{33} [C/m^2]	3.1
		c_{33}^D [GPa]	157
		$\tan\gamma$	0.015
		$\tan\delta$	0.02
		$d_{33,f}$ [pm/V]	20
Q	65.5	Q	67
k_t^2	0.04	k_t^2	0.03
k_t^2 *Q	2.32	k_t^2 *Q	2.01

Table 3.4: Comparison of parameters from equivalent circuit and material coefficients models used to simulate resonance of a 1 μm thick sputtered 20/80 PZT TFBAR with (111) preferential orientation at zero applied field.

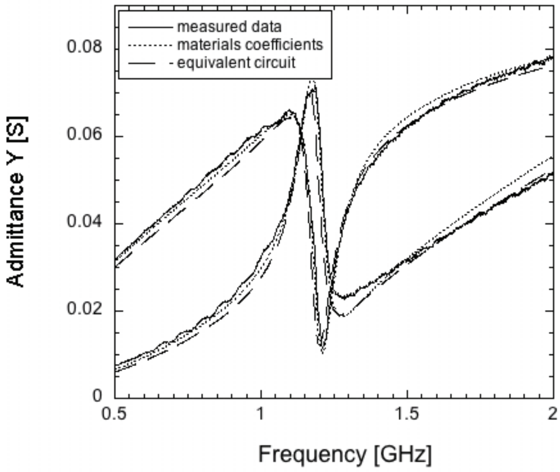

Figure 3.12: Frequency response of a TFBAR based on a 1 μm thick sol-gel 30/70 PZT film with a preferred {100} orientation shown as real and imaginary part of the admittance characteristics. Simulated curves are plotted as dotted lines.

Resonator based on thick sol-gel 53/47 PZT with preferred {100} orientation

VHF (very high frequency : 30-300 MHz) ultrasonic imaging belongs to the new developments in diagnostic ultrasound with in applications dermatology, ophthalmology and intravascular imaging [91]. The devices described in this section were made to resonate around 400 MHz (film thickness of about 4 μm) in order to explore coupling constant and Q-factor at frequencies close to VHF. Devices for ultrasonic imaging do not require high Q-factors since they are used as transducers to send a wave pulse. Still they need to be able to make devices with high sensitivity and bandwidth, which means a high coupling constant is necessary. Resonators with the same design (see Section 3.1.1) as the devices described above but with a PZT film thickness of 3.8 μm were fabricated using sol-gel PZT with a 53/47 composition. A SEM cross-section of the device and of the thick PZT film are shown in Figure 3.14. The thick PZT film lead to some difficulties in aligning since the alignment marks were difficult to see. The misalignment resulted in a size difference of the two resonators composing the double resonator. The difference in size lead to unequal distribution of the electric field, which means two resonance frequencies can be identified. This needed to be taken into account to fit the data more accurately. The impedance data is shown in Figure 3.15 together with the fit using an equivalent circuit model for two resonators with slightly different parameters. The corresponding parameters are presented in Table 3.6. The impedance data is not easy to interpret since their

common parameters			
L_S [nH]	0.1		
R_s [Ω]	6		
C_p [pF]	3.67		
equivalent circuit parameters		**material coefficients**	
L [nH]	29	PZT thickness [μm]	1.1
R [Ω]	10.5	Pt thickness [μm]	0.1
C [pF]	0.63	SiO_2 thickness [μm]	0.1
C_0 [pF]	5.5	v_D [m/s]	4097
$\tan\delta$	0.02	ρ [kg/m^3]	7750
f_r [GHz]	1.18	ε_{33}^S	406
f_a [GHz]	1.24	e_{33} [C/m2]	7.5
		c_{33}^D [GPa]	130
		$\tan\gamma$	0.060
		$\tan\delta$	0.02
		$d_{33,f}$ [pm/V]	65
Q	20.4	Q	17
k_t^2	0.11	k_t^2	0.12
$k_t^2 {*} Q$	2.24	$k_t^2 {*} Q$	2.04

Table 3.5: Comparison of parameters from equivalent circuit and material coefficients models used to simulate resonance of a 1 μm thick sol-gel 30/70 PZT TFBAR with {100} preferential orientation at zero applied field.

are several resonances at these low frequencies. The peaks fitted were the only ones that showed dependency on the applied electric field. The oscillations observed from around 320 MHz to 800 MHz with a width of around 11 MHz probably correspond to Lamb waves. Simulations using the finite element method (FEM) software package ANSYS show that Lamb waves are indeed present. In the example shown in Figure 3.13, where half of the TFBAR membrane structure at a frequency of 360 MHz is illustrated, a symmetric lamb wave can be identified.

The low Q-factor is expected since the composition is near the morphotropic phase boundary, where losses due to domain oscillations are high and since the orientation is not preferable for low acoustic losses [38, 92]. The coupling constant is known to decrease with increasing frequency, so high coupling constants were also expected and are ideal for ultrasonic imaging applications.

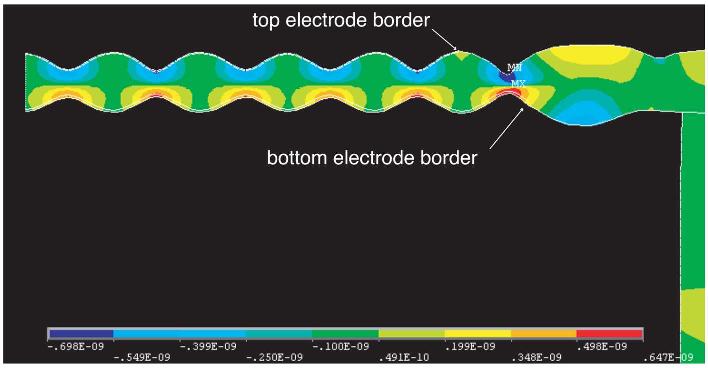

Figure 3.13: Half of a TFBAR membrane structure based on a 3.8 μm thick sol-gel 53/47 PZT film simulated using the finite element method (FEM) software package ANSYS. A symmetric lamb wave can be identified at 360 MHz.

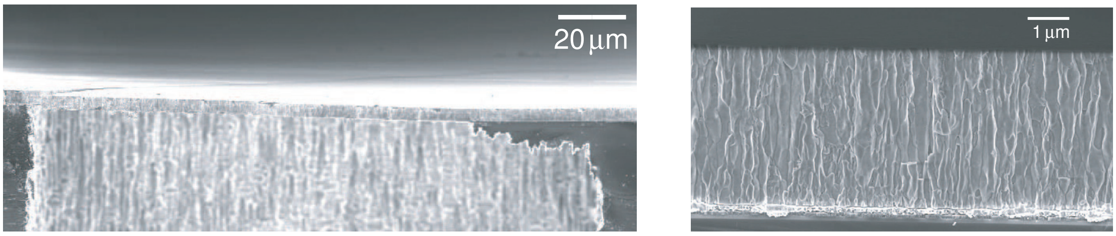

(a)

(b)

Figure 3.14: (a) SEM image of a membrane cross-section of a TFBAR based on a 3.8 μm thick sol-gel 53/47 PZT film with a preferred {100} orientation (b) Close-up view of the PZT film

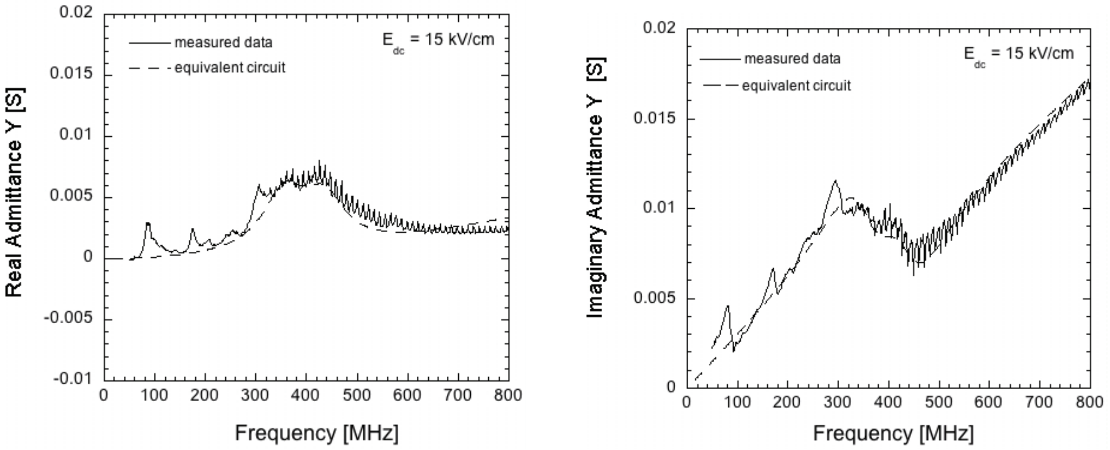

(a) (b)

Figure 3.15: Frequency response of a TFBAR based on a 3.8 μm thick sol-gel 53/47 PZT film with a preferred {100} orientation shown as real (a) and imaginary (b) part of the admittance characteristics at an applied voltage of 15 kV/cm. This electric field was divided unequally between the two resonators due to their varying sizes. Two different resonance frequencies can be distinguished. Simulated curves are plotted as dotted lines.

common parameters			
L_S [nH]	0.01		
R_s [Ω]	10		
C_p [pF]	2.3		
equivalent circuit parameters			
resonator 1		**resonator 2**	
L [nH]	148	L [nH]	113
R [Ω]	90	R [Ω]	70
C [pF]	1.4	C [pF]	1.55
C_0 [pF]	5.5	C_0 [pF]	1.8
$\tan\delta$	0.01	$\tan\delta$	0.01
f_r [MHz]	350	f_r [MHz]	380
f_a [MHz]	390	f_a [MHz]	480
Q	3.6	Q	3.85
k_t^2	0.25	k_t^2	0.86
k_t^2 *Q	0.92	k_t^2 *Q	3.32

Table 3.6: Parameters from equivalent circuit model for the two resonators in series used to simulate resonance of a 3.8 μm thick sol-gel 53/47 PZT TFBAR with {100} preferential orientation at an applied field of 15 kV/cm. This electric field was divided unequally between the two resonators due to their varying sizes. This resulted in different properties of the two resonators.

Resonator based on sputtered 20/80 PZT with preferred {100} orientation

As discussed in Section 2.3 devices based on 20/80 sputtered films with a {100} preferred orientation could not be realised. In order to understand possible fabrication issues Focused Ion Beam (FIB) techniques combined with SEM (FEI Nova 600 NanoLab, dual beam (SEM/FIB)) were used to observe the transition between the PZT grown on the platinum bottom electrode to the PZT grown on SiO_2. Figure 3.16 shows a cross-section of a device membrane at the edge of the bottom electrode, showing the bottom electrode, the PZT film and top electrode. Both on the bottom electrode and on the SiO_2 surface next to the bottom electrode, a columnar grain structure is observed. But the surface of the PZT film is very rough. A zoomed in detail of the same area of the device shown in Figure 3.16a seems to show discontinuity in the top electrode due to the high roughness of the PZT. This was probably the reason why these devices could not be measured.

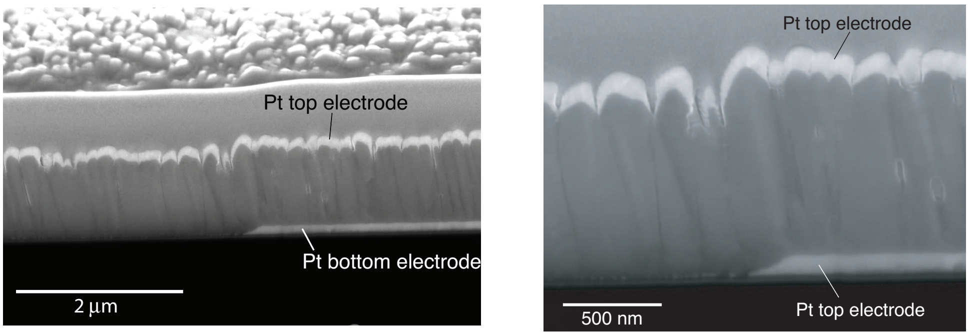

(a) (b)

Figure 3.16: (a) SEM of a FIB cut at the edge of a bottom electrode of a TFBAR structure based on a 1 μm thick sputtered 20/80 PZT film (b) detail of the same area.

3.4 Field dependence of TFBAR characteristics

Field dependency of the resonance and antiresonance frequencies as well as the coupling constant were measured for resonators based on compositions near the morphotropic phase boundary. For devices based on tetragonal compositions no dependency of the parameters on the applied electric field could be observed. As described in Section 2.4.2 the variation of the dielectric constant at frequencies up to 2 GHz could not be distinguished for tetragonal films. The domain walls in tetragonal films seem to be less mobile than in films at the morphotropic phase boundary and do not seem to move much at high frequencies. This keeps the dielectric constant relatively constant. Apart from the dielectric constant the physical parameters changing when applying an electric field are the stiffness or sound velocity ($v_D = \sqrt{\frac{c_{33}^D}{\rho}}$), the thickness of the piezoelectric film and the piezoelectric coefficients. All these parameters interact. What can be observed directly are the variations of the resonance frequency (dependent on the sound velocity v_D and film thickness), antiresonance frequency (dependent on sound velocity v_D, film thickness and coupling constant) and the coupling constant (see 1.9). The movement of domain walls will influence all these parameters.

In order to study the field dependency of resonance and antiresonance frequencies and coupling constant the resonators based on 53/47 (111) textured PZT were chosen. Admittance data for these devices were collected at frequencies from 0.2 to 1.3 MHz at fields ranging from 0 kV/cm to 20 kV/cm for the double resonator, which means 10 kV/cm for each resonator. Resonance and antiresonance frequencies were extracted from the admittance and plotted against the DC field as shown in Figure 3.17. Both frequencies show a strong dependence on the bias field and reflect the ferroelectric hysteresis. From zero to 10 kV/cm the resonance curve drops by 3.4%, while the antiresonance drops by 2.1%. The drop of the antiresonance curve is much larger than the thickness change of 0.14% calculated from $d_{33,f}$, meaning that the stiffness constant c_{33}^D is reduced by the electric field along the average polarisation. Similar hysteresis effects were previously reported by Schreiter *et al.* [27], also on (111)-oriented films, one of tetragonal 25/75 composition, the other of rhombohedral 58/42 composition. The reduction of the (series) resonance frequency of rhombohedral composition (-1.6%) can readily be explained by the increase of k_t^2 with increasing bias. In contrast, however, the antiresonance frequency was not observed to move significantly at this composition, meaning that c_{33}^D was found to be constant in rhombohedral symmetry. In the same work, a shift of the antiresonance curve was reported for the tetragonal film, with the difference, however, that a minimum was reached in the switching region. In our case, the switching region exhibits a maximum, similar to the antiresonance response. Hence, on the one hand we can confirm the trends observed in Ref. [27] that our film of morphotropic composition - thus a mixture of rhombohedral and tetragonal symmetry - should show a variation of both frequencies, on the other hand the behaviour of the antiresonance frequency is opposite. While in Ref. [27] a softening is observed in the domain rich switching region, we deal with a hardening in the switching region, or a softening at high fields. As described in Ref. [27] the coupling constant can be varied from zero to its maximum value. Figure 3.18 shows the bias dependency of the coupling constant derived from impedance data at varying frequencies. The values for the coupling constant were taken from the equivalent circuit model fits as described in Section 3.3.

This frequency dependence of resonance and antiresonance frequencies could be used for tuning of the resonator. Since both frequencies shift when applying an electric field, the coupling constant and thus the bandwidth do not show too much variation when applying an electric field. In Figure 3.19 the same data is shown as in Figure 3.18 but only the positive side of the graph as well as the ratio of f_a/f_r which can be seen to be relatively constant. Restricting to unipolar bias voltages the bandpass region of a filter could be shifted up to 2% with a range of k_t^2 from 8 to 23%.

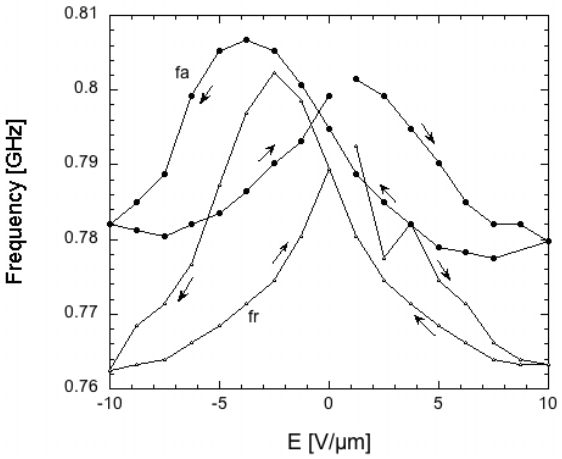

Figure 3.17: Resonance and antiresonance frequency versus electric field for a TFBAR based on a 2.1 μm thick sol-gel 53/47 PZT with a (111) texture.

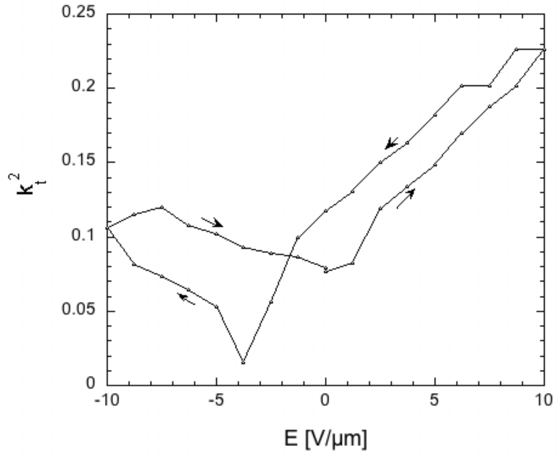

Figure 3.18: Coupling constant versus electric field for a TFBAR based on a 2.1 μm thick sol-gel 53/47 PZT with a (111) texture.

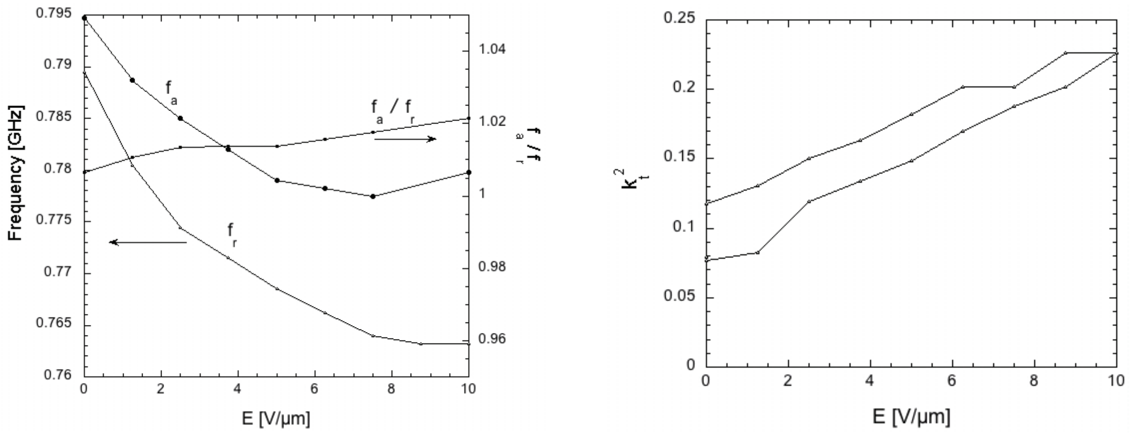

(a) (b)

Figure 3.19: (a) Resonance and antiresonance frequencies vs. positive electric field. Ratio of f_a/f_r is relatively constant. (b) variation of coupling constant when applying a positive field.

3.5 Discussion of derived materials parameters

In this section we discuss the material parameters obtained from the fitting of the resonance impedance data including parameters derived from these values such as the piezoelectric coefficient $d_{33,f}$. The parameters which can be compared to the measurements presented in Chapter 2 are the dielectric constant ε_{33}^S and the piezoelectric constant $d_{33,f}$.

The measurements of the dielectric constant presented in Section 2.4 confirmed the frequency and field dependence of this parameter. The difference between the data obtained from the fits of the resonance and the data shown in Section 2.4 from impedance measurements of the device structures is small. The main difference is that the results shown in Section 2.4 were measured on clamped films, whereas the resonance data describes films no longer clamped to the substrate. Another difference for the films with a MPB composition is the applied field at which the resonance data was measured. This data was thus compared to the field dependent data for ε_{33}^S at high frequencies. In Figure 3.20 the dielectric constants from resonance fitting are compared to high frequency values for the dielectric constants as shown in Section 2.4. It can be seen that the dielectric constants are slightly higher for the free structures than for the clamped films in the case of tetragonal films, which are unpoled. For the compositions at the morphotropic phase boundary, where an electric field is applied, the opposite is the case. This can be explained by the more efficient poling of the unclamped films. The loss tangent $\tan\delta$ is low for all films (0.01 to 0.02) which is slightly lower than the values from low frequency measurements

(0.01 to 0.04).

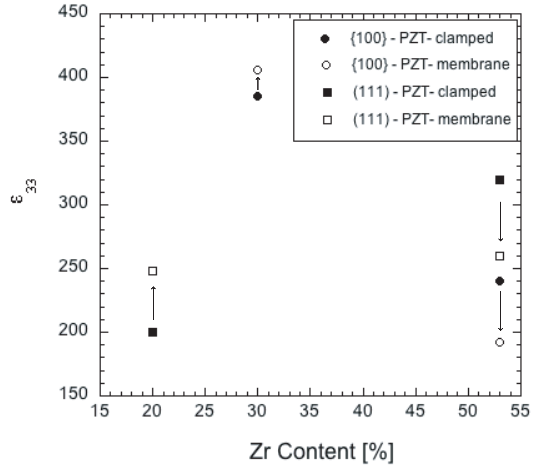

Figure 3.20: Dielectric constants from impedance data of unreleased device structures compared to data from resonating structures. The values of the films at the MPB were measured with an applied electric field of 7.5-10 kV/cm.

In order to compare the piezoelectric coefficient from TFBARs with the values from interferometric measurements, the piezoelectric constant $\mathrm{d}_{33,f}$ can be calculated using the materials parameters from the fit by the following equation:

$$d_{33,f} = \frac{e_{33}}{c_{33}^{D}(1-k_t^2)} \tag{3.10}$$

The values measured by interferometry are presented in Section 2.5 in Figure 3.21. It would be expected that the piezoelectric constant $\mathrm{d}_{33,f}$ is higher for the unclamped film than for the clamped film. This is the case for two of the four measurements shown in Figure 3.21, the other two show very similar values for clamped and unclamped films. The small change with frequency when comparing the interferometry measurements with the values derived from the impedance data analysis of resonators indicates that we mostly observe lattice (intrinsic) contributions with only a weak domain wall contribution. The maximum d_{33} value observed at around 110 pm/V is indeed close to the expected lattice contribution.

The model used allows for the determination of the stiffness constant of specific orientations of PZT grains. Values for stiffness and sound velocity can be found in literature. Values in this work range from 130 to 200 GPa which are slightly higher than values reported for bulk PZT (PZT4: $c_{33}^{D} = 150$ GPa, PZT 3203: $c_{33}^{D} = 177$ GPa [93]). As we applied a

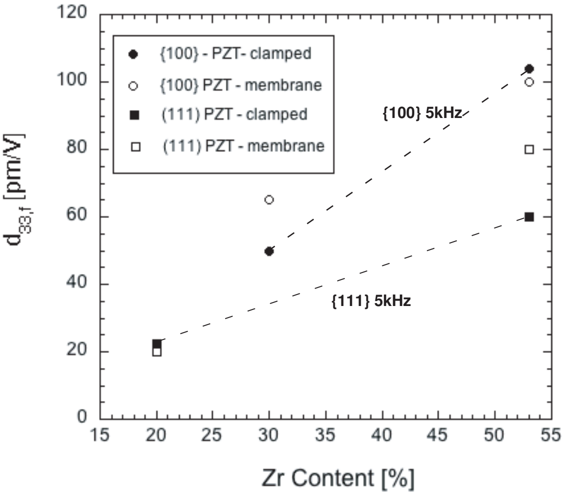

Figure 3.21: Piezoelectric constants $d_{33,f}$ from interferometry measurements compared to data derived from the impedance data analysis of resonators. The values of the films at the MPB were measured with an applied electric field of 7.5-10 kV/cm.

relatively high bias, leading to a reduction of domains and in addition we are dealing with a textured structure, the higher values can be explained by improved domain alignment as compared to ceramics. Larson *et al.* characterised PZT thin films and reported values for the sound velocity. Using the standard density of PZT (7750 kg/m^3) these values correspond to c_{33}^D values between 140 and 160 GPa, similar to bulk PZT. Values on PZT thick films have been reported by Lukacs *et al.* [94] who measured c_{33}^D values of 20-90 GPa on 15-75 μm thick sol-gel PZT films with random orientation. These low values may indicate that films are porous. These values are all at zero electric field, whereas some of the values presented in this work are at an applied field of 7.5 to 10 kV/cm. The influence of the electric field on sound velocity was studied for PZT ceramics by [95]. They study commercial soft PZT (APC 850) at frequencies of 22 MHz and found that for longitudinal waves the sound velocity decreases close to the coercive field.

Acoustical losses or attenuation $\tan\gamma$ have also been discussed for PZT ceramics at low frequencies [96]. They reported damping of 13 dB/mm at 100 MHz which translates into a damping coefficient of $\alpha = 2900$ /m. Extrapolation of this value to 800 MHz would give us a damping coefficient α of roughly 50'000 /m. When using this coefficient to estimate the quality factor at 800 MHz a quality factor Q of around 11 is obtained. This value shows that big losses can be expected in PZT at high frequencies, but this calculation is only a rough estimate and is based on values for ceramic PZT at low frequencies. In the same work, it was also shown that smaller grains lead to less losses.

Values of $\tan\gamma$ obtained in this work suggest that losses are higher for {100} textured films. This would be consistent with the explanation given in Section 2.3.1, suggesting (111) oriented films to have lower losses caused by domain vibrations. It can also be noted that losses are higher for films with a composition at the morphotropic phase boundary than for films with a tetragonal composition. In all cases a high coupling constant of film is accompanied by high losses and thus low Q-factors.

3.6 Summary

An overview of the coupling constants and Q-factors of the realised devices compared to devices reported in literature (as shown in Figure 1.3) is shown in Figure 3.22. A summary of all parameters used for fitting, parameters extracted from the models and parameters calculated using extracted data for all modelled devices are shown in Table 3.7. Material parameters for PZT thin films with compositions at the MPB or tetragonal compositions and textured in the (111) or {100} direction have been presented. It was observed that acoustic losses are higher for films at the MPB than for tetragonal films and higher for {100} textured films than (111) textured films. The mechanism of loss is attributed to domain wall vibrations in both of these cases. The acoustic losses and the coupling constants were found to be correlated, high coupling constants were accompanied by high losses and vice versa.

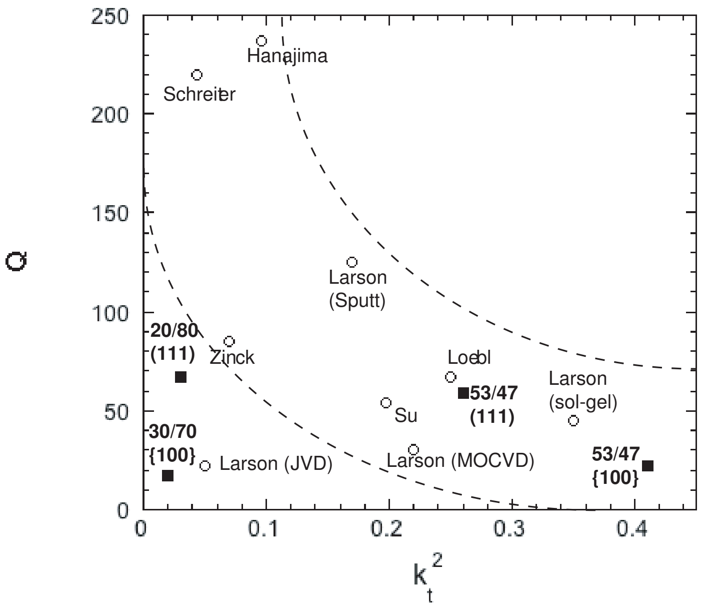

Figure 3.22: Overview of data for coupling constant k_t^2 vs. Q factor for PZT resonators realised in this work (filled squares) and for resonators reported in literature (open circles). Dotted lines indicated possible correlations between the two values.

	sol-gel 53/47 (111) (15V)	**sol-gel 53/47 {100}(20V)**	**sputt. 20/80 (111) (0V)**	**sol-gel 30/70 {100} (0V)**	**sol-gel 53/47 {100}(0V)**
common parameters					
L_s [nH]	0.1	0.01	0.1	0.1	0.01
R_s [Ω]	6	13	6	6	10
C_p [pF]	3.05	3.69	3.49	3.67	2.3
equivalent circuit parameters					
L [nH]	90	15	80	33	113
R [Ω]	8.2	6.0	10.8	10.5	90
C [pF]	0.48	1.30	0.16	0.60	1.55
C_0 [pF]	2	3.2	4.1	5.5	1.8
$\tan\delta$	0.01	0.01	0.02	0.02	0.01
f_r [GHz]	*0.766*	*1.14*	*1.406*	*1.13*	*0.38*
f_a [GHz]	*0.852*	*1.352*	*1.434*	*1.19*	*0.48*
Q	*52.8*	*18.0*	*65.5*	*22.3*	*3.3*
k_t^2	*0.24*	*0.41*	*0.039*	*0.11*	*0.86*
k_t^2*Q	*12.67*	*7.38*	*2.32*	*2.45*	*3.32*
material coefficients					
PZT thickness [μm]	2.1	1.0	1.0	1.1	
Pt thickness [μm]	0.1	0.15	0.1	0.1	
v_D [m/s]	4846	5389	4501	4097	
ε_{33}^S	260	192	248	406	
e_{33} [C/m^2]	10.0	12	3.1	7.5	
c_{33}^D [GPa]	180	225	157	130	
$\tan\gamma$	0.017	0.045	0.015	0.060	
$\tan\delta$	0.01	0.01	0.02	0.02	
$d_{33,f}$ [pm/V]	*79*	*100*	*20*	*65*	
Q	*59*	*22*	*67*	*17*	
k_t^2	*0.24*	*0.36*	*0.03*	*0.12*	
k_t^2*Q	*14.16*	*7.92*	*2.01*	*2.04*	

Table 3.7: Overview of parameters used to fit impedance data. Parameters in italic are derived values.

Chapter 4

Alternative materials and routes

The performances of the devices shown in the previous Chapter are not satisfactory. There are different approaches that could be followed in order to find higher Q-factors while keeping a high coupling constant. In this Chapter two approaches that have been initiated shall be described. The first approach is to study a uniaxial ferroelectric material, i.e. one in which only 180 ° domain boundaries exist. Since these can be removed by poling, acoustic losses in these films should be a lot smaller than for PZT. The material studied is potassium lithium niobate (KLN) deposited by pulsed laser deposition (PLD). The second approach is still using PZT as functional layer, but on a MgO substrate. As discussed in Chapter 2, the substrate has a great influence on the stress in the film and thus on the a/c domain ratio. The lattice parameters of MgO allow for highly c-axis oriented PZT thin films. In order to exploit this a process flow to fabricate TFBARs on MgO substrates was designed and first test structures were fabricated.

4.1 KLN

Complex ceramics with tungsten bronze structure are known for their superior pyroelectric, piezoelectric and optical properties [3]. $K_3Li_2Nb_5O_{15}$ (KLN) crystals have attracted great interest due to their desirable electro-optic and nonlinear optical properties and their high stability to intense laser irradiation [97]. The piezoelectric properties of KLN are also promising; the coupling coefficient k_t of 0.64 makes it an interesting candidate for piezoelectric transducer and resonator applications [98]. This section will start by introducing the structure and physical properties of potassium lithium niobate (KLN) single crystals and ceramics. The second part shall give a literature overview of fabrication and characterisation of KLN thin films. The next two sections describe the method used to fabricate the films followed by film characterisation.

4.1.1 KLN structure and properties

Tetragonal Tungsten Bronzes (TTB) can be described with the general chemical formula $[(A_1)_2(A_2)_4C_4][(B_1)_2(B_2)_8]O_{30}$. The structure consists of BO_6 octahedra (B = Nb, Ta, W...) connected at their corners. One elementary cell consists of 10 oxygen octahedra. The positions A_1, A_2, B_1, B_2 and C are shown in Figure 4.1. The crystal structure of KLN was first resolved by Abrahams *et al.* [99]. The point group is 4mm at room temperature. The phase transition from paraelectric to ferroelectric phase results in a transition from 4/mmm to 4mm. This is due to a unidirectional displacement of the niobium ions from the centre of their oxygen octahedra, resulting in a loss of the 1/m symmetry and the formation of a spontaneous polarisation along the *c*-axis.

In most TTB compounds the cation positions A and C are only partially occupied. Potassium lithium niobate and potassium lithium tantalate niobate solid solutions are the only known ferroelectric compounds with a filled structure. The chemical formula for KLN $K_6Li_4Nb_{10}O_{30}$ is only an ideal stoichiometric formula, which is thermodynamically not stable. Abrahams [99] *et al.* found the A_1 site occupied by 87% K and 13% Li, the A_2 site by 99% K and 1% Li and the C site by 94% Li and 6% Nb. The B sites are fully occupied by Nb. It is obvious that the Nb ions on C sites will lead to disturbance in the charge balance. The mechanism to equalise this charge is though to be creation of vacancies.

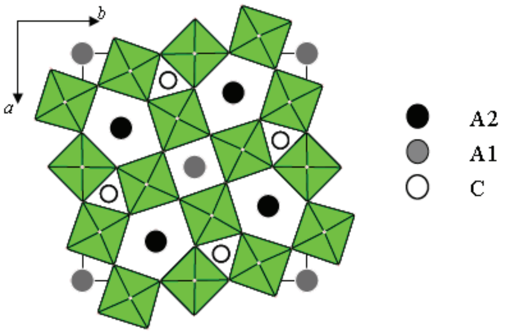

Figure 4.1: Crystallographic structure of potassium lithium niobate. The general chemical formula of the tungsten bronze structure is given by $[(A_1)_2(A_2)_4\ C_4][(B_1)_2(B_2)_8]O_{30}$. The crosses represent the NbO_6 octahedra.

The $K_2O - Li_2O - Nb_2O_5$ ternary system was first studied by Scott [100] and Ikeda [101] in 1970. They both excluded the existence of stoichiometric $K_6Li_4Nb_{10}O_{30}$ and define the location of the tungsten bronze field as shown in Figure 4.2. It can be seen that the KLN phase is present along the 30% K_2O isopleth in the area of 51 mole % to 68 mole % Nb_2O_5. The composition $K_6Li_4Nb_{10}O_{30}$ is slightly outside of this area and thus not stable. The solid solution $K_{6-x-y}Li_{4+x}Nb_{10+y}O_{30}$ exists only when the Nb_2O_5 proportion is bigger than 51 mole %. Above 55 mole % Nb KLN remains paraelectric down to room temperature. The paraelectric to ferroelectric phase transition for compositions between 51 mole % and 55 mole % Nb has been shown to vary from 400 °C to 500 °C [100] .

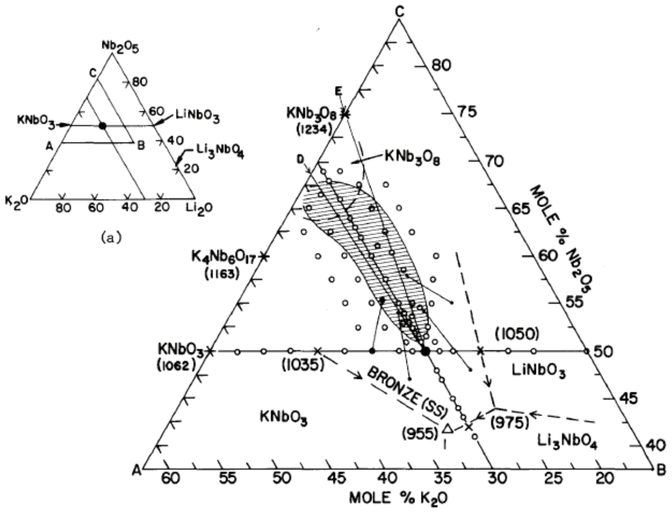

Figure 4.2: a) K_2O-Li_2O-Nb_2O_5 ternary system, b) The reduced phase diagram ABC showing the tungsten bronze field (hatched area, after Scott [100]).

Properties of single crystals and ceramics have been reported by various authors. Properties of interest for this work shall be briefly summarised. Uematsu *et al.* [98] studied the piezoelectric properties of single crystal KLN. They obtained crystals with single domain structure by poling. By measuring this crystal, cut in order to measure the purely longitudinal mode, they obtain an electromechanical coupling factor of $k_t = 0.64$. Adachi *et al.* [97] gave a more detailed study also of KLN single crystals reporting values for coupling constant $k_{33} = 0.52$, dielectric constants $\varepsilon_{11} = 306$ and $\varepsilon_{33} = 115$ and piezoelectric constant $d_{33} = 57$ pm/V and many other piezoelectric and elastic constants. Neurgaonkar *et al.* did similar experiments finding: $k_{33} = 0.52$, $\varepsilon_{33} = 120$, $d_{33} = 57$ pm/V, confirming the results of Adachi *et al.* [97].

Dielectric characteristics of polycrystalline KLN were studied by Xu *et al.* [102]. They study the effect of the Nb_2O_5 content on dielectric characteristics of KLN, the Nb_2O_5 content ranging from 50 to 56 mole %. The dielectric constants at 200 °C range from 110 to 410 with increasing Nb content. The expected phase transition from ferroelectric to paraelectric was not observed when measuring the dielectric constant versus temperature. They assume this is due to evaporation of Li and/or K which leads to a higher effective Nb content above 55 mole % meaning the composition is paraelectric. They add titanium in order to suppress evaporation of potassium and lithium and observe the structure to be more stable. The dielectric relaxation at the phase transition temperature is observed in samples containing Ti.

4.1.2 Literature review of KLN thin film synthesis

Ferroelectric single crystal thin films attract a great deal of attention for optical device applications. The interest in KLN came due to its high stability to intense laser radiation, its good electro-optic and nonlinear optic properties. The first reports of KLN thin films in the early 1980's were studies of epitaxial single crystal KLN on $K_2BiNb_5O_{15}$ and sapphire substrates for optical waveguide applications [103, 104]. They obtained epitaxial KLN (001) films on both substrates by sputtering of a ceramic target with a potassium and lithium enriched composition. The measurements done on these films include refractive index, optical propagation losses and surface acoustic wave (SAW) properties. The same group reported similar work in the early 1990's using the same technique on sapphire but also on fused silica and metal substrates, all showing highly (001) oriented KLN [105]. Another group, also interested in waveguiding applications reported fabrication of KLN films by metalorganic chemical vapour deposition (MOCVD) on potassium lithium tantalate substrates [106]. Park *et al.* were the first to report the fabrication of KLN thin films on platinised silicon substrates [107, 108]. For this work the sputtering technique with a ceramic target containing potassium and lithium excess was applied. They obtain a mixture of (001) and (311) orientations and explain the (311) peak as probably due to underlying (111) oriented platinum, since it is not present on films deposited on glass substrates [109]. They explore different sputtering pressures and characterise the morphology of the films by SEM. Optical properties of KLN films were further studied using sol-gel techniques on various substrates such as MgO [110,111] and SiO_2/Si [112,113]. The only report of sol-gel KLN on platinised silicon was in in the work of Ono *et al.*. They found the films showed no preferential orientation on platinised substrates and a $LiNbO_3$ second phase was observed using XRD. They report values for the dielectric constant ε_f = 136 and loss tangent tanδ = 0.026 measured at 1 kHz. This value is the first value of a dielectric constant reported for KLN thin films. The reported value of 136 is close to the ε_{33} value of 115 for a single crystal and is too low for a randomly oriented film. This low value can be explained easily when taking into account that second phases of $LiNbO_3$ are present, $LiNbO_3$ single crystal values for the dielectric constant are $\varepsilon_{11} = 85$ and $\varepsilon_{33} = 28$ [114], lower than for KLN. Another reason explaining the low dielectric constant could be porosities present in the films.

PLD of KLN thin films was first reported in 2007 by Zhan *et al.* [115]. They use a stoichiometric target and deposited on quartz glass substrates. The films obtained are (310) oriented films and show good optical properties. One more recent report studies the influence of oxygen pressure on the structural, morphological and optical properties of KLN deposited by PLD [116]. The films are deposited on glass substrates using a stoichiometric ceramic target. The authors concluded that a low oxygen pressure during deposition improves crystallinity of the films, and with increasing oxygen pressure the rms surface roughness and the grain size of the films decrease.

4.1.3 KLN thin film deposition by PLD

Thin films have been deposited starting from $K_3Li_2Nb_5O_{15}$ ceramic targets with an excess of potassium and lithium. The target was prepared by sintering the high purity chemicals K_2CO_3 (99.99%), Li_2CO_3 (99.99%) and Nb_2O_5 (99.9%) in air at 900 °C for 4 h to obtain stoichiometric KLN powder [102, 117] . An excess of 100% potassium and 50% lithium were added by adding K_2CO_3, Li_2CO_3 and discs were prepared. The discs were fired at 800 °C for 3 h to obtain mechanical stability. Targets with a diameter of 2 cm were obtained. The target was ablated using a KrF excimer laser (Lambda Physik, $\lambda = 248nm$) with pulse duration of 25 ns and total energy 300 mJ. The pulsed laser energy density was 1850 mJ/cm^2 and the repetition rate 5 Hz. The substrate of Si with a $Ti/TiO_2/Pt$ (10 nm / 40 nm / 100 nm) sputtered electrode was situated at a distance of 4 cm from the target. The base pressure in the chamber was $1 \cdot 10^{-5}$ mbar. For film deposition the oxygen pressure was varied from $2 \cdot 10^{-2}$ mbar to $2 \cdot 10^{-1}$ mbar and substrate temperature from 600 to 700 °C to find optimal deposition conditions. Deposition time was from 30 min to 1 h followed by slow cooling to room temperature in an oxygen atmosphere. A summary of deposition conditions is given in Table 4.1.

Target compositions with 100% potassium excess and 50%-75% lithium excess were found to produce KLN films with a tungsten bronze phase. Previous experiments with a stoichiometric target and a target with 100% lithium excess showed second phases. High oxygen pressures (0.1 mbar) and high temperatures (680 to 700 °C) were observed to decrease second phases. However pure tungsten bronze films could not be achieved using stoichiometric targets. The thickness of the films varied greatly with the deposition conditions (pressure, temperature), in the range of 10-30 nm/min. The target with 100% K and 50%

Table 4.1: General deposition parameters used in this work

laser wavelength	248 nm
laser energy	200 mJ
laser flow	1850 mJ/cm^2
laser pulse duration	20 ns
laser repetition rate	5 Hz
substrate to target distance	4 cm
base pressure	$1 \cdot 10^{-5}$ mbar
oxygen pressure	$2 \cdot 10^{-2}$ to $2 \cdot 10^{-1}$ mbar
substrate temperature	600 to 700 °C

Li and also the target with 100% K and 75% Li excess were found to give films with a pure tungsten bronze phase at 700 °C and 0.1 mbar.

4.1.4 KLN thin film characterisation

The structure and morphology of the films were analysed by XRD $\theta - 2\theta$ measurement and scanning electron microscopy. Capacitance measurements were performed using an impedance meter to characterise the dielectric properties of the films. The piezoelectric properties were measured using a double beam laser interferometer as described in reference [39].

X-ray diffraction

Figure 4.3 compares two XRD $\theta - 2\theta$ measurements of KLN film deposited with two different targets. The film with the diffraction pattern shown in Figure 4.3a was grown using a KLN target with 50% excess Li and 100% excess K. The target used to make the film with the diffraction pattern shown in Figure 4.3b contained 75% Li excess and 100% K. Other conditions were the same. Both films have a preferred (001) orientation. The peak at $2\theta = 31.6°$ can be identified as the (311) orientation, the peak $2\theta = 36.9°$ could correspond to the (411) orientation of KLN [118]. The peak $2\theta = 42.8°$ corresponds to the (511) orientation, but could also correspond to the (202) peak of a lithium niobate secondary phase ($LiNbO_3$) [118, 119]. The preferred (001) orientation of KLN films has previously been reported for sputtered films [105, 108], in [108] the KLN films were deposited on a Pt/Ti/SiO_2/Si substrate and the (311) peak was also observed, but no other orientations. Since the (311) peak is the most intense peak of the KLN powder of JCPDS

(Joint Committee on Powder Diffraction Standards) [118] these films are still well oriented in the (001) direction, the film show in Figure 4.3a having a preferred orientation of 97%, the film in Figure 4.3b 80%, assuming the peak at $2\theta = 42.8°$ is KLN.

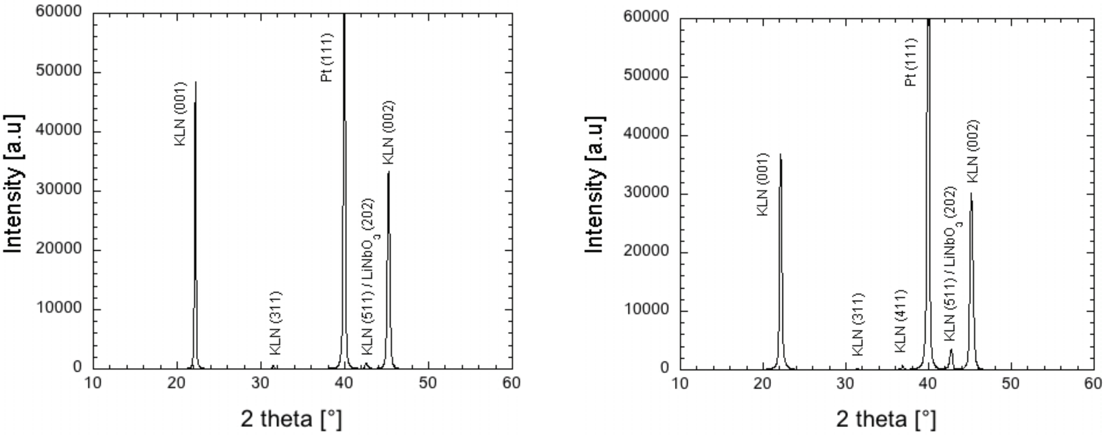

(a) (b)

Figure 4.3: (a) X-ray diffraction scan of a KLN film deposited by PLD of a 100% K and 50% Li excessed target, (b) X-ray diffraction scan of a KLN film deposited by PLD of a 100% K and 75% Li excessed target.

Scanning electron microscopy (SEM) observations

SEM images reveal a columnar structure with a very fine grains of about 50 nm diameter (Figure 4.4). The thickness of the films shown in Figure 4.4 is about 400 nm, which means that the deposition rate is approximately 10 nm/min (deposition time 30 min). The fourfold symmetry of the grains can be recognised when looking at the films from the top as shown in Figure 4.5.

Dielectric measurements

Figure 4.6 presents the frequency dependence of the dielectric constant of a 400 nm thick KLN film made using the 100% K and 50% Li excessed target. The value of the dielectric constant at 1 kHz is around 250 and the dielectric losses around 2-3%. The reported values for the dielectric constant of stoichiometric single crystal KLN are $\varepsilon_{33} = 115$ and $\varepsilon_{11} = 306$. Since the film is well textured a lower dielectric constant is expected. An explanation for the high dielectric constant could be a composition poor in lithium and rich in niobium.

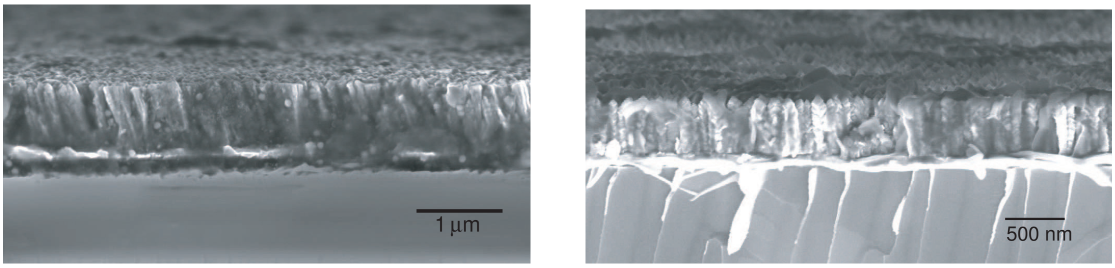

(a) (b)

Figure 4.4: (a) SEM cross-section of a KLN film deposited by PLD of a 100% K and 50% Li excessed target, (b) SEM cross-section of a KLN film deposited by PLD of a 100% K and 75% Li excessed target.

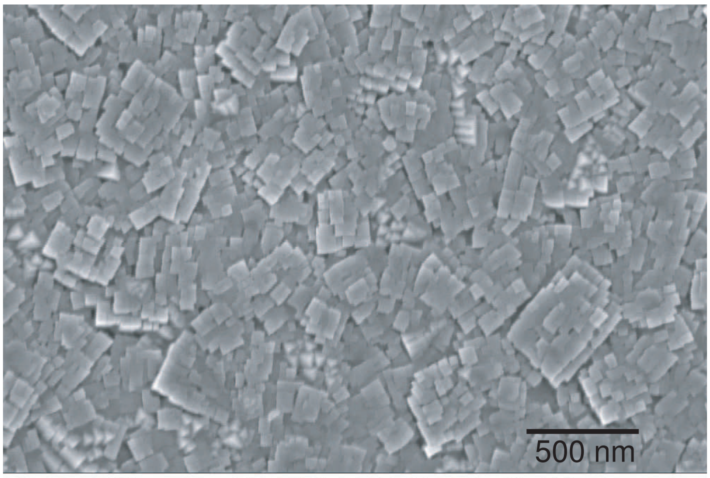

Figure 4.5: SEM top view of a KLN film deposited by PLD. Four-fold symmetry of the grains is observed.

The KLN ternary phase diagram shows a tungsten bronze field for compositions with about 30 mole % K_2O and Nb_2O_5 varying between 51 mole % and 68 mole %. Therefore intermediate compositions can have a stable tungsten bronze structure with properties differing from the near stoichiometric composition. The work of Xu *et al.* [102] studied the effect of the Nb_2O_5 content on dielectric characteristics of KLN ceramics with the Nb_2O_5 content ranging from 50 to 56 mole % and found higher dielectric constants for compositions rich in Nb. The composition of the films in this work should be analysed in order to confirm this explanation for a slightly high dielectric constant.

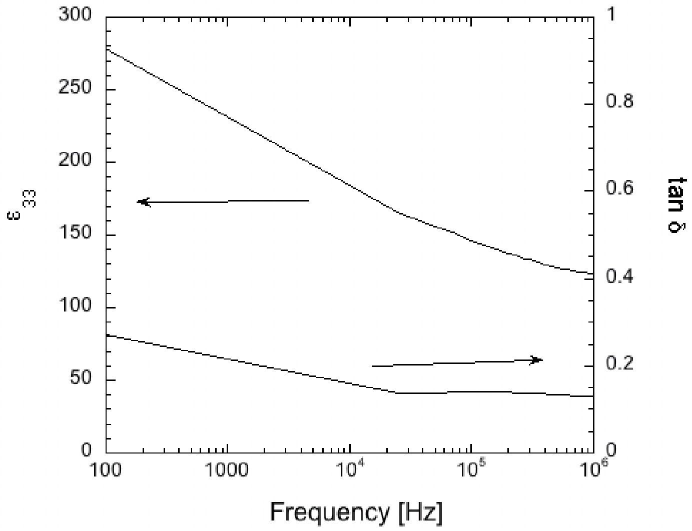

Figure 4.6: Frequency dependence of the dielectric constant of a 400 nm thick KLN film made using the 100% K and 50% Li excessed target.

Piezoelectric measurements

The 400 nm thick KLN film made using the 100% K and 50% Li excessed target characterised above was used to measure the piezoelectric coefficient $d_{33,f}$ using a double beam laser interferometer setup as described in Section 2.5. The piezoelectric constant $\mathrm{d}_{33,f}$ was measured using an AC voltage of 0.1 V at 5 kHz. The field dependency shown in Figure 4.7 was measured by applying a superimposed DC voltage up to 3 kV/cm.

Piezoresponse force microscopy (PFM) was used to image the local piezoelectric activity of the KLN thin film on a nanometer scale. In PFM, a local electric field is generated by applying an AC voltage to a conducting tip in contact with a sample, and the deformation due to the piezoelectric effect is detected [120]. An AC voltage of 1 V at 5.3 kHz was used to measure an area of 3 x 3 μm on a KLN film with a thickness of 400 nm made using the 100% K and 50% Li excessed target. Figure 4.8a shows the topography of this film. The area was then poled with -3V applied to the AFM tip. The remanent piezoelectric activity was measured after the removal of the DC bias, shown in (b) as an amplitude signal and in (d) as phase signal. A subsequent poling treatment with +3V reduced the piezoelectric activity of some of the grains, but switching of the polarisation was hardly observed (see Figures 4.8c and 4.8e).

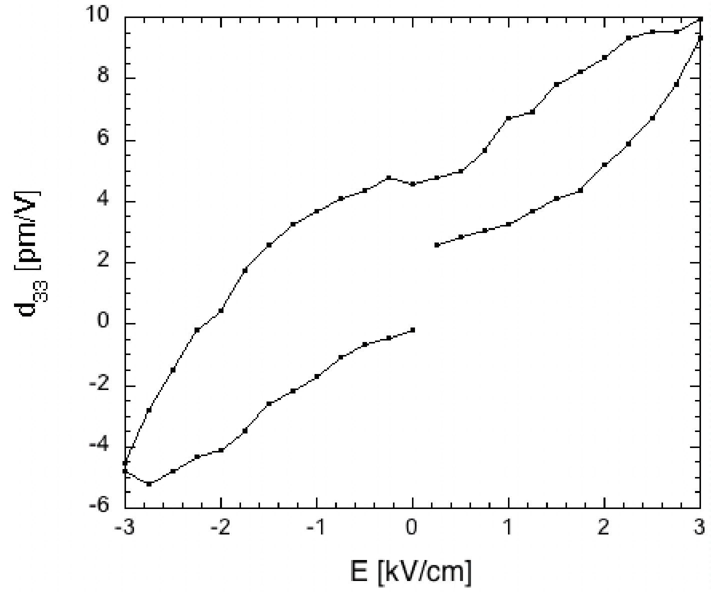

Figure 4.7: Field dependence of the piezoelectric constant $d_{33,f}$ of a 400 nm thick KLN film made using the 100% K and 50% Li excessed target measured by laser interferometry.

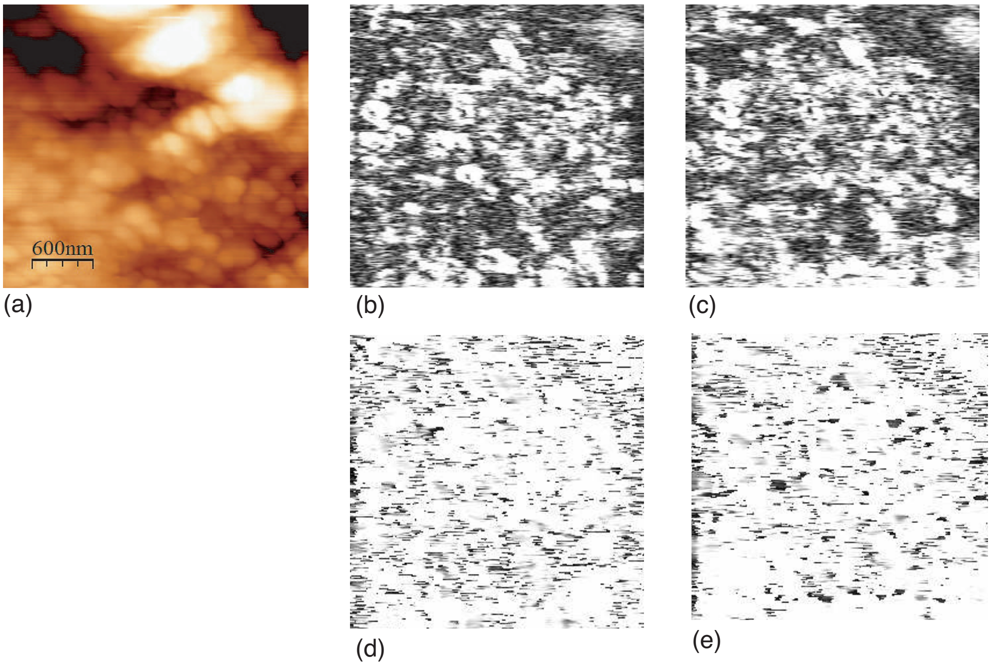

(a) (b) (c) (d) (e)

Figure 4.8: AFM measurements (3 x 3 μm) on a 400 nm thick KLN film made using the 100% K and 50% Li excessed target. (a) Topography, (b) Amplitude signal of piezoresponse after poling with an applied voltage of -3 V, (d) corresponding phase signal, (c) Amplitude signal of piezoresponse after poling with an applied voltage +3 V, (e) corresponding phase signal.

4.1.5 Summary

$K_6Li_4Nb_{10}O_{30}$ (KLN) films with a tungsten bronze structure have been deposited on $Pt/TiO_2/Ti/Si$ substrates by pulsed laser deposition. The films were deposited at 700 °C and 0.1 mbar in an oxygen atmosphere. The films were characterised by XRD, SEM and capacitance measurements. A tungsten bronze structure was observed by XRD and SEM revealed small columnar grains. The dielectric constant is around 250 at 1 kHz; reported values of the dielectric constant for single crystal KLN with a stoichiometric composition are $\varepsilon_{33} = 115$ and $\varepsilon_{11} = 306$. A possible explanation for the high dielectric coefficient could be that the composition is not stoichiometric but lithium deficient. To measure acoustic properties in this material a bulk acoustic wave resonator structure should be fabricated.

4.2 PZT on MgO

Ideally the PZT for a TFBAR should be a c-axis oriented single crystal, single domain thin film. One way to get closest to this state is to grow the PZT film on MgO substrates. This section will start with a description of the state of the art of PZT films grown on platinised MgO substrates, followed by the process flow in order to get a TFBAR structure. Section 4.2.3 shall describe films grown on MgO substrates for this study and also the first attempts to create a TFBAR structure on MgO.

4.2.1 Growth issues

Epitaxial film growth of ferroelectric materials is of great importance since it allows for alignment of the polar axis, elimination of grain boundaries and reduction of domain wall density. The use of dissimilar substrates induces elastic strains associated with the mismatch in lattice constants and the thermal expansion coefficients between film and substrates. In addition strain is induced if a phase transformation takes place during the cooling process of the films after deposition. The studies of PZT films on MgO summarised in this section mainly explore properties of *c*-axis oriented films or the stress behaviour of these films.

$PbTiO_3$ thin films with *c*-axis orientation were first reported by Iijima et al. in 1986 [121]. The films were obtained by sputtering at a low deposition rate on (100) MgO substrates and reported to have good pyroelectric, dielectric and piezoelectric properties. The platinum was grown at 600 °C and was (100) oriented. PZT films on MgO were reported by the same group three years later [122]. Again a (100) MgO substrate with a (100) oriented Pt film was used and ceramic targets with 8 different $Pb(Zr_x\ Ti_{1-x})O_3$ compositions with x = 0.2 - 0.8 were employed to sputter deposit the PZT films. They found the tetragonal films had a strong (001) orientation whereas the rhombohedral ones were (100) oriented. The dielectric, ferroelectric and pyroelectric properties of these films were also studied. MOCVD deposited PZT films on MgO were reported by Sakashita *et al.* (1991) [123] who found that the *c*-axis oriented films with compositions close to the morphotropic phase boundary had dielectric constants around 200 - 300.

In 1992 Tuttle *et al.* [62] use sol-gel PZT on MgO and silicon substrates in order to study stress effects on the properties as previously described in Section 2.3.2. They state that the films with a high degree of *c*-axis orientation had higher polarisation and lower dielectric constants than films with *a*-axis orientation.

From the early 1990's until the present many reports on PZT films on MgO deposited by various methods were published. A summary of principle conditions and results on PZT deposited on (100) MgO substrates is shown in Table 4.2. In general it was found that c-axis oriented films showed low dielectric constants and high piezoelectric constants. Microstructurisation of the MgO was used in some of these studies [124–126] to create cantilever structures for the measurement of piezoelectric constants. The MgO beneath the beams was etched out using a hot H_3PO_4 solution in all of these studies.

One study of a TFBAR fabricated on a MgO substrate has been published to date. The study by Yamauchi *et al.* [127] reports of devices based on single *c*-domain Pb(Mn, Nb)O_3 - Pb(Zr, Ti)O_3 on (001) MgO substrates. They found a maximum electromechanical coupling coefficient of 0.7 and a Q-factor of 185 at a resonance frequency of 4 GHz using this film. The bottom electrode used to fabricate this structure is based on $SrRuO_3$/Pt and the top electrode was aluminium. The MgO substrate was removed from the back side by chemical etching. This study shows that both high coupling and high quality factors can be obtained using PZT based materials in TFBARs.

4.2.2 TFBAR fabrication

As stated in the previous section microfabricated cantilevers can be obtained by wet etching of the MgO substrate. The fabrication of a membrane structure on MgO substrates has also been reported by Kotani *et al.* [135]. They fabricated infrared sensors by surface micromachining of La-modified $PbTiO_3$ on platinised MgO substrates. They use etching holes at two sides of the membrane to allow access to the MgO substrate for chemical etching.

Based on this approach a process flow for a surface micromachined double resonator TFBAR structure was developed. A schematic of the design used to obtain this structure is shown in Figure 4.9. A summary of the process flow is shown in Figure 4.10. The substrates used were single side polished, single crystal (100) oriented MgO substrates with dimensions of 10 mm x 10 mm x 0.5 mm. A 100 nm thick platinum bottom electrode was deposited using a magnetron sputtering system (Nordiko 2000) at 600 °C. The bottom electrode was patterned by dry etching using a photoresist mask. The etching is done using chlorine chemistry in a dry etcher (STS multiplex ICP). The PZT was deposited onto the bottom electrode either by sputtering ($Pb(Zr_{0.20}, Ti_{0.80})O_3$) or by sol-gel ($Pb(Zr_{0.30}, Ti_{0.70})O_3$) as described in Chapter 2. Standard conditions were used to fabricate {100} oriented films. Both for sol-gel and for sputter deposited films a $PbTiO_3$ seed layer was used. A photolithographic lift-off process was used to pattern the top electrode. The top electrode was a 100 nm thick Pt film deposited either by sputtering at room temperature

(Nordiko) or by evaporation using an E-beam evaporator. Another photolithography was then performed in order to define the etching holes in the PZT film. The PZT was dry etched using fluorine chemistry (Alcatel AMS 200 DSE). The last step was the wet etching of the MgO substrate using 10 vol.% H_3PO_4 solution at 80 °C.

4.2.3 PZT and TFBAR characterisation

Sputtered $Pb(Zr_{0.20}, Ti_{0.80})O_3$ and sol-gel deposited $Pb(Zr_{0.30}, Ti_{0.70})O_3$ both with a thickness of 1 μm were grown on (100) oriented Pt on MgO substrates. The films were characterised by XRD $\theta-2\theta$ measurement. XRD scans of a sputtered and a sol-gel film deposited on platinised MgO are shown in Figure 4.11. Both films have a high c-axis orientation.

Before the wet etching of the MgO, the impedance of the devices were measured from 0.5 MHz to 2 GHz in order to extract the dielectric constant. The dielectric constant derived from these measurements was found to be 170 for the sputtered $Pb(Zr_{0.20}, Ti_{0.80})O_3$ film and 200 for the sol-gel deposited $Pb(Zr_{0.30}, Ti_{0.70})O_3$.

The critical step in the process flow to fabricate surface micromachined TFBARs on MgO as described in the previous section is the wet etching of MgO in order to liberate the membrane. The MgO beneath the top electrode contacts was etched away before complete liberation of the membrane. Completely liberated membranes could not be measured using this design. Figure 4.12 showing optical microscopy images and Figure 4.13 showing SEM images illustrate encountered problems. The impedance data of a device with a partially released membrane is shown in Figure 4.14 with the corresponding parameters shown in Table 4.3. The PZT film is a sol-gel deposited $Pb(Zr_{0.30}, Ti_{0.70})O_3$ and a voltage of 30 kV/cm were applied during this measurement.

Etching issues

In order to understand the encountered problems during etching a FIB cut through the middle of the device was performed. This cut should reveal how much of the substrate under the bottom electrode has been etched. Figure 4.15 shows a SEM image of a FIB cross-section of the device, cut in-between the two resonators of the double resonator structure. The bottom electrode of the device shown in Figure 4.15 is slightly displaced, meaning that the etchinghole was closer to the bottom electrode on the right side than on the left side. Figure 4.16 shows a zoomed-in detail of the left side of the same FIB cut. From this image it looks like the etching of the MgO substrate is inhibited when reaching the Pt bottom electrode.

Kotani *et al.* [135] used a similar processflow to fabricate infrared sensors based on La-modified PT (PLT). They observed an increase of the etching rate with increasing Pt deposition temperature. They assume that the diffusion of Pt into the MgO substrate is responsible for the increased etching rate, either because the Pt atoms act as catalysts during MgO etching or because of an increased number of defects due to Pt diffusion. They report the microcavity having a lozenge shape due to anisotropic etching of the (100) MgO substrate and state the yield of the microcavity production to be 99%. In this work the etching rate of the MgO covered by PZT was 2 μm/min, comparable to the etching rate reported in Ref. [135] of 3.3 μm/min. However the etching rate of the MgO beneath the bottom electrode was only around 0.1 μm/min. Previous reports of etching MgO covered by Pt/PZT (see Ref. [124–126]) do not mention low etching rates or any other difficulties. None of the publications mention if their H_3PO_4 solution was stirred during the etch process. Since in this work a droplet of the solution was placed on the sample surface, the solution could not be stirred. According to Sangwal [136] a stagnant solution results in isotropic etching with lower etch-rates.

The most likely reason explaining etching difficulties in this work seems to be a diffusion process impeding the etching of MgO. No literature could be found describing this phenomena. In order to study the etching of this structure, a process flow where stirring of the solution is possible should be tested. Another solution would be to try different electrodes or a diffusion barrier.

4.2.4 Summary

High *c*-axis oriented PZT films on MgO single crystal substrates have been fabricated. A process flow for TFBAR fabrication on MgO substrates was developed and tested. A small etch rate of the MgO underneath the bottom electrode inhibited the liberation of the membrane. The test structure was measured on the partially released structure and a coupling constant k_t^2 of 23% and a Q-factor of 2.7 were obtained. Since the wave is not reflected the energy is lost in the substrate and the resulting Q-factor is low. The coupling constant should also be higher for the released structure. Approaches to get around the etching difficulties have been proposed.

Author	**Year**	**Deposition technique**	**Deposition T [°C] Pt/PZT**	**Pt orientation**	**PZT orientation**	**Principle properties**	**Ref.**
Takayama	1988	sputtering	600/550-650	(100)	(001) for tetr. (100) for rhomb. PZT	good pyroelectric, dielectric and ferroelectric properties	[122]
Sakashita	1991	MOCVD	400/600-650	(100)	(001)	low dielectric constants	[123]
Tuttle	1992	sol-gel	600/650	(100)	(001)	high polarisation low dielectric constants	[62]
Kanno	1997	sputtering	n.s./500	(100)	(001)	microfabrication of cantilever d_{31} = -100 pm/V	[124]
Fujii	1997	sputtering	600/620-700	(100)	(001)	microfabrication of cantilever d_{31} = -100 pm/V	[125]
Okino	1999	MOCVD	RT/550	-	(001)	thickness/stress dependence of properties	[128]
Hong	2001	MOCVD	600/450	(100) (111)	epitaxial (001) oriented (001)	comparison of epitaxial and *c*-axis oriented films	[129]
Kwak	2003	sol-gel	n.s./650	(100)	(001)	microwave dielectric properties	[130]
Brennecka	2004	sol-gel	600/650	(100)	(001)	d_{31} = -51 pm/V	[131]
Kanno	2004	sputtering	n.s./550	(100)	epitaxial (001)	thermodynamic study	[126]
Kobune	2005	HIP	600/700	(100)	(001)	$PbTiO_3$ seed	[132]
Desfeux	2005	sputtering	500/500	(100)	(001)	AFM - local switching properties	[133]
Terada	2007	sputtering	600/600	(100)	epitaxial (001)	transfer to glass substrate	[134]

Table 4.2: Overview of literature on PZT deposited on platinised MgO substrates with a (100) orientation. (n.s. = not specified)

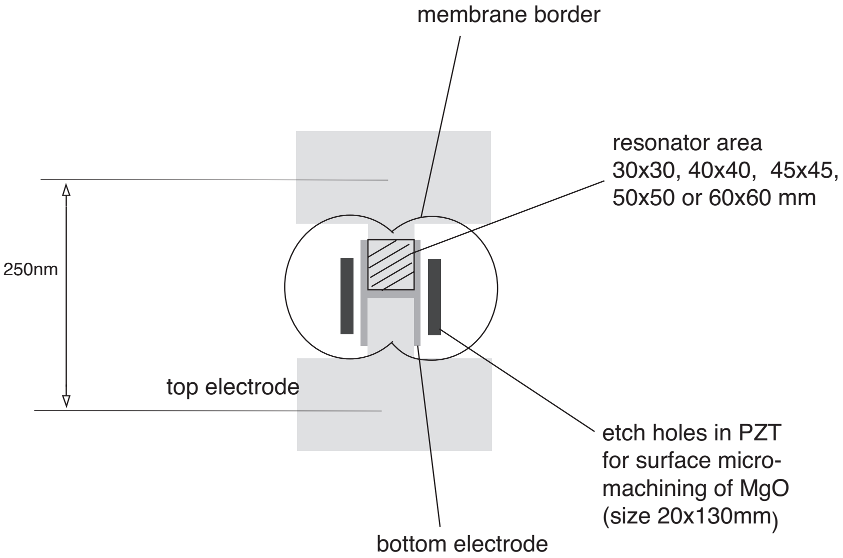

Figure 4.9: Schematic top view of a TFBAR with double resonator membrane structure. Etching holes allow for wet etching of the MgO in order to liberate the membrane.

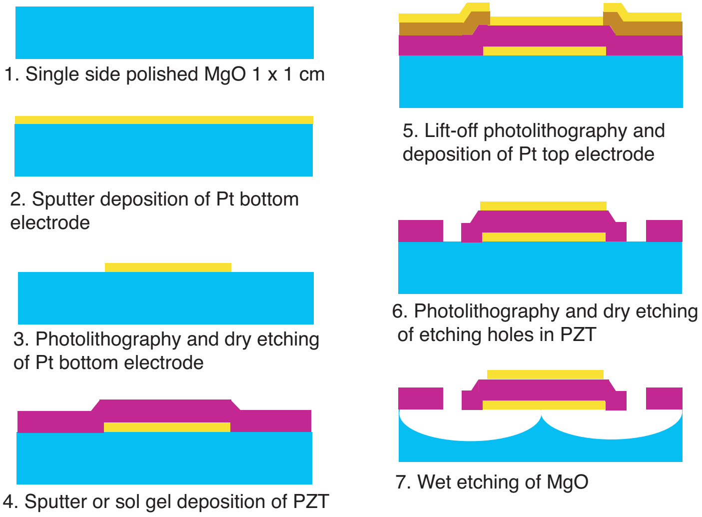

Figure 4.10: Process flow showing the steps to realise a TFBAR with double resonator membrane structure on MgO substrate.

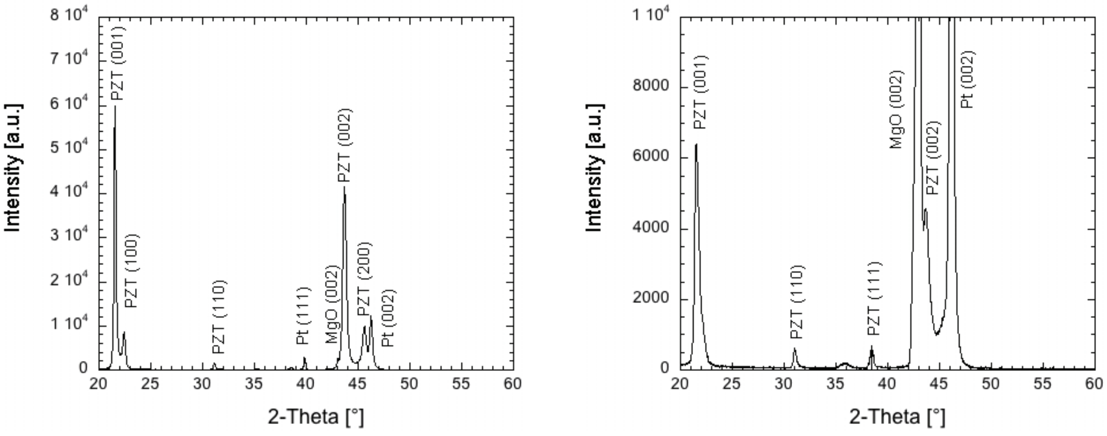

(a) (b)

Figure 4.11: (a) X-ray diffraction scan of a sputtered Pb($Zr_{0.20}$, $Ti_{0.80}$)O_3 film on Pt/MgO, (b) X-ray diffraction scan of a sol-gel deposited Pb($Zr_{0.30}$, $Ti_{0.70}$)O_3 film on Pt/MgO.

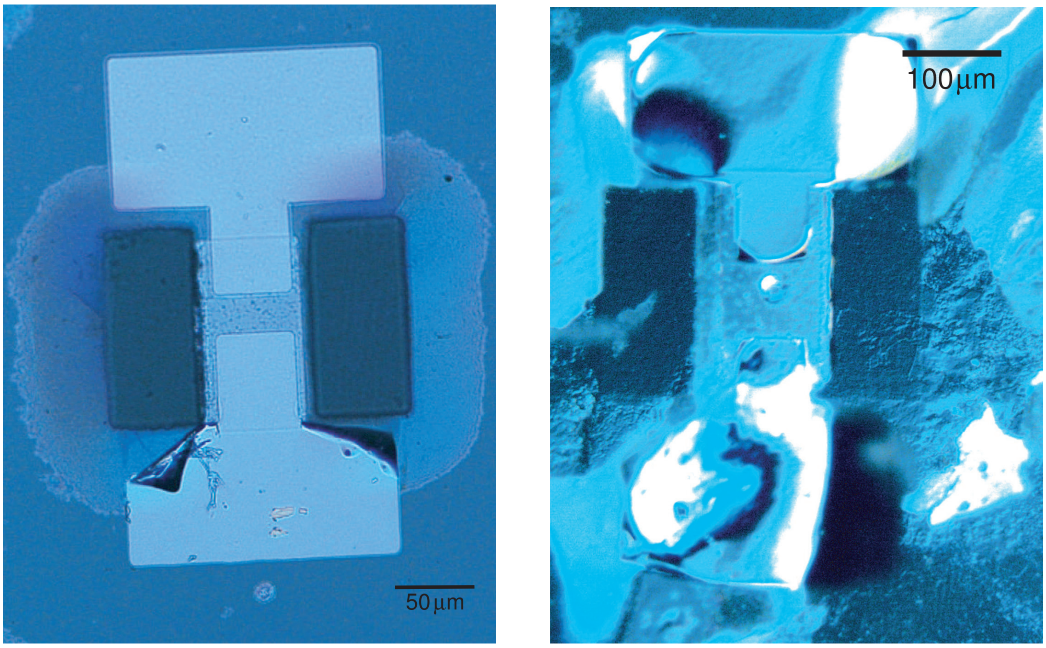

(a) (b)

Figure 4.12: Optical microscopy of a of a TFBAR double resonator structure based on Pt/PZT/Pt/MgO, (a) the membrane is probably not completely liberated, (b) the structure has been overetched.

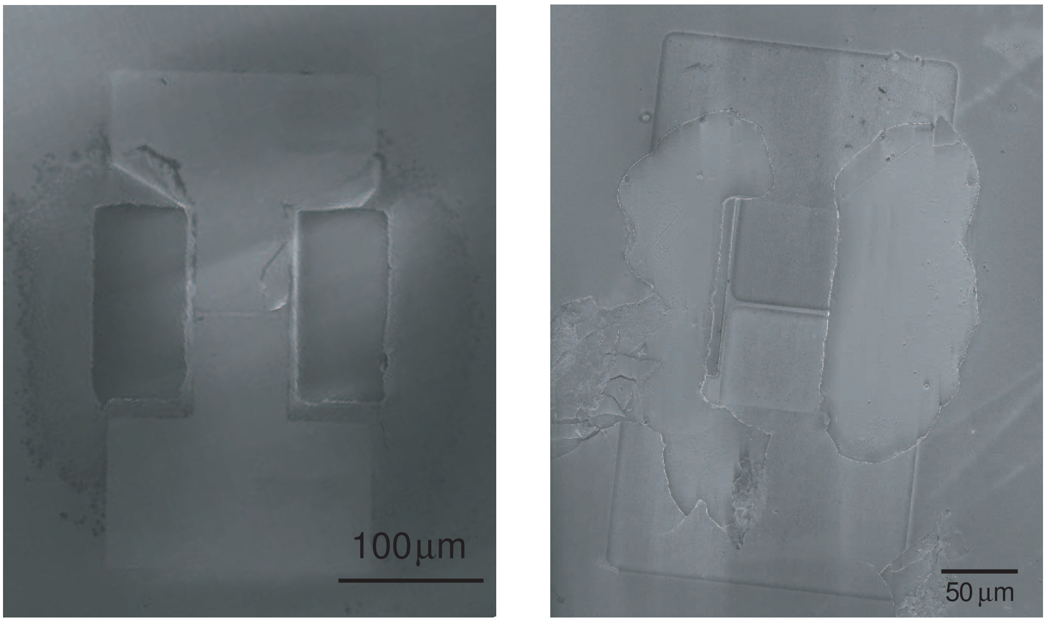

(a) (b)

Figure 4.13: SEM of a TFBAR double resonator structure based on Pt/PZT/Pt/MgO, (a) the membrane is probably not completely liberated, (b) the structure has been overetched.

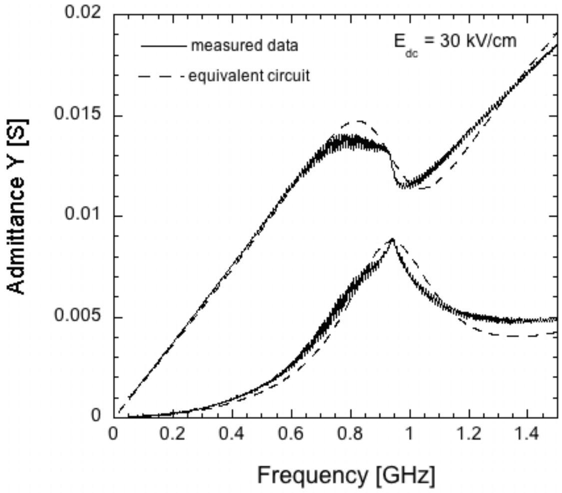

Figure 4.14: Frequency response of a TFBAR based on a 1 μm thick sol-gel 30/70 PZT film on MgO shown as real and imaginary part of the admittance characteristics. Simulated curves are plotted as dotted lines.

common parameters	
L_S [nH]	146
R_s [Ω]	330
C_p [pF]	0.13
equivalent circuit parameters	
L[nH]	58
R [Ω]	130
C[pF]	0.48
C_0 [pF]	2.05
$\tan\delta$	0.01
f_r [GHz]	0.95
f_a [GHz]	1.06
Q	2.7
k_t^2	0.23
$k_t^2 {*}Q$	0.62

Table 4.3: Parameters from equivalent circuit model used to simulate resonance of a 1 μm thick sol-gel 30/70 PZT TFBAR on at a field of 30 V.

Figure 4.15: SEM image of a FIB cross-section of the double resonator structure on MgO. The resonator was cut in-between the two resonators of the double resonator structure.

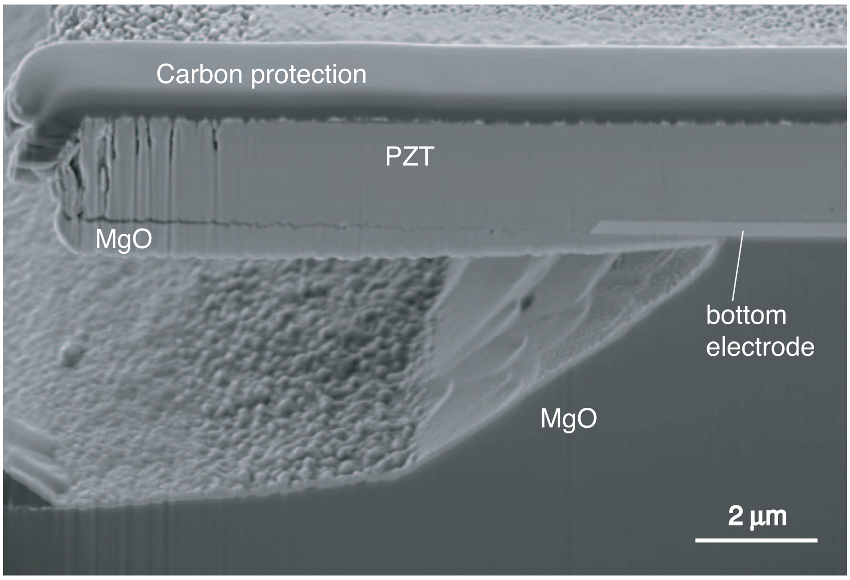

Figure 4.16: SEM image of a FIB cross-section showing a zoomed-in detail of the double resonator structure on MgO. The etching of the MgO substrate stopped when reaching the Pt bottom electrode.

Chapter 5

Conclusions and Outlook

5.1 Conclusions

In this thesis ferroelectric materials known to have a high electromechanical coupling constant have been studied for bulk acoustic wave resonator applications. The Pb(Zr_x,Ti_{1-x})O_3 (PZT) solid solution system is the main candidate, since it is known for its large piezoelectric constants and its growth is already well studied. As a main test vehicle, free standing thin film bulk acoustic resonator (TFBAR) structures with Pt/PZT/Pt/SiO_2 membranes were successfully fabricated based on silicon micro-machining techniques. The main outcome of the TFBAR characterisation can be summarised as follows:

- Thicker films tend to exhibit higher coupling constants: A k_t^2 of 0.8 was found for a 3.8 μm thick sol-gel PZT 53/47 {100} resonating at 400 MHz, as compared to k_t^2=0.4 for a the same film with a thickness of 1 μm. As the two films were processed in identical ways, the difference must be attributed to domain contributions, that either decrease with increasing frequency, or increase with increasing film thickness. For both contributions, experimental and theoretical evidence could be found. The change in the Q-factor confirms the role of domain wall motion, since the Q-factors decrease from 18 to 3 in these two samples.
- High coupling constants are associated with high acoustic losses in the PZT, which are inversely proportional to the Q-factor. It has been observed that our PZT films with high coupling constants, such as films at the morphotropic phase boundary and {100} textured films, have higher losses. Films with lower coupling (tetragonal films and (111) textured films) lead to lower losses. Since the figure of merit (FOM) of a device is the product $k_t^2 \cdot Q$ the highest FOM of 15 was observed for a film with

a high coupling composition (MPB) and low coupling texture (111). The main loss mechanism in films with a composition at the MPB and {100} textured films can be attributed to the presence of ferroelastic domains, leading to losses due to oscillation of the domain walls, as well as inhomogeneous excitation and emission of acoustic waves.

- The study of the TFBAR resonance data allows the derivation of materials parameters of PZT at high frequencies. These parameters were identified and compared to low frequency measurements, if possible. The stiffness of the films is of particular interest, since little data for thin films can be found. Stiffness constants c_{33}^{D} of PZT films at the morphotropic phase boundary (with an applied electric field of 7.5 V - 10 V) of 170 GPa for the (111) textured sol-gel film and 205 GPa for the {100} textured sol-gel film (gradient free) were found. These values are rather higher than the values for bulk ceramics (around 150 GPa). Since we applied a relatively high bias, leading to a reduction of domains and in addition we use a textured structure, these higher values can be explained by the improved domain alignment as compared to ceramics.

- The dielectric constant as derived from the admittance Y measured by the network analyser did not change between 50 MHz and 2 GHz. The observed change in the imaginary part of Y can be consistently attributed to parasitic capacitances and inductances. The values are nevertheless reduced by 30-50% compared to the 100 Hz -1 MHz dielectric constants. Although this reduction is expected, the effect is difficult to quantify because the applied measurement technique is prone to significant errors. Nevertheless the constant ε value in the range of 50 MHz to 2 GHz is clear and means that the domain wall mobility of mostly 180° domains hardly changes in this frequency range. Concerning ferroelastic domain wall motions, their contribution to the dielectric constant is either weak, or constant in the considered frequency range. The absence of such contributions is supported by the large stiffness. In ceramics, one usually observes shape effects, or size effects related to waves trapped in grains or large domains. In the thin film case, the dominant shape effect is the basic BAW resonance, at which indeed the dielectric constant drops. But no other kind of shape resonances, and consequently drop of dielectric response is observed.

- The piezoelectric coefficient d_{33}, however, did not significantly change between low frequencies, measured by double beam interferometry, and 1.4 GHz as derived from resonance and antiresonance frequencies. As frequency measurements are precise, the values derived from resonances are thus reliable. The small change with frequency indicates that we mostly observe lattice (intrinsic) contributions with only a weak domain wall contribution. The maximum d_{33} value observed at around 110 pm/V is indeed close to the expected lattice contribution.

- The resonance frequencies and the coupling constants have been observed to be field dependent, suggesting tunable filters based on PZT are feasible. The bandpass region of a filter could be shifted up to 2% with a range of k_t^2 from 8 to 23% using a PZT film with a composition of 53/47 and a (111) texture. Simultaneous tuning of shunt and series resonance of the MPB composition is promising for tunable filter applications.

- The properties of PZT films are highly dependant on their domain configuration and the domain configuration is determined by the stress in the film. For this reason the stress behaviour of tetragonal {100} textured films was studied as a function of temperature and heat treatment. As known from previous works, silicon substrates are unfavourable for high *c*-domain fractions. This was confirmed in this work, PZT 30/70 exhibited a *c*-domain fraction of only about 50-60%. It was discovered that an anneal in vacuum at 550°C lead to a significant reduction of *c*-domains in a tetragonal 30/70 PZT film. On the contrary, if the sample was subjected to a compressive stress during cooling, the *c*-domain fraction could be increased. The detailed mechanism by which the vacuum anneal influences domain formation and film stress, however, is not yet well understood. As the misfit strain S_m is increased by the vacuum anneal, one cannot ascribe the effect to an increase of the lattice constants by oxygen vacancy formation. The effect is rather compatible with the idea that the 550°C annealing temperature is close to θ_C, leading to an $a_1/a_2/a_1/a_2$ pattern during the anneal in order to relax the tensile stress in the film. The role of the oxygen vacancies and electrons formed at the same time, is not clear. They may help to stabilise the ferroelectric ordering above the expected θ_C. This mechanism would explain why the strain S_m increases for a film annealed in vacuum, but not for a film annealed in oxygen.

- In order to avoid the high losses associated with the high coupling, two alternative solutions were explored. One solution is a TFBAR based on PZT using MgO as a substrate. The MgO induces compressive stress on the PZT film leading to highly *c*-axis oriented films. The high *c*-axis orientation of the PZT deposited on MgO reduces the density of ferroelastic domains and thus the acoustic losses. High coupling constants can be expected for these films due to the high fraction of *c*-domains. The coupling constant is expected to be over 0.5 for these films, however, our devices did not allow to measure it, due to difficulties of membrane liberation. The micromachining of these devices needs some improvement, however the preliminary data look very promising.

- In another research direction we explored how to reduce acoustic losses by the use of the uniaxial ferroelectric potassium lithium niobate (KLN). The unique ferroelectric axis in this material means that only 180° domain walls are present, which can theoretically be removed by poling. This material has been deposited in thin film form using pulsed laser deposition (PLD). KLN thin films with a $\{001\}$) texture were deposited successfully on Pt/Si substrates. The films were piezoelectric with a $d_{33,f}$ value of around 10 pm/V and a dielectric constant of 250. This is the first time that piezoelectric properties were measured on KLN thin films. A columnar structure has been observed, however the small grain size and the rough surface make it difficult to apply this material to TFBAR's.

Table 5.1 gives an overview of the work performed in this thesis.

Piezo / **Substrate**	**PZT**	**KLN**
Si	TFBAR's fabricated, high k_t^2 measured, losses high	Films fabricated by PLD, measurements of $\varepsilon_{33,f}$, $d_{33,f}$, film fabrication delicate
MgO	Highly c-axis oriented films fabricated, promising results for TFBAR fabrication	

Table 5.1: Overview of the main results obtained in this thesis, showing the combinations of substrates and piezoelectric films used.

5.2 Outlook

PZT for BAW applications

The high coupling constants that can be achieved in PZT TFBARs justify further research in this field. However the losses are a significant hindrance to applications, and must be overcome. The explored solution using MgO as a substrate in order to have c-axis orientation is worth studying further. The etching difficulties may be solved, either by using back side etching, or by using a diffusion barrier. The use of a diffusion barrier is challenging, since all of the films need to be grown epitaxially. Stirring the etching solution is another possible improvement for future experiments, since the stagnant etching solution in this work, could have reduced the the etch rate in the cavities. One path which could lead to lower losses is to study doped PZT films in TFBARs. Little work has been done in this field and a lot of possibilities are waiting to be explored. The tunability of PZT is also a key feature that is worth exploiting, and further efforts are required to understand the range of tunability available in these different types of samples.

KLN for BAW applications

The controlled growth of stoichiometric and well textured KLN thin films proved to be very challenging. The deposition process was not very reproducible since the concentrations of the very mobile ions, potassium and lithium, were difficult to control. However, the theoretical properties justify further research on this material. For further continuation of this work, it may be necessary to utilise a deposition method that is more apt to overcome the difficulties of KLN processing. At present it is not yet clear whether KLN could become a viable material for TFBAR filters. More effort is needed to investigate this interesting material with its large potential.

Appendix A

List of Symbols and their Units

Symbol	Meaning	SI Unit
a,b,c	Crystal axes	meter
c_{ijkl},c_{mn}	Elastic stiffness constant	newton per square meter
C	Capacitance in resonator equivalent circuit	farad
C_0	Shunt capacitance in resonator equivalent circuit	farad
C_p	Parasitic capacitance in resonator equivalent circuit	farad
d_{ijk}, d_{im}	Piezoelectric constant	meter per volt = coulomb per newton
Dij, D_m	Dielectric displacement	coulomb per square meter
D(superscript)	At constant electric displacement	
e_{ijk}, e_{im}	Piezoelectric constant	coulomb per square meter
E_{ij}, E_m	Electric field	volt per meter
E(superscript)	At constant electric field	volt per meter
f	Frequency	hertz
f_a	Antiresonance frequency	hertz
f_r	Resonance frequency	hertz
G	Gibbs free energy	joule
k_t	Coupling constant for thickness mode vibration for thickness mode vibration	
l	Length	meter
L	Inductance in resonator equivalent circuit	henry
L_s	Parasitic series inductance	henry

	in resonator equivalent circuit	
Q	Resonator quality factor	
R	Resistance in resonator equivalent circuit	ohm
R_s	Parasitic series resistance in resonator equivalent circuit	ohm
s_{ijkl},s_{mn}	Elastic compliance constant	square meter per newton
S(superscript)	At constant strain	
S_{ij}, S_m	Strain components	
T(superscript)	At constant stress	
t	thickness	meter
T_{ij}, T_m	Stress components	newton per square meter
U	Internal energy	joule
v	Sound velocity	meter per second
w	Width	meter
x,y,z	Rectangular axes of a crystal	meter
X	Electric circuit reactance	ohm
Y	Electric circuit admittance	siemens
Y	Electric circuit impedance	ohm
ε_0	Permittivity of free space	farad per meter
ε_{ij}	Permittivity component	farad per meter
η	Acoustic viscosity	newton second per square meter
θ	Temperature	kelvin
λ	Wavelength	m
ν	Poisson ratio	
ρ	Mass density	kg per cubic meter
σ	Entropy	joule per kelvin
τ	Motional time constant	second
ϕ	Fraction of c-domains	
ω	Angular frequency ($2\pi f$)	hertz

Appendix B

List of abbreviations

AFM	Atomic Force Microscope
BAW	Bulk Acoustic Wave
BVD	Butterworth Van Dyke
CVD	Chemical Vapour Deposition
DC	Direct Current
FIB	Focused Ion Beam
FOM	Figure of Merit
GPS	Global Positioning System
HIP	Hot Isostatic Pressing
JVD	Jet Vapour Deposition
KLN	Lithium Potassium Niobate
MOCVD	Metal-Organic Chemical Vapour Deposition
MPB	Morphotropic Phase Boundary
PLD	Pulsed Laser Deposition
PT	Lead Titanate
PZT	Lead Zirconate Titanate
RF	Radio Frequency
SAM	Scanning Acoustic Microscope
SAW	Surface Acoustic Wave
SEM	Scanning Electron Microscope
SHF	Super High Frequency (3 GHz - 30 GHz)
SMR	Solidly Mounted Resonator
TFBAR	Thin Film Bulk Acoustic Resonator
TTB	Tetragonal Tungsten Bronze
UHF	Ultra High Frequency (300 MHz - 3 GHz)

WLAN	Wireless Local Area Network
XRD	X-Ray Diffraction

Appendix C

Simulation of stress-temperature curves

The stress versus temperature was measured for 30/70 sol-gel PZT films as described in section 2.3. The data were fitted using equation 2.5 with the spontaneous strain described by equation 2.7 below θ_P and by equation 2.7 above θ_P. The measurements of the three different samples with the simulated data are shown in Figures C.1, C.2, C.3 for the sol-gel films and in Figures C.4, C.5, C.6 for the sputtered films. The parameters du fit the data are shown in Table 2.26 for the sol-gel film and in Table 2.3 for the sputtered film.

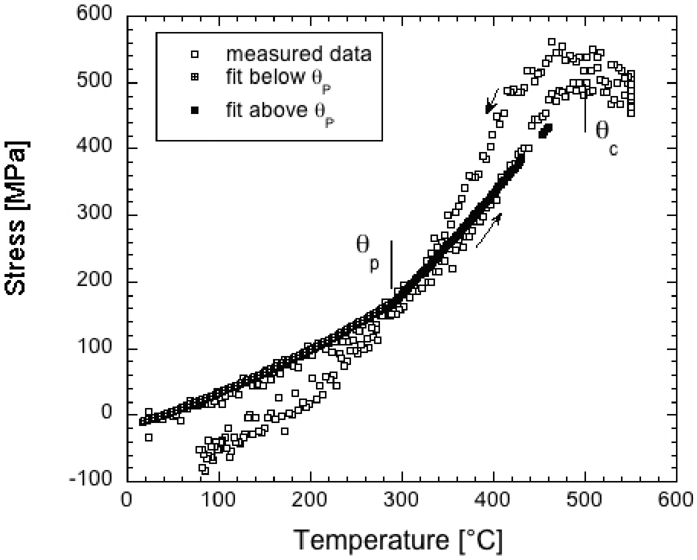

Figure C.1: Stress vs. temperature curve for the as deposited sol-gel film.

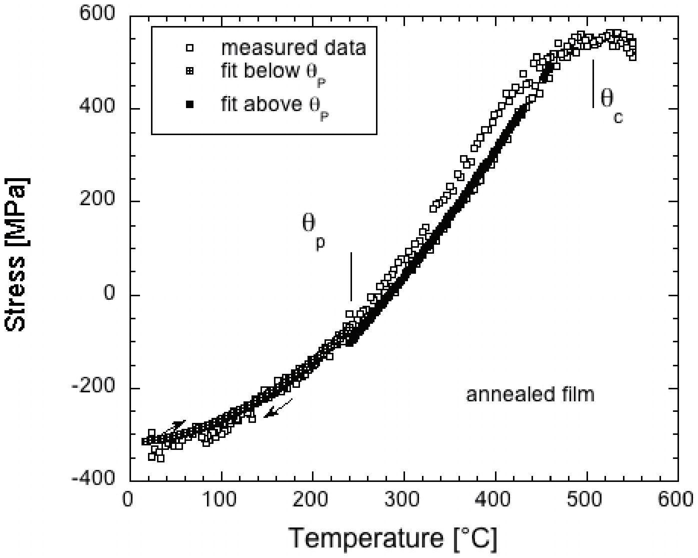

Figure C.2: Stress vs. temperature curve for the annealed sol-gel film.

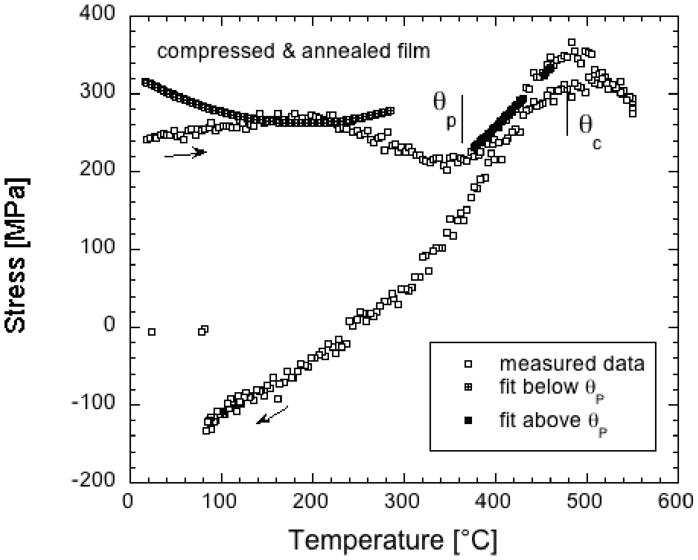

Figure C.3: Stress vs. temperature curve for the compressed and annealed sol-gel film.

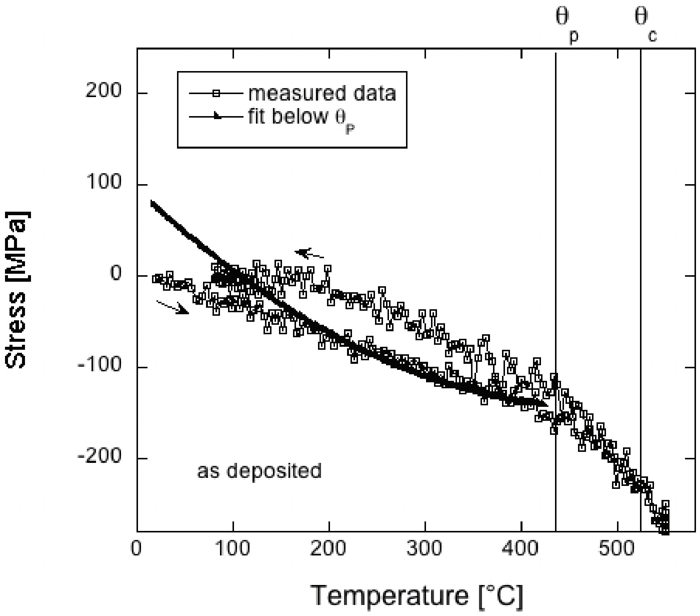

Figure C.4: Stress vs. temperature curve for the as deposited sputtered film.

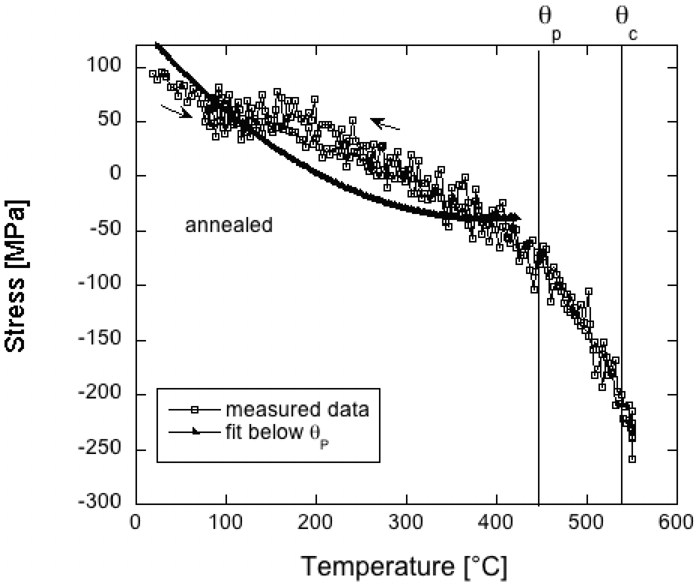

Figure C.5: Stress vs. temperature curve for the as deposited annealed sputtered film.

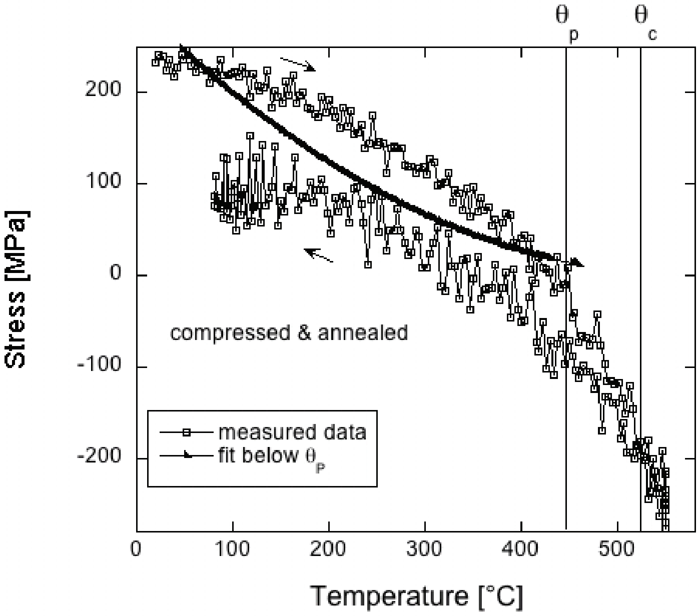

Figure C.6: Stress vs. temperature curve for the as deposited compressed and annealed sputtered film.

List of Tables

List of Figures

Bibliography

[1] R. Weigel, D. P. Morgan, J.M. Owens, A. Ballato, K. M. Lakin, K. Hashimoto, and Ruppel W. Microwave acoustic materials, devices, and applications. *IEEE Transactions On Microwave Theory and Techniques*, 50(3):738–749, 2002.

[2] M. E. Lines and A. M. Glass. *Principles and applications of ferroelectrics and related materials*. Clarendon Press, Oxford, reprinted edition, 2004. by M.E. Lines and A.M. Glass Ill. First publ. 1977.

[3] Yuhuan Xu. *Ferroelectric materials and their applications*. North-Holland, Amsterdam, 1991.

[4] T. W. Grudkowski, J. F. Black, T. M. Reeder, D. E. Cullen, and R. A. Wagner. Fundamental mode vhf-uhf bulk acoustic-wave resonators and filters on silicon. *Ieee Transactions on Sonics and Ultrasonics*, 28(5):374–374, 1981.

[5] K. M. Lakin, G. R. Kline, R. S. Ketcham, and S. G. Burns. Thin-film resonator based low insertion loss filters. *Ieee Transactions on Ultrasonics Ferroelectrics and Frequency Control*, 34(3):415–415, 1987.

[6] R. Aigner. MEMS in RF-filter applications: Thin film bulk-acoustic-wave technology. *Transducers '05, Digest of Technical Papers, Vols 1 and 2*, pages 5–8, 2005.

[7] R. Aigner. SAW and BAW technologies for RF filter applications: A review of the relative strengths and weaknesses. pages 582–589, Nov. 2008.

[8] A. Ballato, J. G. Gualtieri, and J. A. Kosinski. Ferroelectric materials for thin-film and membrane resonators. *Isaf '94 - Proceedings of the Ninth IEEE International Symposium on Applications of Ferroelectrics*, pages 674–679, 1994.

[9] P. Muralt, J. Antifakos, M. Cantoni, R. Lanz, and E. Martin. Is there a better material or thin BAW applications than AlN? *2005 IEEE Ultrasonics Symposium, Vols 1-4*, pages 315–320, 2005.

[10] S. Trolier-McKinstry and P. Muralt. Thin film piezoelectrics for MEMS. *Journal of Electroceramics*, 12(1-2):7–17, 2004.

[11] F. Martin, P. Muralt, M. A. Dubois, and A. Pezous. Thickness dependence of the properties of highly *c*-axis textured AlN thin films. *Journal of Vacuum Science and Technology A*, 22(2):361–365, 2004.

[12] Maurice H. Francombe. *Handbook of thin film devices.* Academic Press, San Diego, 2000.

[13] Hans Jaffe. Piezoelectric ceramics. *Journal of the American Ceramic Society*, 41(11):494–498, 1958.

[14] B. Noheda. Structure and high-piezoelectricity in lead oxide solid solutions. *Current Opinion in Solid State and Materials Science*, 6(1):27–34, 2002.

[15] K. Sreenivas, M. Sayer, C.K. Jen, and K. Yamanaka. Bulk and surface acoustic wave transduction in sputtered lead zirconate titanate thin films. *Ultrasonics Symposium, 1988. Proceedings., IEEE 1988*, pages 291–295 vol.1, Oct 1988.

[16] M. Yamaguchi, K. Y. Hashimoto, R. Nanjo, N. Hanazawa, S. Ttsutsumi, and T. Yonezawa. Ultrasonic properties of PZT thin films in UHF-SHF ranges - Prepared by sol gel method. *Proceedings of the 1997 IEEE International Frequency Control Symposium*, pages 544–555, 1997.

[17] N. Hanajima, S. Tsutsumi, T. Yonezawa, K. Hashimoto, R. Nanjo, and M. Yamaguchi. Ultrasonic properties of lead zirconate titanate thin films in UHF-SHF range. *Japanese Journal of Applied Physics Part 1-Regular Papers Short Notes and Review Papers*, 36(9B):6069–6072, 1997.

[18] S. Arscott, R.E. Miles, and S.J. Milne. Lead zirconate titanate thin films for microwave device applications. *IEEE Proc. - Circuits Devices Syst.*, 145(5):373–378, 1998.

[19] H.P. Loebl, M. Klee, R. Milsom, R. Dekker, C. Metzmacher, W. Brand, and P. Lok. Materials for bulk acoustic wave (BAW) resonators and filters. *J. Euro. Ceram. Soc.*, 21:2633–2640, 2001.

[20] Q.X. Su, P. Kirby, E. Komuro, M. Imura, Q. Zhang, and R. Whatmore. Thin-film bulk acoustic resonators and filters using ZnO and lead-zirconium-titanate thin films. *IEEE Trans. Microwave Theory and Tech.*, 49(4):769 – 777, 2001.

[21] P. Cong, T. L. Ren, J. S. Liu, and L. T. Liu. RF-Mems BAW filter using surface micromachining. *Integrated Ferroelectrics*, 50:71–79, 2002.

[22] K. Misu, T. Nagatsuka, S. Wadaka, C. Maeda, and A. Yamada. Film bulk acoustic wave filters using lead titanate on silicon substrate. *1998 IEEE Ultrasonics Symposium - Proceedings, Vols 1 and 2*, pages 1091–1094, 1998.

[23] C. Maeda, A. Yamada, F. Uchikawa, K. Misu, S. Wadaka, and J. Shinada. Microwave properties of La-doped lead titanate piezoelectric films for bulk acoustic wave resonators. *1998 IEEE Ultrasonics Symposium - Proceedings, Vols 1 and 2*, pages 629–632 1892, 1998.

[24] A. Yamada, C. Maeda, F. Uchikawa, K. Misu, and T. Honma. Piezoelectric properties of La-doped $PbTiO_3$ films for RF resonators. *Japanese Journal of Applied Physics Part 1-Regular Papers Short Notes and Review Papers*, 38(9B):5520–5523, 1999.

[25] Y. Park, E. K. Kim, T. Y. Lee, and J. T. Song. The modeling and fabricating of film bulk acoustic resonators using sputtered PZT films with various thickness. *Integrated Ferroelectrics*, 66:187–194, 2004.

[26] C. Zinck, E. Defay, A. Volatier, G. Caruyer, D. P. Tanon, and L. Figuiere. Design, integration and characterization of PZT tunable FBAR. *2004 14th IEEE International Symposium on Applications of Ferroelectrics-ISAF-04*, pages 29–32 335, 2004.

[27] M. Schreiter, R. Gabl, D. Pitzer, R. Primig, and W. Wersing. Electro-acoustic hysteresis behaviour of PZT thin film bulk acoustic resonators. *Journal of the European Ceramic Society*, 24(6):1589–1592, 2004.

[28] J.D. Larson, S.R. Gilbert, and B. Xu. PZT material properties at UHF and microwave frequencies derived from FBAR measurements. In *IEEE Ultrasonics Symposium*, 2004.

[29] K. Uchino and S. Hirose. Loss mechanisms in piezoelectrics: How to measure different losses separately. *IEEE Transactions on Ultrasonics Ferroelectrics and Frequency Control*, 48(1):307–321, 2001.

[30] Charles Kittel. *Introduction to solid state physics.* Wiley, New York, seventh edition, 1996.

[31] K. H. Haerdtl. Electrical and mechanical losses in ferroelectric ceramics. *Ceramics International*, 8(4):121 – 127, 1982.

[32] T. Tsurumi, H. Kakemoto, and S. Wada. Dielectric, elastic and piezoelectric losses of PZT ceramics in the resonance state. *Isaf 2002: Proceedings of the 13th IEEE International Symposium on Applications of Ferroelectrics*, pages 375–378, 2002.

[33] C. B. Sawyer and C. H. Tower. Rochelle salt as a dielectric. *Physical Review*, 35(3):0269–0273, 1930.

[34] D. Damjanovic. Ferroelectric, dielectric and piezoelectric properties of ferroelectric thin films and ceramics. *Reports on Progress in Physics*, 61(9):1267–1324, 1998.

[35] G. Arlt and H. Dederichs. Complex elastic, dielectric and piezoelectric constants by domain-wall damping in ferroelectric ceramics. *Ferroelectrics*, 29(1-2):47–50, 1980.

[36] G. Arlt, H. Dederichs, and R. Herbiet. 90-Degree-domain wall relaxation in tetragonally distorted ferroelectric ceramics. *Ferroelectrics*, 74(1-2):37–53, 1987.

[37] P. Gerthsen, K. H. Hardtl, and N. A. Schmidt. Correlation of mechanical and electrical losses in ferroelectric ceramics. *Journal of Applied Physics*, 51(2):1131–1134, 1980.

[38] S. J. Zhang, N. P. Sherlock, R. J. Meyer, and T. R. Shrout. Crystallographic dependence of loss in domain engineered relaxor-PT single crystals. *Applied Physics Letters*, 94(16):–, 2009.

[39] A. L. Kholkin, C. Wutchrich, D. V. Taylor, and N. Setter. Interferometric measurements of electric field-induced displacements in piezoelectric thin films. *Review of Scientific Instruments*, 67(5):1935–1941, 1996.

[40] C. J. Brinker and G. W. Scherer. Sol-gel science: The physics and chemistry of sol-gel processing, 1990.

[41] S. R. Gurkovich and J. B. Blum. Preparation of monolithic lead-titanate by sol-gel process, 1984.

[42] K. D. Budd, S. K. Dey, and D. A. Payne. Sol-gel processing of PT, PZ, PZT and PLZT thin films. *Brit. Ceram. Soc. Proc.*, 36:107–121, 1985.

[43] F. Calame and P. Muralt. Growth and properties of gradient free sol-gel lead zirconate titanate thin films. *Applied Physics Letters*, 90(6):1–12, 2007.

[44] K. Abe, H. Tomita, H. Toyoda, M. Imai, and Y. Yokote. PZT thin-film preparation on Pt-Ti electrode by RF-sputtering. *Japanese Journal of Applied Physics Part 1-Regular Papers Short Notes and Review Papers*, 30(9B):2152–2154, 1991.

[45] K. Suu, A. Osawa, Y. Nishioka, and N. Tani. Stability control of composition of RF-sputtered Pb(Zr, Ti)O_3 ferroelectric thin film. *Japanese Journal of Applied Physics Part 1-Regular Papers Short Notes and Review Papers*, 36(9B):5789–5792, 1997.

[46] A. Okada. Some electrical and optical properties of ferroelectric lead-zirconate-lead-titanate thin films. *Japanese journal of applied physics*, 48(7):2905–2909, 1977.

[47] K. Sreenivas and M. Sayer. Characterization of Pb(Zr,Ti)O_3 thin-films deposited from multi-element metal targets. *Journal of Applied Physics*, 64(3):1484–1493, 1988.

[48] K. Sreenivas, M. Sayer, and P. Garrett. Properties of DC magnetron-sputtered lead zirconate titanate thin-films. *Thin Solid Films*, 172(2):251–267, 1989.

[49] T. Maeder, L. Sagalowicz, and P. Muralt. Stabilized platinum electrodes for ferroelectric film deposition using Ti, Ta and Zr adhesion layers. *Japanese Journal of Applied Physics Part 1-Regular Papers Short Notes and Review Papers*, 37(4A):2007–2012, 1998.

[50] P. Muralt, T. Maeder, L. Sagalowicz, S. Hiboux, S. Scalese, D. Naumovic, R. G. Agostino, N. Xanthopoulos, H. J. Mathieu, L. Patthey, and E. L. Bullock. Texture control of $PbTiO_3$ and Pb(Zr,Ti)O_3 thin films with TiO_2 seeding. *Journal of Applied Physics*, 83(7):3835–3841, 1998.

[51] G. B. Harris. Quantitative measurement of preferred orientation in rolled uranium bars. *Philosophical Magazine*, 43(336):113–123, 1952.

[52] Powder diffraction file. *card 33-0784*. JCPDS-ICDD (Joint Commitee on Powder Diffraction Standards - International Center for Diffraction Data), Swarthmore, 1996.

[53] N. Ledermann. {100}- Textured, piezoelectric Pb(Zr_x, Ti_{1-x})O_3 thin films for MEMS: Integration, deposition and properties. *Sensors and actuators. A, Physical*, 105(2):162–170, 2003.

[54] S. Hiboux and P. Muralt. Piezoelectric and dielectric properties of sputter deposited (111), (100) and random-textured Pb(Zr_x Ti_{1-x})O_3 (PZT) thin films. *Ferroelectrics*, 224(1-4):743–750, 1999.

[55] Florian Calame. *PZT thin film growth and chemical composition control on flat and novel three-dimensional micromachined structures for MEMS devices.* EPFL, Lausanne, 2007. par Florian Calame ill.

[56] A. L. Roytburd, S. P. Alpay, L. A. Bendersky, V. Nagarajan, and R. Ramesh. Three-domain architecture of stress-free epitaxial ferroelectric films. *Journal of Applied Physics*, 89(1):553–556, 2001.

[57] N. A. Pertsev, V. G. Kukhar, H. Kohlstedt, and R. Waser. Phase diagrams and physical properties of single-domain epitaxial $Pb(Zr_{1-x}Ti_x)O_3$ thin films. *Physical Review B*, 67(5):–, 2003.

[58] V. G. Kukhar, N. A. Pertsev, H. Kohlstedt, and R. Waser. Polarization states of polydomain epitaxial $Pb(Zr_{1-x}Ti_x)O_3$ thin films and their dielectric properties. *Physical Review B*, 73(21):–, 2006.

[59] G. H. Yi, Z. Wu, and M. Sayer. Preparation of $Pb(Zr,Ti)O_3$ thin-films by sol-gel processing - electrical, optical, and electro-optic properties. *Journal of Applied Physics*, 64(5):2717–2724, 1988.

[60] S. S. Sengupta, S. M. Park, D. A. Payne, and L. H. Allen. Origins and evolution of stress development in sol-gel derived thin layers and multideposited coatings of lead titanate. *Journal of Applied Physics*, 83(4):2291–2296, 1998.

[61] S. Corkovic, R. W. Whatmore, and Q. Zhang. Development of residual stress in sol-gel derived $Pb(Zr,Ti)O_3$ films: An experimental study. *Journal of Applied Physics*, 103(8), 2008.

[62] B. A. Tuttle, J. A. Voigt, T. J. Garino, D. C. Goodnow, R. W. Schwartz, D. L. Lamppa, T. J. Headley, and M. O. Eatough. Chemically prepared $Pb(Zr,Ti)O_3$ thin-films - the effects of orientation and stress. *Isaf 92 : Proceedings of the Eighth IEEE International Symposium on Applications of Ferroelectrics*, pages 344–348 644, 1992.

[63] J. F. Shepard, S. TrolierMcKinstry, M. Hendrickson, and R. Zeto. The effects of biaxial stress on the ferroelectric characteristics of PZT thin films. *Materials for Smart Systems*, 459:47–51, 1997.

[64] L. Lian and N. R. Sottos. Stress effects in sol-gel derived ferroelectric thin films. *Journal of Applied Physics*, 95(2):629–634, 2004.

[65] T. Garino and M. Harrington. Residual stress in PZT thin films and its effect on ferroelectric properties. *Materials Research Society Symposium Proceedings*, 243:341–347, 1992.

[66] T. Kumazawa, Y. Kumagai, H. Miura, M. Kitano, and K. Kushida. Effect of external stress on polarization in ferroelectric thin films. *Applied Physics Letters*, 72(5):608–610, 1998.

[67] W. K. Lim, J. R. Ahn, Y. S. Kim, J. C. Lee, S. O. Park, and S. I. Lee. The effect of stress on the electrical properties of PZT thin films. *Ferroelectrics*, 259(1-4):251–257, 2001.

[68] S. Alpay, R. Ramesh, and A. L. Roytburd. Effect of uniaxial stress fields on the domain selection of epitaxial ferroelectric films. *Ferroelectrics*, 221(1-4):245–250, 1999.

[69] A. Y. Emelyanov, N. A. Pertsev, and A. L. Kholkin. Effect of external stress on ferroelectricity in epitaxial thin films. *Physical Review B*, 66(21):–, 2002.

[70] J. W. Lee, C. S. Park, M. Kim, and H. E. Kim. Effects of residual stress on the electrical properties of PZT films. *Journal of the American Ceramic Society*, 90(4):1077–1080, 2007.

[71] G. G. Stoney. The tension of metallic films deposited by electrolysis. *Proceedings of the Royal Society of London Series A-Containing Papers of a Mathematical and Physical Character*, 82(553):172–175, 1909.

[72] Powder diffraction file. *card 01-070-4261.* JCPDS-ICDD (Joint Commitee on Powder Diffraction Standards - International Center for Diffraction Data), Swarthmore, 1996.

[73] W. R. Cook, F. J. Scholz, and D. Berlincourt. Thermal expansion and pyroelectricity in lead titanate zirconate and barium titanate. *Journal of Applied Physics*, 34(5):1392–1398, 1963.

[74] G. A. C. M. Spierings, G. J. M. Dormans, W. G. J. Moors, M. J. E. Ulenaers, and P. K. Larsen. Stresses in Pt/Pb(Zr,Ti)O_3/Pt thin-film stacks for integrated ferroelectric capacitors. *Journal of Applied Physics*, 78(3):1926–1933, 1995.

[75] M. J. Haun, E. Furman, H. A. Mckinstry, and L. E. Cross. Thermodynamic theory of the lead zirconate-titanate solid-solution system, .2. tricritical behavior. *Ferroelectrics*, 99:27–44, 1989.

[76] Y. Okada and Y. Tokumaru. Precise determination of lattice-parameter and thermal-expansion coefficient of silicon between 300-k and 1500-k. *Journal of Applied Physics*, 56(2):314–320, 1984.

[77] R. Bruchhaus, H. Huber, D. Pitzer, and W. Wersing. Deposition of ferroelectric PZT thin-films by planar multitarget sputtering. *Ferroelectrics*, 127(1-4):137–142, 1992.

[78] Powder diffraction file. *card 01-070-4260*. JCPDS-ICDD (Joint Commitee on Powder Diffraction Standards - International Center for Diffraction Data), Swarthmore, 1996.

[79] Markus Kohli. *Investigation of pyroelectric thin films and their application in micromachined infrared detectors*. PhD thesis, 1998.

[80] X. H. Du, U. Belegundu, and K. Uchino. Crystal orientation dependence of piezoelectric properties in lead zirconate titanate: Theoretical expectation for thin films. *Japanese Journal of Applied Physics Part 1-Regular Papers Short Notes and Review Papers*, 36(9A):5580–5587, 1997.

[81] X. H. Du, J. H. Zheng, U. Belegundu, and K. Uchino. Crystal orientation dependence of piezoelectric properties of lead zirconate titanate near the morphotropic phase boundary. *Applied Physics Letters*, 72(19):2421–2423, 1998.

[82] F. Xu, S. Trolier-McKinstry, W. Ren, B. M. Xu, Z. L. Xie, and K. J. Hemker. Domain wall motion and its contribution to the dielectric and piezoelectric properties of lead zirconate titanate films. *Journal of Applied Physics*, 89(2):1336–1348, 2001.

[83] H. Tanaka, H. Tabata, T. Kawai, Y. Yamazaki, S. Oki, and S. Gohda. Controlling factors on the synthesis of $Pb(Zr_xTi_{1-x})O_3$ films. *Thin Solid Films*, 289(1-2):29–33, 1996.

[84] Stephane Hiboux. *Study of growth and properties of in-situ sputter deposited $Pb(Zr_x, Ti_{1-x})O_3$ thin films*. PhD thesis, EPFL, 2002.

[85] D. V. Taylor and D. Damjanovic. Piezoelectric properties of rhombohedral Pb(Zr, Ti)O_3 thin films with (100), (111), and "random" crystallographic orientation. *Applied Physics Letters*, 76(12):1615–1617, 2000.

[86] C. R. Cho, L. F. Francis, and M. S. Jang. Piezoelectric properties and acoustic wave detection of $Pb(Zr_{0.52}Ti_{0.48})O_3$ thin films for microelectromechanical systems sensor. *Japanese Journal of Applied Physics Part 2-Letters*, 38(7A):L751–L754, 1999.

[87] L. Lian and N. R. Sottos. Effects of thickness on the piezoelectric and dielectric properties of lead zirconate titanate thin films. *Journal of Applied Physics*, 87(8):3941–3949, 2000.

[88] R. Lanz and P. Muralt. Bandpass filters for 8 GHz using solidly mounted bulk acoustic wave resonators. *IEEE Transactions on Ultrasonics Ferroelectrics and Frequency Control*, 52(6):936–946, 2005.

[89] S. Sherrit, H. D. Wiederick, B. K. Mukherjee, and M. Sayer. An accurate equivalent circuit for the unloaded piezoelectric vibrator in the thickness mode. *Journal of Physics D-Applied Physics*, 30(16):2354–2363, 1997.

[90] K. M. Lakin, G. R. Kline, and K. T. Mccarron. High-Q microwave acoustic resonators and filters. *IEEE Transactions on Microwave Theory and Techniques*, 41(12):2139–2146, 1993.

[91] K. K. Shung. Very high frequency (VHF) ultrasonic imaging. *Proceedings of the IEEE 25th Annual Northeast Bioengineering Conference*, pages 107–108, 1999.

[92] J. Conde and P. Muralt. Characterization of sol-gel $Pb(Zr_{0.53}Ti_{0.47})O_3$ in thin film bulk acoustic resonators. *IEEE Transactions on Ultrasonics Ferroelectrics and Frequency Control*, 55(6):1373–1379, 2008.

[93] S. Sherrit, H. D. Wiederick, B. K. Mukhejee, and M. Sayer. Field dependence of the complex piezoelectric, dielectric, and elastic constants of Motorola PZT 3203 HD ceramic. *Smart Materials Technologies*, 3040:99–109, 1997.

[94] M. Lukacs, T. Olding, M. Sayer, R. Tasker, and S. Sherrit. Thickness mode material constants of a supported piezoelectric film. *Journal of Applied Physics*, 85(5):2835–2843, 1999.

[95] V. Ryzhenko, L. Burianova, and P. Hana. Influence of electric field on the ultrasound velocity in PZT ceramics. *Journal of Electroceramics*, 20(1):35–41, 2008.

[96] F. S. Foster, L. K. Ryan, and D. H. Turnbull. Characterization of lead zirconate titanate ceramics for use in miniature high-frequency (20-80 MHz) transducers. *IEEE Transactions on Ultrasonics Ferroelectrics and Frequency Control*, 38(5):446–453, 1991.

[97] M. Adachi and A. Kawabata. Elastic and piezoelectric properties of potassium lithium-niobate (KLN) crystals. *Japanese Journal of Applied Physics*, 17(11):1969–1973, 1978.

[98] Y. Uematsu and S. Koide. Piezoelectric properties of ferroelectric $K_3Li_2(Ta_xNb_{1-x})_5O_{15}$ Single Crystals. *Japanese Journal of Applied Physics*, 9(3):336–, 1970.

[99] S. C. Abrahams, P. B. Jamieson, and J.L. Bernstein. Ferroelectric tungsten bronze-type crystal structures: Potassium Lithium Niobate $K_{6-X-Y}Li_{4+X}Nb_{10+Y}O_{30}$. *Journal of Chemical Physics*, 54(6):2355–2363, 1971.

[100] B. A. Scott, E. A. Giess, B. L. Olson, G. Burns, A. W. Smith, and D. F. Okane. Tungsten bronze field in system K_2O-Li_2O-Nb_2O_5. *Materials Research Bulletin*, 5(1):47–56, 1970.

[101] T. Ikeda and K. Kiyohashi. Study of subsolidus equilibria in K_2O-Li_2O-Nb_2O_5 system. *Japanese Journal of Applied Physics*, 9(12):1541–1552, 1970.

[102] S. L. Xu, J. H. Lee, J. J. Kim, H. Y. Lee, and S. H. Cho. Effect of Nb_2O_5 content on dielectric characteristics of tungsten-bronze-structured KLN ceramics. *Materials Science and Engineering B-Solid State Materials for Advanced Technology*, 99(1-3):483–486, 2003.

[103] M. Adachi, M. Hori, T. Shiosaki, and A. Kawabata. Epitaxial-growth of $K_3Li_2Nb_5O_{15}$ (KLN) single-crystal films on $K_2BiNb_5O_{15}$ (KBN) by RF sputtering. *Ferroelectrics*, 29(1-2):125–131, 1980.

[104] T. Shiosaki, M. Adachi, and A. Kawabata. Sputtering and chemical vapor-deposition of piezoelectric ZnO, AlN and $K_3Li_2Nb_5O_{15}$ films for optical-waveguides and surface acoustic-wave devices. *Thin Solid Films*, 96(2):129–140, 1982.

[105] M. Adachi, A. Kawabata, and F. Takeda. Preparation of tungsten-bronze thin-films. *Japanese Journal of Applied Physics Part 1-Regular Papers Short Notes and Review Papers*, 30(9B):2208–2211, 1991.

[106] K. Chikuma, A. Onoe, and A. Yoshida. Waveguiding epitaxial potassium lithium niobate single-crystal films deposited by metalorganic chemical vapor deposition. *Japanese Journal of Applied Physics Part 1-Regular Papers Short Notes and Review Papers*, 37(10):5582–5587, 1998.

[107] S. K. Park, M. S. Baek, S. C. Bae, S. Y. Kwon, J. H. Kim, and K. W. Kim. Growth of four-fold grained $K_3Li_2Nb_5O_{15}$ thin film using RF-magnetron sputtering. *Japanese Journal of Applied Physics Part 1-Regular Papers Short Notes and Review Papers*, 38(11):6483–6486, 1999.

[108] S. K. Park. Crystallographic properties of four-fold grain $K_3Li_2Nb_5O_{15}$ thin films. *Thin Solid Films*, 457(2):397–401, 2004.

[109] S. K. Park, S. C. Bae, B. J. Choi, G. H. Nam, Y. J. Kim, and K. W. Kim. Fabrication and annealing effect of c-axis orientated potassium lithium niobate thin film on glass substrate. *Japanese Journal of Applied Physics Part 1-Regular Papers Short Notes and Review Papers*, 39(3A):1303–1308, 2000.

[110] H. X. Zhang, C. H. Kam, Y. Zhou, X. Q. Han, S. D. Cheng, Y. C. Chan, K. Pita, and Y. L. Lam. Optical properties of potassium lithium niobate films. *Integrated Ferroelectrics*, 33(1-4):71–78, 2001.

[111] S. Ono, N. Yamada, and S. Hirano. Potassium lithium niobate films derived from aqueous precursor solution. *Journal of the American Ceramic Society*, 84(7):1415–1420, 2001.

[112] H. X. Zhang, Y. Zhou, C. H. Kam, S. Cheng, X. Q. Han, Y. L. Lam, and Y. C. Chan. Preparation and characterization of sol-gel derived potassium lithium niobate films. *Journal of Crystal Growth*, 211(1-4):82–85, 2000.

[113] Z. X. Cheng, X. L. Wang, K. Ozawa, and H. Kimura. A novel aqueous solution method for $K_3Li_2Nb_5O_{15}$ film and powder. *Journal of Crystal Growth*, 307(2):353–357, 2007.

[114] R. S. Weis and T. K. Gaylord. Lithium-niobate - Summary of physical-properties and crystal-structure. *Applied Physics a-Materials Science and Processing*, 37(4):191–203, 1985.

[115] Z. S. Zhan, Y. S. Gong, Q. Shen, and L. M. Zhang. Growth and properties of pulsed laser deposited $K_3Li_2Nb_5O_{15}$ thin films. *Composite Materials V*, 351:184–188, 2007.

[116] V. Jayasree, R. Ratheesh, V. Ganesan, V. R. Reddy, C. Sudarsanakumar, V. P. M. Pillai, and V. U. Nayar. Influence of reactive oxygen ambience on the structural, morphological and optical properties of pulsed laser ablated potassium lithium niobate thin films. *Thin Solid Films*, 517(2):603–608, 2008.

[117] Y. D. Juang. Phase transition of lithium potassium niobate ceramics. *Solid State Communications*, 120(1):25–28, 2001.

[118] Powder diffraction file. *card 34-0122*. JCPDS-ICDD (Joint Commitee on Powder Diffraction Standards - International Center for Diffraction Data), Swarthmore, 1996.

[119] Powder diffraction file. *card 20-0631.* JCPDS-ICDD (Joint Commitee on Powder Diffraction Standards - International Center for Diffraction Data), Swarthmore, 1996.

[120] S. V. Kalinin, A. Rar, and S. Jesse. A decade of piezoresponse force microscopy: Progress, challenges, and opportunities. *IEEE Transactions on Ultrasonics Ferroelectrics and Frequency Control*, 53(12):2226–2252, 2006.

[121] K. Iijima, Y. Tomita, R. Takayama, and I. Ueda. Preparation of c-Axis oriented $PbTiO_3$ thin-films and their crystallographic, dielectric, and pyroelectric properties. *Journal of Applied Physics*, 60(1):361–367, 1986.

[122] R. Takayama and Y. Tomita. Preparation of epitaxial $Pb(Zr_xTi_{1-x})O_3$ thin-films and their crystallographic, pyroelectric, and ferroelectric properties. *Journal of Applied Physics*, 65(4):1666–1670, 1989.

[123] Y. Sakashita, T. Ono, H. Segawa, K. Tominaga, and M. Okada. Preparation and electrical-properties of MOCVD-deposited PZT thin-films. *Journal of Applied Physics*, 69(12):8352–8357, 1991.

[124] I. Kanno, S. Fujii, T. Kamada, and R. Takayama. Piezoelectric properties of c-axis oriented $Pb(Zr,Ti)O_3$ thin films. *Applied Physics Letters*, 70(11):1378–1380, 1997.

[125] S. Fujii, I. Kanno, T. Kamada, and R. Takayama. Preparation of c-axis oriented $Pb(Zr, Ti)O_3$ thin films by RF-magnetron sputtering and their dielectric and piezoelectric properties. *Japanese Journal of Applied Physics Part 1-Regular Papers Short Notes and Review Papers*, 36(9B):6065–6068, 1997.

[126] I. Kanno, Y. Yokoyama, H. Kotera, and K. Wasa. Thermodynamic study of c-axis-oriented epitaxial $Pb(Zr,Ti)O_3$ thin films. *Physical Review B*, 69(6):–, 2004.

[127] N. Yamauchi, T. Shirai, T. Yoshihara, Y. Hayasaki, T. Ueda, T. Matsushima, K. Wasa, I. Kanno, and H. Kotera. High coupling piezoelectric thin films of $Pb(Zr,Ti)O_3$-based ternary perovskite compounds for GHz-range film bulk acoustic resonators. *Applied Physics Letters*, 94(17):172903, 2009.

[128] H. Okino, T. Nishikawa, M. Shimizu, T. Horiuchi, and K. Matsushige. Electrical properties of highly strained epitaxial $Pb(Zr,Ti)O_3$ thin films on MgO(100). *Japanese Journal of Applied Physics Part 1-Regular Papers Short Notes and Review Papers*, 38(9B):5388–5391, 1999.

[129] J. Hong, H. W. Song, H. C. Lee, W. J. Lee, and K. No. Structure and electrical properties of Pb(Zr_xTi_{1-x})O_3 deposited on textured Pt thin films. *Journal of Applied Physics*, 90(4):1962–1967, 2001.

[130] M. H. Kwak, S. E. Moon, S. J. Lee, Y. T. Kim, H. C. Ryu, and W. J. Kim. Microwave dielectric properties of ferroelectric Pb($Zr_{1-x}Ti_x$)O_3 thin films using interdigital capacitors. *Integrated Ferroelectrics*, 54:659–664, 2003.

[131] G. L. Brennecka, W. Huebner, B. A. Tuttle, and P. G. Clem. Use of stress to produce highly oriented tetragonal lead zirconate titanate (PZT 40/60) thin films and resulting electrical properties. *Journal of the American Ceramic Society*, 87(8):1459–1465, 2004.

[132] Masafumi Kobune, Yusuke Nishioka, Tomoaki Inoue, and Tetsuo Yazawa. Growth and ferroelectric properties of Pb($Zr_{0.52}Ti_{0.48}$)O_3 thin films crystallized on MgO single-crystal substrates by hot isostatic pressing. *Journal of Crystal Growth*, 275(1-2):e2421 – e2425, 2005. Proceedings of the 14th International Conference on Crystal Growth and the 12th International Conference on Vapor Growth and Epitaxy.

[133] R. Desfeux, C. Legrand, A. Da Costa, D. Chateigner, R. Bouregba, and G. Poullain. Correlation between local hysteresis and crystallite orientation in PZT thin films deposited on Si and MgO substrates. *Surface Science*, 600(1):219–228, 2006.

[134] K. Terada, T. Suzuki, I. Kanno, and H. Kotera. Fabrication of single crystal PZT thin films on glass substrates. *Vacuum*, 81(5):571–578, 2007.

[135] T. Kotani, T. Nakanishi, and K. Nomura. Fabrication of a new pyroelectric infrared-sensor using MgO surface micromachining. *Japanese Journal of Applied Physics Part 1-Regular Papers Short Notes and Review Papers*, 32(12B):6297–6300, 1993.

[136] K. Sangwal. *Etching of crystals theory, experiment, and application.* North-Holland, Amsterdam, 1987.

Publications and Symposia

2009 **Dielectric and acoustical high frequency characterisation of PZT thin films**
J. Conde and P. Muralt
IOP Conf. Ser.: Mat. Sci. and Eng., **2009**, EMRS spring meeting, Strasbourg.

Piezoelectric materials parameters for piezoelectric thin films in GHz applications
P. Muralt, **J. Conde**, A. Artieda, F. Martin and M. Cantoni
International Journal of Microwave and Wireless Technologies, **2009**,Vol 1, p. 19-27.

2008 **Characterization of sol-gel $Pb(Zr_{0.53}Ti_{0.47})O_3$ in thin film bulk acoustic resonators**
J. Conde and P. Muralt
IEEE Transactions on Ultrasonics Ferroelectrics and Frequency Control, **2008**, vol. 55, pp. 1373-1379.

Characterisation of PZT in Thin Film Bulk Acoustic Wave Resonators
J. Conde and P. Muralt
Mater.Res.Symp.Proc., **2008**, Vol 1075, paper 1075-J03-03.

2005 **Is there a better material or thin BAW applications than AlN?**
P. Muralt, **J. Antifakos**, M. Cantoni, R. Lanz, and F. Martin
IEEE Ultrasonics Symposium, **2005**, Vol 1-4, pp. 315-320.

Janine Conde

Date of Birth:	May 26, 1979
Maiden Name:	Antifakos
Nationality:	Swiss, Citizen of Rüti (GL)
Present Address:	Chemin des Perrettes 15 CH-1024 Ecublens Switzerland
Phone:	+41 76 510 44 48
Email:	janine.conde@epfl.ch

Education

2005 – 2009	Doctoral student at the Ceramics Laboratory , Department of Materials, Swiss Federal Institute of Technology (EPF Lausanne)
2001/02	Exchange year at EPF Lausanne, Switzerland
1999 – 2005	Studies of Material Sciences and Engineering at ETH Zurich. Graduation with the degree 'Dipl. Werkstoff-Ing. ETH' (BSc and MSc Material Engineering)
1998 – 1999	Studies of Biology, Option II (Biochemistry), Switzerland
1992 – 1998	Matura Typus B at the 'Kantonsschule Glarus', Switzerland

Experience

2005	ETH Zurich, Scientific collaborator, Institute of Surface Science and Technology (LSST)
2004/05	Diploma thesis on doped AlN films, University of Cambridge, UK
2003	Semesterproject at PLATIT AG, Grenchen, Switzerland
2002	Internship at Universidad Polytechnica de Valencia, Spain
2002	Internship at ABB, Oerlikon, Switzerland